Project no.:	**101095738**		
Project full title:	**6G SHort range extreme communication IN Entities**		
Project Acronym:	**6G-SHINE**		
Project start date:	**01/03/2023**	**Duration**	**30 months**

D3.2 – RIS TECHNOLOGIES AND MODELS FOR IN-X SUBNETWORKS

Due date	29/02/2024	**Delivery date**	28/02/2024
Work package	WP3		
Responsible Author(s)	Davide Dardari (CNIT)		
Contributor(s)	Andrea Abrardo (CNIT), Davide Dardari (CNIT), Vittorio Degli Esposti (CNIT), Marina Lotti (CNIT), Muhammad Awais Jadoon (IDE), Ognen Ognenoski (IDE), Silvia Palmucci (CNIT), Fredrik Rusek (SONY), Giulia Torcolacci (CNIT), Enrico Maria Vitucci (CNIT)		
Version	V1.0		
Reviewer(s)	Meng Li (IMEC), Bernhard Raaf (APPLE)		
Dissemination level	Public		

Co-funded by the European Union

Horizon Europe Grant Agreement No. 101095738. Views and opinions expressed are however those of the author(s) only and do not necessarily reflect those of the European Union or SNS JU. Neither the European Union nor the granting authority can be held responsible for them.

VERSION AND AMENDMENT HISTORY

Version	Date (DD/MM/YYYY)	Created/Amended by	Changes
0.1	4/10/2023	D. Dardari (CNIT)	TOC proposal
0.2	6/11/2023	D. Dardari (CNIT)	TOC approval
0.3	11/12/2023	G. Torcolacci (CNIT), M. Lotti (CNIT), S. Palmucci (CNIT), A. Abrardo (CNIT)	Contribution to Secs. 2 and 5
0.4	12/12/2023	Fredrik Russek (SONY)	Contribution to Sec. 3
0.5	20/12/2023	D. Dardari (CNIT), E. Vitucci, V. Degli Esposti (CNIT)	Contribution to Sec. 2
0.6	15/1/2024	CNIT, IDE, SONY	Contribution refinements
0.7	23/1/2024	F. Rusek (SONY), Ognen Ognenoski (IDE), D. Dardari (CNIT)	Sections review by section leaders
0.8	31/1/2024	D. Dardari (CNIT)	Final version ready for internal review
0.9	15/2/2024	F. Rusek (SONY), Ognen Ognenoski (IDE), D. Dardari (CNIT), S. Palmucci (CNIT)	Revised version
1.0	28/2/2024	D. Dardari (CNIT)	Submitted version

Table of Contents

FIGURES

TABLES

ABBREVIATIONS

Acronym	Description
3GPP	3rd Generation Partnership Project
5G	5th Generation
6G	6th Generation
AAL	antenna array-like
AD	autonomous driving
AI	artificial intelligence
AO	alternate optimization
AP	access point
AR	augmented reality
BackCom	backscatter communication
BCD	block coordinate descent
BS	base station
CC	control channel
CCU	connectivity control unit
CDF	cumulative distribution function
CR	constraint relaxation
CSI	channel state information
CSMA	carrier-sense multiple access
DC	dual connectivity
DL	downlink
DMA	dynamic metasurface antenna
DMRS	demodulation reference signal
ECU	electronic control unit
E/E	electrical/electronic
EM	electromagnetic
Embb	enhanced mobile broadband
ETSI	European telecommunications standards institute
FDMA	frequency division multiple access
HC	element with high capabilities

HPCU	high-performance computing unit
i.i.d.	independently and identically distributed
IoT	Internet-of-things
IO	indoor office
IRT	isochronous real-time
ISG	industry specification group
IT	Information technology
KKT	Karush-Kuhn-Tucker
KPI	key performance indicator
KVI	key value indicator
LC	element with low capabilities
LOS	line-of-sight
MAC	medium access control
MIMO	multiple-input multiple-output
MISO	Multiple-input single-output
ML	machine learning
mMTC	massive machine-type communication
mmWave	millimetre wave
MSE	mean square error
MU-MIMOO	multi-user multiple-input multiple-output
NLOS	non-line-of-sight
NOMA	non orthogonal multiple access
NR	new radio
NRC	network control repeater
N-RIS	non-reconfigurable intelligent surface
OFDM	orthogonal frequency division multiplexing
PHY	physical layer
PLC	programmable logic controller
QoS	quality of service
RAN	radio access network
RF	radiofrequency

RIS	reconfigurable intelligent surface
RL	reinforcement learning
R-RIS	reflecting RIS
RRM	radio resource management
RV	random variable
RX	receiver
SCM	self-conjugating metasurface
SDG	sustainability development goal
SDR	semidefinite relaxation
SI	study item
SINR	signal-to-interference-plus-noise ratio
SIR	signal-to-interference ratio
SM	shopping mall
SNE	subnetwork element
SNEC	SNE category
SRE	smart radio environment
TC	technical component
TDMA	time division multiple access
TE	transversal electric
TM	transversal magnetic
TRL	technology readiness level
TRP	transmission/reception points
T-RIS	transmitting RIS
TX	Transmitter
UAV	unmanned aerial vehicle
UTD	uniform theory of diffraction
UE	user equipment
UL	Uplink
URLLC	ultra reliable low latency communication
UTD	uniform theory of diffraction
VR	virtual reality

WA	weight adaptation
WMMSE	weighted minimum mean square error
XR	extended reality

EXECUTIVE SUMMARY

This deliverable reports the activities carried out in Task 3.3 “Reconfigurable intelligent surfaces” during the first year of the project. Reconfigurable Intelligent Surfaces (RISs) are expected to play a crucial role in next-generation wireless networks as they enable the smart radio environment (SRE) design paradigm, integrating the propagation environment into system optimization for improved performance of wireless applications. While RISs might represent a low-cost and energy-efficient solution to extend the coverage, especially in harsh propagation environments, and to add more degrees of freedom in interference shaping and medium access control (MAC) strategies, they introduce new challenges that could make them not always convenient if not properly tackled. For instance, identifying the proper model and simulation tools properly accounting for the main electromagnetic effects, finding low-complexity, low-overhead RIS optimization strategies, defining suitable and low-overhead control channel protocols, and investigating the additional interference that RIS might generate in the presence of close subnetworks, especially if they are not coordinated, are the main issues to be addressed.

In this context, it is fundamental to understand to what extent RISs might be beneficial for in-X subnetworks under study in 6G-SHINE and how they can be exploited. With this purpose in mind, in this deliverable first a survey and classification of RIS technologies is provided, both available and under-study. The main models to characterize and design RISs are detailed along with possible integration into Ray-tracing tools under development in WP2. A preliminary analysis of promising RIS technologies that are expected to improve the Key Performance Indicators (KPIs) as well as the main design issues for the use cases identified in WP2 are presented. This analysis represents a baseline for the subsequent research activity aimed at identifying RIS-aided PHY/MAC methods and RIS optimization algorithms. In this direction, some preliminary investigations and optimization methods are presented. Specifically, starting from the analysis of the state-of-the-art, a RIS-aware MAC framework for 6G-SHINE in-X subnetworks in which users are grouped based on their traffic characteristics, position, mobility, and their Quality-of-Service (QoS) requirements is proposed. Some results on RIS deployment and optimization strategies are reported, highlighting the underexplored interference issues in RIS-aided systems and comparing various RIS hardware architectures as well as proposing a new one offering spatial-selective properties. In addition, the optimal RIS configuration in multiple users multiple-input multiple-output (MU-MIMO) scenarios are investigated through the proposal of a low-complexity rate and weight adaptation strategy. An initial mapping of the methods to the KPIs, Key Value Indicators (KVIs), and use cases of the project, whose definition is presented in deliverable D2.2 [1], is provided. The concepts and results presented in this deliverable are based on works that are currently in progress, and further findings and recommendations will be provided in deliverable D3.4 at M28.

1 INTRODUCTION

Reconfigurable intelligent surfaces (RISs) are considered one of the key technological breakthroughs of next-generation wireless networks. According to the emerging smart radio environment (SRE) design paradigm, in which the propagation environment is incorporated into the system design and optimization loop, the introduction of RISs allows dynamic control over the radio propagation environment. This, in turn, enhances the performance of wireless-based applications with a reduced or more hardware-efficient infrastructure.

Therefore, it is of interest to understand to what extent RISs might bring advantages in In-X subnetworks to approach the targeted KPIs/KVIs and help in achieving the following project objectives:

- Objective 3. "*Design new physical layer (PHY) enablers for scalable requirements in terms of latency, reliability, or throughput, tailored to devices with constrained computational capabilities by leveraging the opportunities offered by short range subnetworks*. "
- Objective 4. "*Develop new effective medium access control (MAC) solutions for efficient multiplexing of diverse traffic types in a subnetwork, including deterministic traffic.* "

Along this direction, this deliverable describes the identified RIS technologies and the related models for future In-X subnetworks. It also reports a preliminary set of RIS optimization strategies studied in Task 3.3. The concepts and results presented in this deliverable are based on works that are currently in progress, and further findings and recommendations will be provided in Deliverable D3.4. The activities carried out in Task 3.3 are all related to the technical component (TC) #7 (RIS enhancements) defined in 6G-SHINE. For what the elements composing the subnetwork are regarded, this deliverable will adopt the nomenclature defined in deliverable D2.2 [1].

In section 2, a classification of available or under-study RISs and non-reconfigurable intelligent surfaces (N-RISs) is presented based on different features and technologies (Subtask 3.3a: "*Identification of RIS technologies for the considered in-X subnetwork scenarios*"). One fundamental aspect of an RIS is its analytical and simulative modelling. To address this aspect, the main analytical models for RISs, consisting of arrays of tuneable elements or metamaterials (impedance sheet), are reported. Additionally, there is a discussion on how such models can be integrated into ray-tracing tools to obtain more accurate simulations. Building upon the aforementioned classification, the section concludes with a preliminary analysis of the most promising RIS technologies (if any) for each scenario/use case identified in WP2. This includes providing initial insights into the potential advantages in terms of KPIs. For the most promising solutions, design and optimization methods will be developed and assessed in the next project period.

In section 3, preliminary investigations on the RIS-generated interference between subnetworks and/or microcells are presented (Subtask 3.3c: "*RIS deployment and interference mitigation strategies*"). In fact, in many scenarios (e.g., industrial) a subnetwork is meant to co-exist with a microcell. When the subnetwork is equipped with a RIS, the RIS may reflect signals from the microcell causing unwanted and uncontrolled interference. Interference issues are underexplored for RIS-aided systems in general, and for RIS-aided subnetworks in particular. Within this context, in this section we consider several potential RIS hardware architectures and compare them with respect to interference. An analysis of the coexistence of RIS-equipped subnetworks with a micro-cell is presented by considering that a RIS is reflecting all impinging signals which implies that a RIS may potentially cause interference to the macro-cell also in separate frequency bands as its reflection characteristics is typically not strongly bandlimited. To mitigate or avoid interference, a novel spatial-selective RIS architecture is proposed and compared with a conventional non-selective RIS.

Section 4 addresses the design of RIS-aware MAC Protocols (Subtask 3.3b: "*RIS aware PHY and MAC protocols*"). It should be noted that conventional MAC protocols may underperform when enabling medium access to multiple users since these do not harness the benefits of RIS which may lead to improved user performance. Therefore, a RIS-aware MAC framework for 6G-SHINE X-subnetworks, in which users are grouped based on their traffic characteristics, position, mobility, and their QoS requirements, is introduced. The section concludes with some initial considerations for the control channel and its involvement within the design of RIS-aware MAC protocols.

Finally, in section 5, preliminary results on RIS optimization strategies are reported (Subtask 3.3c: "*RIS deployment and interference mitigation strategies*"). In particular, the problem of reducing both the communication overhead and computational complexity is tackled by reducing the dimension of the RIS optimization problem. This is achieved by employing a more streamlined set of potential RIS configurations, transforming the RIS optimization problem into an assignment problem. A second study addresses the optimal RIS configuration in MU- MIMO scenarios by proposing a rate weight adaptation strategy which aims at achieving a form of proportional fairness among subnetwork elements (SNEs).

We present below an initial -but not exclusive- mapping of the methods to the KPIs/KVIs and use cases of the project, whose preliminary definition is presented in deliverable D2.2. In particular, Table 1 describes the main KPIs targeted by the presented methods.

Regarding the KVIs, it is worth mentioning that being 6G-SHINE a low Technology Readiness Level (TRL) project, we do not aim at directly measuring the impact of the designed solutions in terms of KVIs, as such assessment will only be possible once the designed solutions are implemented and integrated into a coherent system design (beyond the scope of the project). Still, KVIs are at the centre of our technology design, and we speculate how our solutions can be the basic "bricks" for addressing environmental, economic, and social sustainability for future in-X subnetwork products. In particular, below we report the envisioned KVIs associated with the introduction of RIS technologies in In-X subnetworks:

- *Environmental sustainability*: improved energy efficiency and reduced use of electronic material thanks to the semi-passive nature of RISs.
- *Social sustainability*: improved scalability enabled by RISs can ease the support of a larger number of sensors an extended coverage without adding active devices such as Access Points (APs). Infrastructure support for industry and innovation, with improved efficiency and productivity, together with improved workers safety thanks to a more reliable system.
- *Economic sustainability*: Reduced installation and maintenance costs with respect to active APs.

Table 2 presents the mapping of the presented methods to the use case categories (and specific use cases) as defined in deliverable D2.2 that can mostly benefit from them. This does not exclude that other use cases can take advantage from them. We remark that we do not aim at evaluating each presented method for all the mapped use cases. In our performance evaluation, we rather highlight the main use case or use case category of interest, as we believe the extension to a different use case with similar KPIs is straightforward.

Finally, Table 3 highlights potential involvement of the proposed methods in the 3rd Generation Partnership Project (3GPP) standardization process. It has to be remarked that while an extended and more complex form of RIS, namely Network Control Repeater (NCR), has already been standardized as a part of 3GPP's upcoming Rel-18 [105], RISs intended as semi-passive electromagnetic devices have not yet been studied in 3GPP. While some companies proposed including RIS as a study item (SI) in 3GPP for Rel-18, most considered it premature and suggested exploring it for 6G technology instead. Consequently, the proposal was not approved for Rel-18. To address standardization, the European Telecommunications Standards Institute (ETSI) Industry Specification Group (ISG) for RIS was established in September 2021. It serves as the pre-standardizing group for RIS, aiming to define use cases, deployment scenarios, and requirements towards global standardization [107,108].

Expectations expressed in these tables reflect the vision and understanding at the current time of the project, and they might be revised in the second year of the project based on research results as well as on the monitoring of the current standardization activities carried out in WP6.

TABLE 1 KPIS TARGETED BY THE PRESENTED METHODS

Technology/method	Main target KPIs
Optimal RIS configuration in multiple users MIMO scenarios	Communication support for high number of SNEs. Minimum experience data rate assured for the SNEs. Extended coverage.
Non-diagonal and low-rank RIS technologies	Data rate, latency, maximum number of users, interference reduction.
RIS-aware MAC protocol for subnetworks	Number of users, data rate, latency.

TABLE 2 MAPPING BETWEEN PRESENTED METHODS AND USE CASES AS DEFINED IN D2.2

Technology/method	Main use case category(ies)	Relevant use cases
Optimal RIS configuration in multiple users MIMO scenarios	Industrial	Robot control, Unit test cell
Non-diagonal and low-rank RIS technologies	Industrial, vehicular	Robot control, in-vehicle wireless subnetwork zone
RIS-aware MAC protocol for subnetworks	Industrial and Consumer	Subnetwork swarms, immersive education, augmented reality navigation

TABLE 3 STANDARDIZATION POTENTIAL OF THE PRESENTED METHODS.

Technology/method	Standardization potential
Optimal RIS configuration in multiple users MIMO scenarios	This method has potential relevance for 6G standardization, 3GPP Radio Access Network (RAN) 1 Release 19 and beyond to support communication systems with many SNEs that communicates with just one access point (AP) and guarantee broadband services to all the SNEs [105]. A reduced number of APs entails a reduced amount of necessary power supply, thus allowing for more sustainable systems.
Non-diagonal and low-rank RIS technologies	One form of a non-diagonal and low-rank RIS has already been standardized as a part of 3GPP's upcoming Rel-18, namely Network Control Repeaters (NCRs) [105]. This work will likely be continued in many future releases. Problems of NCRs identified in this deliverable, and its solutions (to be further developed in upcoming deliverables) have, therefore, high potential for standardization.
RIS-aware MAC protocol for subnetworks	This method has more exploratory nature and in the preliminary design, there are no considerations to aim at standardisation. However, as we further develop and evaluate the method, the intention is to identify and develop facets of the protocol suitable for standardisation into ETSI RIS ISG or 3GPP RAN 2.

2 RIS TECHNOLOGIES AND MODELS

2.1 RIS TECHNOLOGIES

Smart radio environment (SRE) is an emerging design paradigm for next-generation wireless networks according to which the propagation environment enters in the loop of the system design and optimization. This is possible through the introduction of reconfigurable intelligent surfaces (RISs) that allow to dynamically control the radio propagation environment to improve the performance of wireless-based applications with reduced or efficient hardware infrastructure [2,3]. As it will be detailed later, a RIS can be realized using conventional antenna array technologies or metasurfaces made of metamaterial. While the transition from theoretical concepts and new ideas to precise definitions and applications is ongoing, a key attribute defining RISs is their dynamic response reconfigurability, achieved with low-cost hardware, thereby holding the potential for high energy efficiency [4,5]. However, to determine the actual benefits of the RIS technology in terms of cost, performance, and energy efficiency, rigorous quantification is essential, and these benefits are application-dependent, competing with alternative technologies such as active multi-antenna relays and smart repeaters [5]. Nevertheless, theoretical [6], algorithmic [7], and experimental [8] works within the established community demonstrate clear advancements and value propositions in many contexts even though in many others their potential advantage is not completely clear [9].

Within these diverse fields of application, RISs play a crucial role in the realm of electromagnetic wave control and manipulation. The spectrum of capabilities they offer is extensive, encompassing reflections, refractions, absorptions, and focusing, which collectively contribute to reshaping and directing electromagnetic waves in the radio propagation environment. Furthermore, RISs exhibit the capacity for manipulating the polarization of electromagnetic waves, thereby enhancing the adaptability of these surfaces to varying communication scenarios. The capability for beam splitting, focusing, and steering further extends the potential applications of RIS technology in wireless communication systems. Beyond these fundamental manipulations, RISs facilitate analogue processing, offering a unique approach to signal modification and enhancement. Additionally, they support collimation, a process that aligns electromagnetic waves into parallel beams, contributing to efficiency in communication and precision in sensing applications. Moreover, the ability to modify the amplitude and phase of electromagnetic waves enhances the fine-tuning capabilities of RISs, allowing for advanced control over signal properties. This versatility in electromagnetic wave control positions RISs as promising candidates for addressing the complex challenges and demands of modern wireless communication systems. RISs find applications in communication [10], sensing [11] (e.g., human activity recognition [12] and digital twins [13]), as well as localization/tracking [14] and detection of passive objects [15]. Ongoing research is exploring new directions, leveraging RISs for mapping/imaging to reconstruct a high-fidelity and resolution map of the surrounding radio environment and detect the presence of unknown objects within it [16].

In the framework of the 6G-SHINE project, the introduced RIS taxonomy functions as a systematic framework for comprehending and categorizing diverse functionalities of RISs. It facilitates the identification of potential modalities for their application in the scenarios outlined in the 6G-SHINE project. Drawing upon existing literature [17,18,19], this taxonomy utilizes varied criteria for the classification of RISs, considering their operational features, functionalities, and implementations. The resulting classification, delineated in Table 4, provides a comprehensive overview of the nuanced roles that RISs can undertake in wireless communication, sensing, and related applications. This methodical approach enhances the systematic exploration and comprehension of potential applications and benefits associated with RIS technology in the context of the 6G-SHINE project.

TABLE 4 RIS CLASSIFICATION

Feature	Type
Reconfigurability	• Reconfigurable surface (RIS) • Static surface (N-RIS, smart skin)
Local vs global boundary conditions	• Diagonal • Non-diagonal
Power	• Passive • Active
Selectivity	• Space-time selective • Space-frequency selective (metaprism)
Data bearing	• No data bearing • Data bearing (e.g., coding metasurfaces)
Reflecting / Transmitting	• R-RIS / T-RIS
Implementation technology	• Metasurfaces-based • Antenna arrays-based

The RISs' classification can be structured into multiple categories, each delineated by distinct characteristics that significantly influence their operational capabilities.

The first feature pertains to ***reconfigurability***, distinguishing between reconfigurable surfaces and static surfaces (non-reconfigurable) [19]. Reconfigurable surfaces have the capability to dynamically adapt and alter their properties. Depending on the reconfiguration rate (today up to 1 million conf/s), the platform can be sufficiently flexible for real-time adjustments in response to changing communication conditions. This implies that they need a dedicated control channel with associated protocol and signalling overhead as well as a power supply for the control logic even though they might be passive from the electromagnetic (EM) point of view. In contrast, static surfaces are configured during the fabrication process and hence lack the ability to undergo dynamic transformations. However, they require neither a power supply (fully passive) nor a dedicated control channel. They are often referred to as smart skin [20]. In the following we will call them non-reconfigurable intelligent surfaces (N-RIS) even though we will use the term RIS to denote generic intelligent surface.

The second category focuses on the type of ***EM boundaries*** imposed by the RIS. When boundaries are local, the reflected EM field at a certain surface location/element depends only on the incident EM field at the same location/element. Instead, global boundaries refer to the case where the reflected EM field at a certain surface location/element might depend also on the incident field in a different location/element provided that the overall RIS is passive. This means that locally, the reflection coefficient might be larger than one (amplification) even though the RIS is passive because of the coupling between the different elements. In terms of modelling, this classification distinguishes between diagonal and non-diagonal matrices, reflecting the configuration of the phase shifts imparted by the intelligent surface. Diagonal matrices imply independent adjustments to each element and local boundary conditions, whereas non-diagonal matrices denote interdependence among the phase shifts and global boundary conditions and allow for spatial selectivity, as investigated in section 3.2 [21].

The third feature focuses on the power aspect, discerning between EM ***passive and active RISs***. Passive RISs rely on the reflection and manipulation of incident signals without additional energy input, whereas active RISs incorporate powered elements that actively contribute to reinforce the reflected EM wave. Often, active RISs are referred to as smart repeaters or Network Control Repeaters (NCRs).

Another characteristic of the RIS technology is ***selectivity***. It is a versatile feature that allows for tailored control over electromagnetic waves. Space-time selectivity enables dynamic adjustments in both spatial and temporal

domains, as seen in [22], while space-frequency selectivity, as seen in metaprisms, adds an additional layer of control by selectively manipulating different frequency components based on their spatial characteristics. These capabilities make RISs powerful tools for applications in communication, sensing, and other areas of electromagnetic wave manipulation. Regarding frequency-selective antennas, literature [23,24,25] provide insights where the reflective properties of the metasurface-based surfaces are dependent on the frequency of the incident signal. Spatial selectivity typically refers to the capability of reflecting a signal coming only from a specific direction and as highlighted previously, require non-diagonal structures imposing global boundaries.

In the context of RIS, ***data bearing*** means that the surface is designed or configured to carry information in backscatter mode or used as a smart transmitting or receiving antenna. In backscatter mode, the information can be encoded in the way the surface interacts with incident electromagnetic waves, altering their phase, amplitude, or polarization based on specific coding schemes. Backscatter Communication (BackCom) is based on passive reflection and modulation of an incident wave, has emerged as a cutting-edge technological paradigm for self-sustainable Internet-of-things (IoT). Nevertheless, contemporary BackCom systems are limited to short-range and low data rate applications only, rendering them insufficient on their own to support pervasive connectivity among the massive number of IoT devices. In this regard, RISs have come to the forefront to improve the propagation conditions by passive signal reflections, in fact the reflected signal can be combined with direct link signals, either constructively, to boost the received signal strength, or destructively, to attenuate the co-channel interference, hence improving overall system performance [26, 27]. In [28] a self-conjugating metasurface (SCM) is a type of phased array antenna system designed to automatically align itself with the direction of an incoming signal. The key principle behind retrodirective antenna arrays is to retransmit a received signal back to the source, and this retransmitted signal carries information that enables the source to adjust and align the transmission path. They have applications in various fields, including radar systems, satellite communication, and wireless networks. They offer a self-aligning capability, making them valuable in situations where maintaining a stable and reliable communication link is essential. In the context of intelligent surfaces used as antennas, it is worth mentioning the dynamic metasurface antenna (DMA) which introduces the concept of real-time reconfigurability, allowing adaptive adjustments to the radio environment as communication conditions evolve. DMAs, as transceiver architectures, employ meta-elements as the RF front end, showcasing hybrid beamforming capabilities with both analogue and digital signal processing [29]. Other examples are the coding metasurfaces, that are a specific type of metasurface designed to encode information in the electromagnetic response. By carefully engineering the properties of individual meta-elements, coding metasurfaces can be programmed to perform specific tasks or communicate information to receiving devices [30]. Coding metasurfaces use a pattern or code in the arrangement of their meta-elements to control the interaction with incident electromagnetic waves. This code is designed to achieve specific functionalities, such as beam steering, focusing, or polarization conversion. They find applications in areas such as imaging, communication, and sensing. A RIS with integrated sensing capability has been proposed in [31].

The RISs can be used mainly in two different ways: as ***reflecting or transmitting RIS***. The Reflecting-RIS (R-RIS) [32,33,34] is primarily designed to manipulate incoming electromagnetic waves by reflecting them in a controllable manner. The surface elements of the RIS can adjust the phase, amplitude, or polarization of incident waves to achieve specific outcomes, such as beam steering, signal enhancement, or interference suppression through reflective mechanisms. On the other hand, a Transmitting-RIS (T-RIS) [35] is designed to allow electromagnetic waves to pass through the surface with controllable characteristics. The surface elements of the RIS can be adjusted to modify the transmitted waves' properties, such as their phase, amplitude, or polarization, to achieve specific objectives, like beam shaping or optimizing the link quality.

Regarding the ***RIS' implementation technologies***, a rough classification can be done between RISs whose cells can be seen as small radiating elements with tuneable load impedance [36,37,38, 39, 40-43], i.e., using volumetric metamaterials with several wavelength thick or simply conventional antenna arrays with dynamic loads (array-type RISs), and subwavelength metasurfaces producing a modification of the EM field which can be modelled as impedance sheets [44, 45, 46, 47, 48].

The RIS configured as arrays of tuneable radiating antenna elements allow for dynamic adjustments to selectively control the direction, polarization, and phase of impinging electromagnetic waves, thereby enabling optimal beamforming, polarization control, and phase modulation for customized communication channels. Simplifying, each element of the antenna-array-based RIS is an antenna whose load can be configured to change dynamically the way the element backscatters the impinging EM wave. Typically, pin-diodes are used to change the load.

The concept of metamaterials and metasurfaces was born in electromagnetics in 2000, and then, extended to other fields of physics (acoustics, mechanics, thermodynamics, etc.) [9]. With reference to the last decades, we can identify three main generations of metasurfaces. The first generation of metasurfaces is characterized by structures whose electromagnetic response does not change in space and time. Typical applications in antenna systems are cloaking devices, lenses, polarization transformers, wide-angle impedance matching sheets, spatial filters, high-impedance surfaces and artificial magnetic conductors, etc. The second generation includes inhomogeneous structures (quasiperiodic, gradient structures) exhibiting a surface impedance that varies point by point. Metasurface-based RISs are made of metamaterial and are composed of many closely spaced sub-wavelength unit cells (e.g., 1/10 of the wavelength), often called meta-atoms. This dense presence of meta-atoms makes the metasurface acting as an impedance sheet, altering surface impedance characteristics to influence the interaction with the impinging EM field. This alteration determines the EM boundary conditions imposed by the surface that facilitate enhanced impedance matching, beam steering, and improved communication outcomes through the tailored manipulation of reflected and transmitted electromagnetic waves [49]. Metamaterials are artificially engineered materials whose properties go beyond what Nature offers. Typical applications in antenna systems are: metasurface antennas, beam pointing towards anomalous directions, etc. The third generation is characterized by homogeneous and inhomogeneous structures whose properties are controlled in time [9]. The ability to control the properties in both space and time allows implementing tunable, time-modulated, reconfigurable, and programmable metasurfaces. Metasurfaces may provide full control of the reflected and transmitted electromagnetic fields. In Figure 1, the main functionalities that can be realized using metasurfaces are illustrated, in particular they are (a) bandpass frequency selective surface; (b) bandstop frequency selective surface; (c) high-impedance surface; (d) narrowband perfect absorber; (e) twist polarizer; (f) right-handed circular-polarization frequency selective surface; (g) linear-to-circular polarization converter; (h) two-dimensional leaky-wave antenna with a conical-beam pattern; (i) focusing transmit array; (j) focusing reflect array; (k) at Luneburg lens; (l) hologram. The degrees of freedom available in the third generation of metasurfaces make them a unique tool for designing a new generation of antenna systems and a key-enabling technology for future (beyond 5G) communication systems.

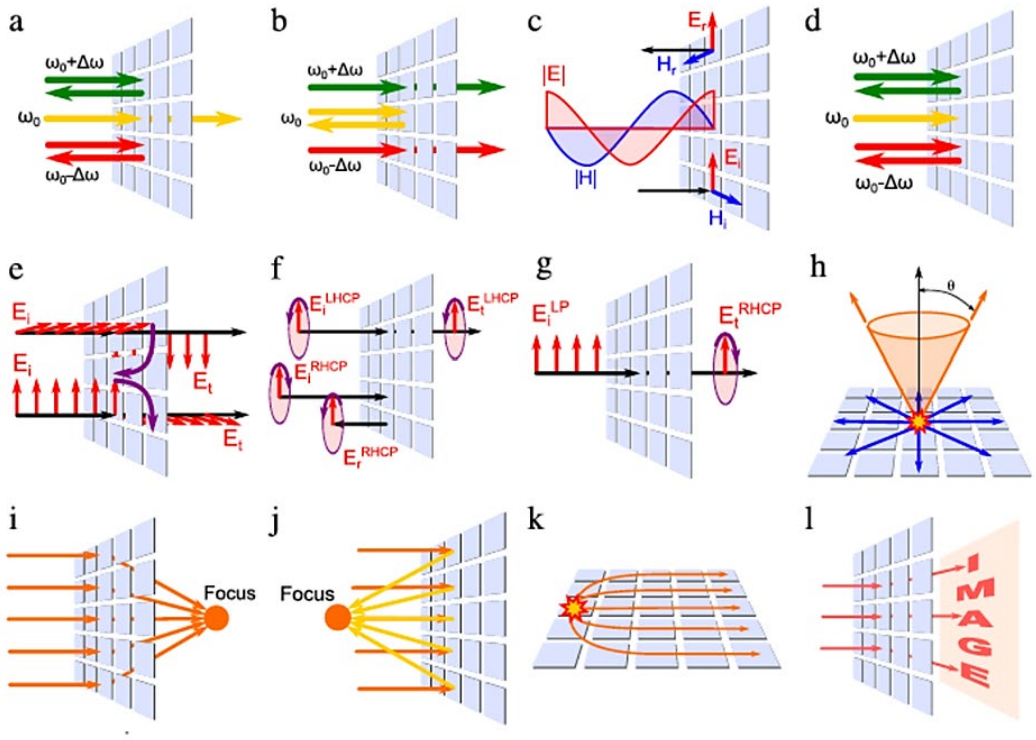

FIGURE 1 SELECTED FUNCTIONALITIES OF METASURFACES [44].

Surveys on the main technologies adopted to realize metasurfaces can be found in [44, 19], whereas surveys on the main applications of metasurface in the field of wireless communications can be found in [50, 51,52,53,54,55]. It is obvious that the metasurface-based RIS is a sophisticated concept which requires a complex fabrication process. Recently, metagrating based-RIS has been introduced [56] using a periodic array of scatterers. Compared to the metasurface, only the scatterers of the metagrating are sub-wavelength, while the distance between them is comparable to wavelength. This allows it to be significantly simpler to fabricate and can afford broader bandwidths because of the larger footprint of the constituent elements.

Finally, it is worth mentioning the novel concept of hybrid reflecting RISs has been recently proposed as a promising unification of conventional RISs and relays, to facilitate the creation of an enhanced intelligent and reconfigurable environment [57]. Another very promising opportunity offered by metasurfaces is the possibility to perform some processing operations directly at the EM level with consequent significant reduction in terms of complexity, cost, energy consumption, latency, and size compared to the digital counterpart. In this perspective, an example is given by the Stacked Intelligent Metasurfaces (or Stacked RIS) [58,59]. A stacked RIS refers to a configuration where multiple RIS layers are vertically stacked on top of each other. Each RIS layer is a planar structure comprising numerous passive elements, such as reflective or refractive units, that can manipulate the phase and amplitude of incoming electromagnetic waves. The vertical arrangement of multiple RIS layers allows for increased degrees of freedom in shaping and redirecting the incident waves. This stacking enables more intricate control over the signal propagation environment, offering the potential for improved signal quality, coverage, and link performance. The individual RIS layers can be dynamically adjusted to adapt to changing communication conditions or user requirements, providing a versatile and adaptive solution for wireless communication.

In summary, the classification of RIS technologies unveils a diverse array of methodologies and possible employments, each offering unique advantages in optimizing wireless communication. These categories highlight the versatile applications and potential contributions of RIS technologies in advancing the concept of a smart radio environment.

2.2 RIS MODELS

As illustrated in the previous section, there are several types of RISs as well as several technologies to realize them, each of them obeying a specific model. In the following, we will focus on the models associated with the most widely used types of RIS, respectively, the RIS made of an array of tuneable elements and RIS made of a metasurface acting as an impedance sheet.

2.2.1 ARRAYS OF TUNABLE RADIATING ANTENNA ELEMENTS

This implementation typically makes use of standard antenna array technology therefore qualifying it as a metasurface is improper. Nevertheless, it has earned significant attention within the realm of RIS due to its relative ease of achieving reconfigurable surfaces and most of today prototypes and products rely on it. Considering a RIS composed of a planar array consisting of *N x M* cells (i.e., antenna elements), a comprehensive equivalent model of the (n, m)-th cell of the metasurface positioned at $\mathbf{p}_{\mathrm{nm}}$ as illustrated in Figure 2.

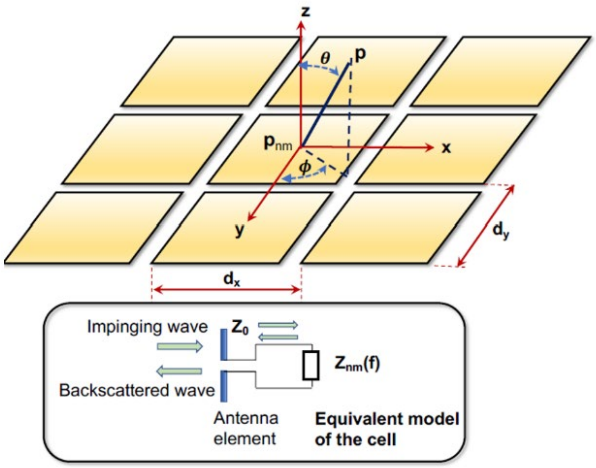

FIGURE 2 METASURFACE COMPOSED OF ELEMENTARY CELL. [23]

This model comprises a radiation element (antenna) positioned above a ground screen loaded with a cell-specific impedance Z_{nm}, where $n = 1,2, \dots, N$ and $m = 1,2, \dots, M$. Like conventional antenna arrays, the cells are typically separated by $\frac{\lambda}{2}$, with λ denoting the wavelength. The load impedance is designed to be unmatched with the antenna impedance Z_0 , leading to the generation of a reflected wave that is emitted back by the radiation element, i.e., backscattering. The corresponding reflection coefficient in the presence of an incident plane wave with a 3D angle $\Theta_{inc} = (\theta_{inc}, \phi_{inc})$ and observed at an angle $\Theta = (\theta, \phi)$ is given by [36,37]

$$r_{nm}(\Theta_{inc}, \Theta) = \sqrt{F(\Theta_{inc})F(\Theta)}G_c\Gamma_{nm} = \beta_{nm}(\Theta_{inc}, \Theta)\mathrm{e}^{\mathrm{j}\phi_{nm}}$$

where we adopt the conventional spherical coordinate system in which it holds $\phi \in [0,2\pi)$ (azimuth) and $\theta \in [0, \pi)$(inclination). Here, $F(\Theta)$represents the normalized power radiation pattern, accounting for potential non isotropic behaviour, of the radiation element; G_c is the boresight antenna gain; Γ_{nm} denotes the cell-specific load reflection coefficient, $\beta_{nm}(\Theta_{inc}, \Theta)$ is the reflection coefficient amplitude, and ϕ_{nm} is the reflection coefficient phase. Note that a more rigorous model should also account for the signal reflected by the antenna according to its structural radar cross section component. $F(\Theta)$ is given by

$$F(\Theta) = \begin{cases} \cos^q(\theta), & \theta \in [0, \pi/2)\,, \phi \in [0,2\pi) \\ 0, & otherwise \end{cases}$$

The parameter q is contingent upon the specific technology adopted and the dimension of the cell, and it is correlated with the boresight gain, i.e., $G_c = 2(q+1)$. Following an approach similar to [37], one possibility is to set G_c so that the effective area of the cell A_c is equal to the area of the cell, i.e., $G_c = A_c \frac{4\pi}{\lambda}$, assuming an ideal radiation efficiency. Considering a cell with $\frac{\lambda}{2}$, it follows that $G_c \approx 5\ dBi$ and $q = 0.57$. A similar model is presented in [3] with $q = 3$. The load reflection coefficient is given by

$$\Gamma_{nm} = \frac{\mathrm{Z}_{nm} - \mathrm{Z}_0}{\mathrm{Z}_{nm} + \mathrm{Z}_0}.$$

Through meticulous design of the impedance Z_{nm} at each cell, diverse reflective behaviours of the metasurface can be achieved. As indicated in the previous equation, it becomes apparent that realizing the ideal model, which assumes a maximum (unit) reflection amplitude regardless of phase shift—commonly employed in the literature—is challenging in practical applications. Specifically, the minimum amplitude occurs near zero phase shift and approaches unity at $-\pi$ and π. This phenomenon arises because as the phase shift approaches zero, image currents align in-phase with reflecting element currents, resulting in increased energy loss and consequently lower reflection amplitude. Additionally, the resistive component of Z_{nm} cannot be zero in practice. For instance, varactor diodes, typically employed in realizing programmable RISs, exhibit a typical resistance of 2.5 Ohm. Consequently, RISs must strike a balance between reflection amplitude and phase alignment [60].

The model does not account for mutual coupling that may arise between closely situated cells, potentially impacting the optimization and performance of RIS-aided wireless communication. In [61], the authors develop a circuit-based model where cells are characterized as coupled short dipoles, representing the RIS in terms of impedance matrices conducive to optimization tools [62]. However, this model does not consider the potential presence of a shielding plane near the RIS and diverse antenna element structures. A recent example of an accurate yet straightforward analytical model for computing the reflection amplitude and phase of RIS can be found in [62,32]. This model relies on a transmission line circuit representation of the RIS, encompassing the physics behind the structure, including the impact of all pertinent geometrical and electrical parameters. The proposed representation of the RIS enables consideration of the effects of incidence angle, mutual coupling among elements, and the interaction of the periodic surface with the RIS ground plane.

In the context of frequency-selective and passive metasurfaces – metaprism - mentioned in section **Error! Reference source not found.**, the load reflection coefficient Γ_{nm} is frequency-dependent and, according to its design, it is possible to realize different reflecting behaviour of the metasurface.

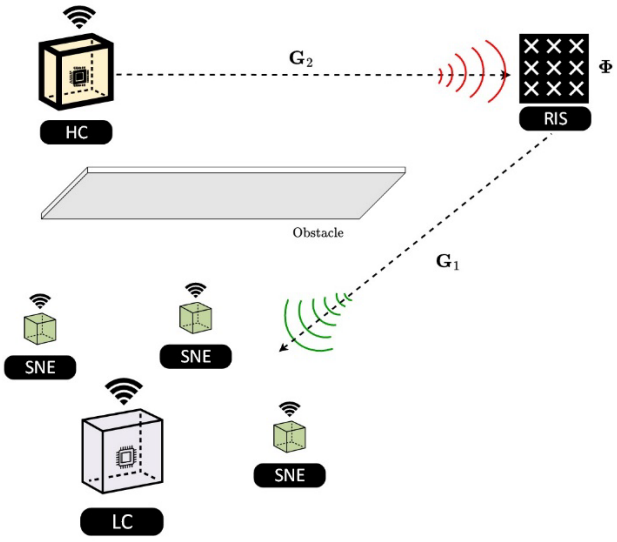

FIGURE 3 RIS-AIDED NLOS SCENARIO IN AN INDUSTRIAL IN X-SUBNETWORK

Transitioning to a system level use of the model, let us consider the reference scenario in Figure 3, representing an industrial subnetwork with a high density of sensors in a specific three-dimensional space requiring coverage even in Non-Line-of-Sight (NLOS) conditions due to obstacles. The RIS facilitates the establishment of a virtual Line-of-Sight (LOS) propagation condition between the transmitter (TX) and the monitored area. Suppose that the TX is equipped with an antenna array composed of N_t antennas and the RX with Nr antennas. The RIS has $K = NxM$ cells each of them characterized by the reflection coefficient r_{nm} , $n = 1,2,\dots,N, m = 1,2,\dots M$, defined before. We stack the K coefficients into the vector $\boldsymbol{r}$ of size K and define the diagonal $K\ x\ K$ matrix $\boldsymbol{\Phi} = diag(\boldsymbol{r})$ (often denoted to as $\mathbf{T}$) characterizing the reflection characteristics of the RIS. Denote with $\boldsymbol{G_2}$ the $K\ x\ Nt$ channel matrix of the MIMO link TX-RIS and with $\boldsymbol{G_1}$ the $Nr\ x\ K$ channel matrix of the MIMO link RIS-RX. The cascade TX-RIS-RX channel is given by [63]

$$\boldsymbol{G} = \boldsymbol{G_1}\,\boldsymbol{\Phi}\,\boldsymbol{G_2}$$

with

$$\Phi_{nm} = -\frac{2\pi n d_x}{\lambda}(u_x(\Theta_{inc}) + u_x(\Theta)) \quad -\frac{2\pi m d_y}{\lambda}(u_y(\Theta_{inc}) + u_y(\Theta))$$

where we have defined the quantitiesu_x $u_x = \sin\theta\cos(\phi)$, $u_y = \sin\theta\sin\phi$, and $d_y = d_x \approx \frac{\lambda}{2}$, being d_x and d_y the elements spacing in the x and y directions, respectively.

In the near field propagation regime, where the plane wave approximation no longer holds, the design of the RIS becomes more challenging. In [63], the optimal configuration of the RIS that maximises the mutual information has been found. In particular, it is shown that in general the optimal RIS must be characterized by a non-diagonal matrix $\boldsymbol{\Phi}$ even though for conventional geometry the adoption of a diagonal RIS provides a good approximation.

The model for the reflection coefficients r_{nm} above implicitly assumes that no coupling is present between the elements of the RIS leading to a diagonal matrix $\boldsymbol{\Phi}$. To ensure broader applicability, RISs characterized by a non-diagonal matrix $\boldsymbol{\Phi}$ have been introduced [64,65,66], where also the coupling between elements can be tuned thus offering more design flexibility and spatial selectivity at the expense of a higher complexity (see also section 3.2). In any case, due to the passive and lossless attributes inherent in the RIS, the matrix must be unitary, i.e., $\boldsymbol{\Phi}^{\boldsymbol{H}}\boldsymbol{\Phi} = \mathbf{I}$. A non-diagonal low-rank matrix can also be obtained through a NCR which has been standardized in 3GPP Rel-18 [104,105].

2.2.2 METASURFACES AS IMPEDANCE SHEET

Typically, metasurface-based RISs are characterized by an extremely thin nature (i.e., thickness much smaller than the wavelength) [33, 34, 40, 41, 42,44, 45, 46, 47, 55]. The composite structure constituting these metasurfaces is assumed to exhibit material-like behaviour in the electromagnetic sense, allowing for homogenization on the wavelength scale. Consequently, the metasurface can be effectively characterized by its surface-averaged properties. The parameters of these metasurfaces result from the two-dimensional surface averaging of microscopic currents on the same wavelength scale. This implies that the unit cell sizes of composite metasurfaces are considerably smaller compared to the wavelength.

In terms of EM response, these metasurfaces reflect and transmit plane waves akin to sheets of homogeneous materials (referred to as impedance sheets), distinguishing them from diffraction gratings that produce multiple diffraction lobes. Metasurfaces can be conceptualized as effective two-dimensional structures designed to control the relationships between EM field values on the two sides of the engineered sheet. This enables the realization of complete control over reflected and transmitted waves using a thin sheet. Following Huygens' principle, the electromagnetic fields generated by arbitrary sources in a given volume V can be represented by equivalent currents on the surface of that volume [44]. The conventional approach of utilizing metamaterials for controlling and transforming electromagnetic fields involves engineering artificial materials in such a way that induced polarization and conduction currents act as secondary sources, creating the desired fields inside or outside the metamaterial sample.

Metasurfaces that are electrically and magnetically polarizable, with thickness much less than the wavelength, can be constructed using small orthogonal electric and magnetic dipoles tangential to the surface. These dipoles, acting as meta-atoms or unit cells, generate surface magnetic currents and electric currents, forming a dense set of Huygens sources [45, 43]. For instance, an omega-shaped particle proposed in [67], can serve as meta-atom. Generally, a metasurface is a composite planar layer comprising periodically arranged electrically small cells, which are polarizable both electrically and magnetically. The electromagnetic properties of these cells can be described by linear relations between the induced electric and magnetic dipole moments and the incident fields at the cell positions. The amplitudes and phases of the reflected and transmitted plane waves depend solely on the surface-averaged electric and magnetic current densities J_e and J_m, flowing on the metasurface, which are related to the induced cell dipole moments. Homogenization models elucidate the relationships between the induced surface current densities and the averaged electric and magnetic fields on the metasurface. These models express the relations between the surface-averaged tangential electric and magnetic fields on the two sides of the metasurface since surface current densities are equivalent to jumps in the tangential components of the surface-averaged fields [68].

In this context, we focus on perfectly reflecting metasurfaces, which have garnered significant attention in the communication theory community. However, recent interest in hybrid reflecting/transmitting metasurfaces has emerged within the same community [69]. In the case of perfectly reflecting metasurfaces, assuming zero fields behind the metasurface, the boundary condition at a location x on the surface can be expressed as

$$\boldsymbol{E}_t(x) = Z(x)\boldsymbol{n} \times \boldsymbol{H}_t(x)$$

In the context where $\boldsymbol{E}_t(x)$ and $\boldsymbol{H}_t(x)$ represent the tangential electric and magnetic fields, respectively, $\boldsymbol{n}$ is the vector perpendicular to the surface, and $Z(x)$ denotes the impedance of the surface, the tangential components of the wavevector dictate the variation of $Z(x)$ along the axis x. For the sake of simplicity in illustration, we consider the variation of $Z(x)$ along the axis x, which is directed along the tangential component of the wavevector. Depending on the specific technology employed, the position-dependent impedance of the surface (impedance sheet) can be intentionally designed. The methodology for mapping the desired impedance profile to the specific design of each unit cell composing the metasurface is contingent on the technology in use. Examples illustrating this mapping process can be found in [47, 48, 50, 51, 33], as well as in related references.

The prevailing method for characterizing a reflecting metasurface, often referred to as a metamirror, involves the application of the generalized reflection law, a concept commonly used in optics. This characterization is achieved by assuming a single incident and reflected plane waves. As per the generalized reflection law, the local reflection coefficient is defined as the ratio between the incident and reflected tangential electric fields at each point x of the metasurface [47, 48, 70, 48].

$$r(x) = \beta(x)\, e^{j\phi(x)} = \frac{\boldsymbol{E}_t^{(i)}(x)}{\boldsymbol{E}_t^{(r)}(x)}$$

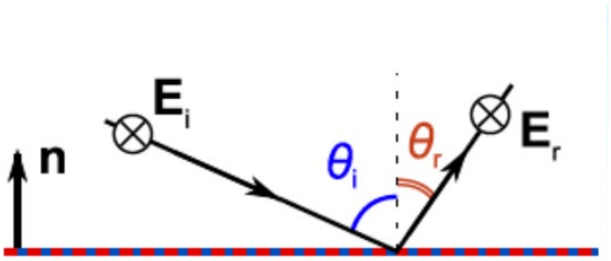

FIGURE 4 ILLUSTRATION OF THE DESIRED PERFORMANCE OF AN IDEALLY REFLECTING METASURFACE AS IMPEDANCE SHEET [33].

where $\phi(x)$ and $\Theta(x)$ represent the position-dependent reflection amplitude and phase, respectively. Consider the scenario where the design objective is to achieve complete reflection of a plane wave originating from a specific direction θ_i into another plane wave propagating in a different and arbitrary direction θ_r (refer to Figure 4). In this case, we examine the situation where the polarization of the reflected wave aligns with that of the incident wave and involves transversal electric (TE) incidence so that

$$\boldsymbol{E}_t^{(i)}(x) = \boldsymbol{E}^{(i)}(x)$$

$$\boldsymbol{E}_t^{(r)}(x) = \boldsymbol{E}^{(r)}(x)$$

$$\boldsymbol{H}_t^{(i)}(x) = \cos(\theta_i)\boldsymbol{H}^{(i)}(x) = \cos(\theta_i)\frac{\boldsymbol{E}^{(i)}(x)}{\eta}$$

$$\boldsymbol{H}_t^{(r)}(x) = -\cos(\theta_r)\boldsymbol{H}^{(r)}(x) = -\cos(\theta_r)\frac{\boldsymbol{E}^{(r)}(x)}{\eta}$$

where η is the free-space impedance. The incident and reflected electric fields on the metasurfaces (setting $\beta(x) = 1$ for full reflection) are

$$\boldsymbol{E}^{(i)}(x) = E^{(i)}(x)e^{-jksin(\theta_i)x}$$

$$\boldsymbol{E}^{(r)}(x) = E^{(i)}(x)r(x) = E^{(r)}e^{-jksin(\theta_i)x + j\phi(x)}$$

In the given context, where $k = \frac{2\pi}{\lambda}$ is the wave number, and $E^{(i)}(x) = E^{(r)}(x)$ we maintain generality by assuming that the reflected plane wave can exhibit any desired phase shift $\phi(x)$ concerning the incident wave. Employing these notations, the origin of the x axis can be selected such that both $E^{(i)}$ and $E^{(r)}$ are real-valued vectors. In this scenario, the desired field distribution at the surface of the metasurface is the superposition of two plane waves, that are the incident and reflected waves:

$$\boldsymbol{E}_t(x) = \boldsymbol{E}_t^{(i)}(x) + \boldsymbol{E}_t^{(r)}(x)$$

$$\mathbf{H}_t(x) = \boldsymbol{H}_t^{(i)}(x) + \boldsymbol{H}_t^{(r)}(x)$$

By substitution we obtain

$$\boldsymbol{E}_t(x) = E^{(i)}(x)e^{-jksin(\theta_i)x} + E^{(r)}e^{-jksin(\theta_i)x + j\phi(x)}$$

$$\mathbf{H}_t(x) = \frac{E^{(i)}(x)}{\eta}e^{-jksin(\theta_i)x} + \frac{E^{(r)}}{\eta}e^{-jksin(\theta_i)x + j\phi(x)}$$

To obtain a reflection angle θ_r, the phase of the reflection coefficient must satisfy the following relationship

$$k\ sin(\theta_i)\ x\ +\ \phi(x) = k\ sin(\theta_r)\ x\ .$$

It is noteworthy that the phase does not exhibit uniformity across the surface. By differentiating the equation, one can ascertain the relationship between the incidence and refraction angles in relation to the gradient of the reflection coefficient phase.

$$\frac{d\phi(x)}{dx} = k(sin(\theta_i) - sin(\theta_r))\ .$$

This outcome implies the most straightforward method for implementing refractive surfaces: creating a locally periodic surface where the absolute value of the transmission coefficient is unity (representing a lossless Huygens' sheet), and the phase of the transmission coefficient linearly varies as described in the previous equation. The surface impedance of such a metasurface, capable of generating a single plane wave in the desired direction, can be determined by combining previous formulas such that

$$Z(x) = \eta\frac{e^{-j\ k\ sin(\theta_i)\ x} + e^{-j\ k\ sin(\theta_r)\ x}}{cos(\theta_i)e^{-j\ k\ sin(\theta_i)\ x} - cos(\theta_r)e^{-j\ k\ sin(\theta_r)\ x}}\ .$$

Nevertheless, adopting this approach does not yield the desired perfect reflection. Subsequently, we will elucidate how the intended performance can be achieved precisely [48]. In essence, $\Phi(x) = 1$ (or more generally $\Phi(x) \leq 1$) implies imposing local passivity (or passiveness with losses) on the metasurface. In such a scenario, the power efficiency of the metasurface, defined as the ratio between the power of the reflected plane wave and the power of the incident plane wave, indicates that an increase in the reflection angle results in a decrease in power efficiency by a factor of $\frac{\cos\Theta_r}{\cos\Theta_i}$. Indeed, achieving ideal reflection into a single plane wave without any power loss is feasible, but only if we permit periodic flow of power into the metamirror structure and back into space. It can be demonstrated that this holds if the amplitude of the reflection coefficient equals [48]

$$\beta(x) = \frac{\sqrt{cos(\theta_i)}}{\sqrt{cos(\theta_r)}}\ .$$

While the metasurface achieves the intended function perfectly, it is imperative to note that the response must exhibit strong nonlocal characteristics: the power absorbed in specific regions of the metasurface structure must be propelled back from other areas. Alternatively, perfect reflection can be attained if the metasurface incorporates active and lossy elements, albeit maintaining an overall lossless nature when averaged over the surface area. This, however, comes at the cost of increased implementation complexity. In essence, the metasurface is not locally passive but globally passive. The primary constraints of the design based on the generalized reflection law, typical in optics, are associated with the assumption of an infinite-sized surface and the local homogeneity assumption. It is crucial to observe that, in accordance with the definition of $\beta(x)$, the local reflection coefficient establishes the relationship between the incident and reflected fields for each point as if the metasurface were locally homogeneous. This implies that waves incident at any point are specularly reflected, albeit with varying phases at different points. Consequently, employing the local reflection coefficient for modelling metasurfaces in far-field scattering calculations may not always be accurate. A homogeneous interface, such as the boundary between two plain dielectrics, supports specular reflection. In this case, when illuminated by a plane wave, any percentage of power reflected by such an interface is directed into a single wave propagating away from the surface in the mirror direction. However, when the interface is not homogeneous, the scattered

wave is generally a combination of all plane waves in the radiation continuum. For a periodic structure, their integral sum straightforwardly reduces to discrete waves propagating toward specific directions, representing the discrete diffraction orders. As per the Floquet theory, periodical variations in metasurface properties give rise to multiple diffracted modes dependent on the illumination angle, period, and frequency.

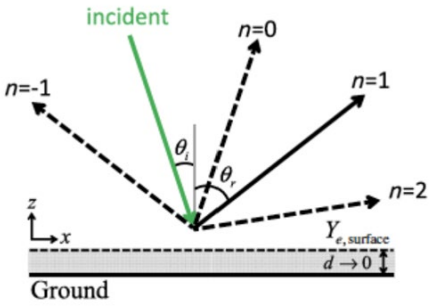

FIGURE 5 FLOQUET MODES [47]

Specifically, in accordance with the Floquet theory, selecting the spatial periodicity of the structure, *D*, along the *x*-axis enables the definition of the propagation directions of reflected modes. When an infinite periodic metasurface is illuminated by a plane wave at the incident angle θ_i, the reflected field is defined as a superposition of plane waves propagating in different directions, as illustrated in Figure 7, according to the relation [47, 71]

$$\sin\theta_{rn} = sin\theta_i + \frac{2\pi n}{k\,D}$$

where θ_{rn} represents the reflection angles of the propagating harmonics with an index $n = \ldots, -2, -1, 0, 1, \ldots$. The presence of multiple propagation directions precludes the use of a singular reflection coefficient. To address this, a reflection coefficient for modelling metasurfaces has been introduced in [71], defined as a composite of individual reflection coefficients for each propagating reflected mode as

$$r(x) = \sum_n r_n e^{-jk(sin\theta_{rn} - sin\theta_i)x}$$

where r_n represents the ratios of the complex amplitudes of the propagating Floquet harmonics for the tangential reflected and incident electric field components at the metasurface plane. These coefficients correspond to the individual reflection coefficients for each propagating diffracted mode. The effective reflection coefficient defined by the aforementioned formula characterizes the macroscopic response of the metasurface and proves valuable in calculating the reflected and scattered fields in the far-field. Its utility becomes evident when characterizing the angular response of the metasurface for arbitrary illuminations, providing effective design tools for wireless communication systems and other applications. This is particularly essential in realistic dynamic or multipath scenarios where metasurfaces are illuminated from various directions and observed from angles different from the intended reflection angle.

To compute the individual reflection coefficients of each reflected mode and, consequently, the macroscopic reflection coefficient $r(x)$ defined above, the starting point involves imposing a spatially varying surface impedance. This impedance can always be locally defined as the ratio between the tangential components of the surface-averaged electric and magnetic fields. The averaging is performed on the scale of the unit cells of the metasurface. The surface impedance denoted as $Z(x)$ is a periodic function of the coordinate x ($Z(x) = Z(x + D)$). The incident power is distributed among the propagating modes based on the surface impedance of the metasurface. The propagation direction of diffracted modes strongly depends on the illumination angle, and for different illumination angles, the propagation directions of reflected waves change. Furthermore, this dependence varies for different diffracted modes. The use of the surface impedance model enables the numerical investigation

of power distribution among all diffracted modes are analysed using the mode-matching method, where the amplitudes of all Floquet harmonics are computed by enforcing the impedance boundary condition. This method has recently been applied to analyse metasurfaces, facilitating rapid calculations of scattering parameters [71].

While the above analysis serves as a valuable tool for infinite metasurfaces extending over a whole plane, it becomes imperative to consider the scattering pattern of metasurfaces in realistic scenarios with finite sizes. A number of approaches are available for real-life, finite-size metasurfaces. Of course, electromagnetic simulation represents the reference, most accurate method. However, full-wave simulation is impractical when link-level or system level simulation in presence of metasurfaces needs to be addressed due to the unbearable computation time and/or memory requirements. Therefore, more efficient, simplified and yet electromagnetically consistent methods, also known as "macroscopic models", must be used. It is evident from the previous paragraphs that a metasurface can be represented using a given surface impedance function, or in alternative using a proper reflection coefficient, or better, "spatial modulation function". In alternative periodic, or locally-periodic, metasurfaces can be represented as diffraction gratings. Based on these descriptions, a number of models for real metasurfaces have been proposed. In [71], a method based on Floquet harmonics is presented that provides accurate expressions for the scattered field of finite-size periodic metasurfaces. The main analysis, however, is limited to the far field only. The scattering of finite-size anomalous reflectors was explored in another recent study [72] where physical optics and the vector Huygens principle are applied to model near-field and far-field scattering from a finite-size RIS using an integral field expression.

Although not as rigorous as those mentioned above, the model proposed in [73] for reflecting metasurfaces, is simpler and also takes into account the impact of diffuse scattering that may be caused by construction inaccuracies, or phase errors with respect to the value of design, which are common when using control networks with discrete-phase rotation states. The model assumes that the metasurface can be described as locally periodic, and each surface element can be characterized using a "spatial modulation coefficient" and a few parameters representing the relative intensities of the different reradiation mode, including the desired mode, the parasitic modes and diffuse scattering, and must satisfy a physical soundness power balance:

$$P_i = P_i R^2 \sum_{n=1}^{N} m_n + P_i \tau + P_i S^2$$

where τ represents the fraction of the incident power that is dissipated into heat, S^2 is the fraction of the incident power that is scattered due to imperfections, and R^2 accounts for the corresponding attenuation of the N reradiation modes of relative intensity m_n. For each reradiation mode, the spatial modulation coefficient at surface position (x,y) has the following form:

$$\Gamma(x,y) = R\sqrt{m_n}\, A(x,y)\, exp\big(j\chi(x,y)\big)$$

where $A(x,y)$ and $\chi(x,y)$ are the amplitude and phase modulation that the metasurface applies to the reradiated field. Note that the amplitude term $A(x, y)$ is introduced to take into account power transfer effects on the surface in non-local metasurfaces. The spatial modulation coefficient can also be generalized into a matrix coefficient that also takes into account polarization, as shown in [74]. The field is then computed for each reradiation mode using a Huygens-based approach, while the so called "Effective Roughness" model is applied to compute the diffuse scattering field. A "radiation integral" is used to compute each mode's field as the superposition of the contribution of wavelets generated by each surface element, in agreement with the Huygens approach.

A discrete version of the model, called "Antenna-Array-Like" (AAL) method, is then derived in section III.B of [73], which has a simpler, discrete summation formulation, and greater computational efficiency. Moreover, it is very suitable to model metasurfaces realized as arrays of tuneable antenna elements, for which it basically boils down to an electromagnetically consistent version of the antenna array models described in section 2.2.1 of this document.

More recently, based on a similar parametric power-balance and spatial modulation coefficient representation, a fully ray-based model has been derived for the computation of the field for each reradiation mode [74]. On the base of the gradient of the local spatial modulation coefficient, the anomalous reflection angle of the reflected field is computed. Moreover, using its second order derivatives, which are related to the local curvature of the reradiated wavefront, the spreading factor of the ray is determined. Edge effects of finite-size metasurfaces are also taken into account through a generalized version of Uniform Theory of Diffraction (UTD) theory that allows to determine direction and characteristics of diffracted rays on the edge of the surface.

2.2.3 INTEGRATION OF RIS MODELS INTO RAY TRACING PLANNING TOOLS

In order to deploy RISs in a complex propagation environment, as the ones corresponding to the aforementioned subnetworks and use cases, a planning tool able to efficiently predict the reradiated field by a RIS and its interaction with the surrounding objects is needed.

Electromagnetic propagation in presence of a metasurface is a complex process that involves microscopic propagation phenomena (coupling between meta-atoms, surface waves, etc.) within the metasurface structure. Metasurfaces, and therefore RIS, are far from showing an ideal behaviour: they actually show dissipation, diffraction, diffuse scattering and multiple reradiation modes, despite only one of them is usually the desired one. Although microscopic propagation phenomena are crucial for the small-scale application of metasurface technology to antennas and devices, only the overall, macroscopic behaviour in terms of radiative near-field and far field scattering is relevant for their simulation, design and use for wireless networks. Full-wave, electromagnetic methods that are necessary for proper simulation of the microscopic propagation phenomena are impractical for the purpose due to their computational burden. A good trade-off between performance and accuracy is given by ray tracing models, based on Geometric Optics and its extensions, such as the UTD. A suitable approach is then based on the integration of ray tracing models with the macroscopic RIS reradiation models described in section 2.2.2 such as the AAL model or the fully ray-based approach.

In [75], the AAL model described in section 2.2.2 has been embedded into a 3D ray-tracing simulator developed at CNIT [76]. Since the AAL model expresses anomalous reflection from the RIS as a sum of multiple contributions from each one of its surface elements, and not as a set of rays that satisfy Geometric Optics rules, the AAL model doesn't seamlessly "blend" within the ray-tracing algorithm: anomalous reflection can only be handled in a straightforward way as the last interaction of the ray-chain. Nevertheless, exploiting the reciprocity of the radio link, and by swapping Tx and Rx positions for the purpose, we have been able to take into account also multiple-bounce rays experiencing RIS scattering as the first interaction of the chain. The field contributions of such rays have been added to the final result in order to obtain a realistic estimate of Radio Frequency (RF) coverage in presence of a RIS.

A more general approach is the full integration in ray tracing tools of the macroscopic model presented in [74]: being fully ray-based, such method does not suffer of the aforementioned limitation and the RIS can be located in any point of the interaction chain. Moreover, this model is far more efficient than AAL and other Huygens-based computation methods, while the degradation of the prediction accuracy is negligible, as shown in [74].

2.3 IDENTIFICATION OF RIS TECHNOLOGIES/MODELS FOR IN-X SUBNETWORKS

In this section, for each use case of subnetworks categories described in WP2, the most suitable intelligent surface technology, among those surveyed in section 2.1, is identified along with the purpose and expected benefit in terms of KPIs improvement. This analysis must be intended as preliminary because it has to be corroborated by numerical investigations. To this aim, for the most promising use cases, some preliminary design and optimization methods are presented in sections 3, 4, and 5 and others will be developed and assessed in the next project period.

TABLE 5 SUITABLE RIS TECHNOLOGIES FOR CONSUMER SUBNETWORKS CATEGORY USE CASES

➢ **Consumer Subnetworks Category Use Cases:**
1. ***Immersive Education***
– **Description:** It aims to enhance interactive experience, beyond what it is possible within an ordinary classroom, or for field excursions like historic sites, museums etc. To provide tutorial footage allowing an almost "hands on" experience to be used with a generic device. – **RIS-aided KPIs :** Full-duplex coverage extension at low cost and without additional latency
– **Suitable RIS technology:** *Purpose:* Enable steering of beams towards individual users within a room. *Technology and design methods:* RISs can be considered in this use case to cover slowly dynamic situations where the movement of users is not predefined. Real-time optimization algorithms as well as control protocols must be designed.
2. ***Indoor Interactive Gaming***
– **Description:** Extended reality (XR) in a place equipped with some equipment like sensors, the access point (AP) and its antennas are placed in optimal location, and a high-end edge cloud server is located or attached together with the AP. These sensors are used to obtain user(s) poses / orientations and then later to be used for the XR scene generation. All of those sensor devices can communicate locally to an AP within a subnetwork. There is also an edge cloud server that can be built-in to the AP or separately. Game participants are wearing the Virtual Reality (VR) headsets and are equipped with sensors which are attached to their bodies. – **RIS-aided KPIs:** Full-duplex coverage extension at low cost and without additional latency
– **Suitable RIS technology:** *Purpose:* Enable steering of beams towards individual users within a room *Technology and design methods:* RISs can be considered in this use case to cover dynamic situations where the movement of users/sensors is not predefined. Real-time optimization algorithms as well as control protocols must be designed.
3. ***Virtual content production***
– **Description:** This use case is about virtual content production of live music. Performers produce 3D video content that can be live or uploaded to social media. Performers in different locations perform live together. Audience in different places far from the live studio (e.g., their home) can view content at different angles of the production by using XR device. Multiple professional cameras and multiple microphones are installed in a live studio where performer(s) will perform and are connected wirelessly with the respective subnetworks. The performer(s) in different geographical location is(are) equipped with similar installations. – **RIS-aided KPIs:** High data rate. Full-duplex coverage extension at low cost and without additional latency.
– **Suitable RIS technology:**

Purpose: Enable steering of beams towards individual users within a room. ***Technology and design methods***: Since this use case is mainly indoor and in a stationary place, the RIS would be an attractive technology to achieve ultra-high data rate. RIS could be useful for deploying multiple transmission/reception points (TRP) operation with lower cost. In cases with multiple subnetworks, RIS-induced interference may become problematic, wherefore non-diagonal RISs may be superior.
4. ***Augmented Reality (AR) Navigation***
– **Description:** The AR device via the glasses provides the augmented reality image containing the information that could be useful to the user. The AR device may also be equipped with sensors, microphone, camera, speaker, and communication module. An Artificial Intelligence (AI)/Machine Learning (ML) server is used to assist the user by providing the user's desired information based on various input to the server. In practice, this operation is inspired by the usage of an AI/ML tool where the user asks a question, and the answer is later provided by the AI/ML tool. In our case, the user may have interactive communication so that she/he provides the enquiry and receives the intended information, such as the best location and best route to the destination. **RIS-aided KPIs:** Full-duplex coverage extension of NLOS conditions at low cost and without additional latency
– **Suitable RIS technology:** *Purpose:* Enable steering of beams towards AR devices. *Technology and design methods:* RISs can be considered in this use case to cover dynamic situations where the movement of users/sensors is not predefined. Real-time optimization algorithms as well as control protocols must be designed. The adoption of RISs in this use case appears very challenging and its benefit not evident.

TABLE 6 SUITABLE RIS TECHNOLOGIES FOR INDUSTRIAL SUBNETWORKS USE CASES.

➢ **Industrial Subnetworks Use Cases:**
1. ***Robot Control***
• **Description:** Robot control operations are usually relying on wired industrial technologies such as Profinet Isochronous Real-Time (IRT) or EtherCAT. This use case aims at translating such wired communication technologies over wireless, while maintaining cycle times and expected quality of service. The purpose of the use case is the control of moving and rotating parts in printing machines, force control, packaging machines, or machine tool. • **RIS-aided KPIs:** Compared to relays or the deployment of additional APs, RIS allows to keep the latency and jitter at the sub-ms and us levels, respectively, being the RIS passive from the EM viewpoint. In addition, the generation of virtual paths through the RIS enhances the diversity and hence the reliability of the wireless link. Since the subnetwork density can be very high, therefore generating potentially high level of mutual interference, the presence of RISs might help in shaping the interference thus reducing its effect and allowing the coexistence of a large number of sensors.
• **Suitable RIS technologies** *Purpose:* The RIS can be installed in proximity of robots and machineries, to create the favourable propagation conditions, counteract blockage effects, increase the coverage, and limit the interference. *Technology and design methods:* Both non-reconfigurable intelligent surfaces (N-RIS) and reconfigurable intelligent surfaces (RIS) can be considered in this use case. N-RIS is suitable to extend the coverage when the TX/RX are fixed or moving along the same pre-defined trajectory. The N-RIS can be designed during the fabrication phase starting from Ray-tracing evaluations. RIS is suitable to cover more dynamic situations where the movement is not predefined. In this case, real-time optimization

algorithms as well as control protocol must be designed. For RISs, (i.e., not N-RIS), a non-diagonal transfer matrix architecture offering spatial selectivity appears promising to avoid interference.

2. ***Unit test cell***

- **Description:**
  A unit test cell is meant to perform quality assurance tasks of product parts in the manufacturing process, as well as of devices used in the manufacturing process. For example, it can be used for providing calibration and tolerance figures for actuators to be used in a factory, to make sure they comply with predefined requirements during execution. The purpose of the use case is the quality assurance tasks of product parts in the manufacturing process.
- **RIS-aided KPIs:**
  RIS allows to keep the latency and jitter at the sub-ms and us levels, respectively. In addition, the generation of virtual paths through the RIS enhances the diversity and hence the reliability of the wireless link. To ensure support cycle times (below 1 ms) and the probability of having two consecutive errors < 10^{-6}, RIS can be deployed to counteract blockage effects without increasing the latency.

- **Suitable RIS technology:**
  Purpose: The RIS can be installed in proximity of the cell to create the favourable propagation conditions, counteract blockage effects, increase the coverage, and limit the interference.
  Technology and design methods: N-RISs seem more appropriate for this use case. The N-RIS can be designed during the fabrication phase starting from Ray-tracing characterization of the cell.

3. ***Visual inspection cell***

- **Description:**
  A visual inspection cell performs quality assurance in the manufacturing process by means of video feeds. The video feeds are processed, and quality control is performed, by eventually outputting commands to actuators in case actions are to be taken for improving operation quality. The purpose of the use case is the quality assurance in the manufacturing process by means of video feeds.
- **RIS-aided KPIs: N/A**

- **Suitable RIS technology:**
  Purpose: The deployment of RISs appears not particularly advantageous in this use case.
  Technology and design methods: N/A

4. ***Subnetworks swarms: subnetwork co-existence in factory hall***

- **Description:**
  In many manufacturing processes, particularly those in the electronics or automotive sector, tasks can be distributed among a swarm of smaller, specialized robots. Each robot is configured to perform a specific function or a series of functions. Working in concert, these robotic swarms can assemble intricate products with an expected level of efficiency that may surpass conventional assembly lines. In this model, each robot not only performs its individual tasks but also shares information with the other robots in the swarm.
- **RIS-aided KPIs:**
  To ensure communication service availability with a minimum target value of 99.999%, RIS can be deployed to counteract blockage effects without increasing the latency.

- **Suitable RIS technology:**
  Purpose: The RIS can be installed in proximity of machineries to create the favourable propagation conditions, counteract blockage effects, increase the coverage, and limit the interference.
  Technology and design methods: RISs can be considered in this use case to cover dynamic situations where the movement of robots is not predefined. Real-time optimization algorithms as well as control protocol must be designed. From the preliminary results presented in this delivery it can be concluded that a NCR architecture appears to be a promising RIS technology; an NCR is a special type of RIS in which the transfer matrix is low rank. As an alternative, a standard RIS with element permutation can be considered; this is an example of a non-diagonal RIS architecture.

5. ***Subnetwork segmentation and management***

- **Description:**
  The information technology (IT) infrastructure security is realized through horizontal and vertical segmentation, or, in other words, through defence by depth and security zones. There is a certain

target factory layout with a physical and logical plan of factory assets incl. sensors, actuators, robots, Programmable Logic Controllers (PLCs), machines, etc. A subset of these assets needs to be put together in the form of a subnetwork as they will jointly perform a production target along a value chain. • **RIS-aided KPIs:** N/A
• **Suitable RIS technology:** ***Purpose:*** The deployment of RISs appears not particularly advantageous in this use case. **Technology and design methods:** N/A

TABLE 7 SUITABLE RIS TECHNOLOGIES FOR IN-VEHICLE SUBNETWORKS CATEGORY USE CASES

➢ **In-Vehicle Subnetworks Category Use Cases:**
1. ***Wireless zone electronic control unit (ECU): in-vehicle wireless subnetwork zone***
- **Description:** In-vehicle zone is characterized by the presence of sensors and actuators that might support automotive functions and systems from different in-vehicle domains. In the in-vehicle zone, there is also a zone ECU that manages and controls the sensors and actuators that are located in this zone. This use case considers that some of the cable links that connect the sensors/actuators to the zone ECU are replaced by wireless connections and that the zone ECU also takes the role of an AP to manage these wireless links. - **RIS-aided KPIs:** Increased coverage without the addition of latency and jitter.
- **Suitable RIS technology:** *Purpose:* To create the favourable propagation conditions inside the car hood / roof to increase the coverage and limit the interference. *Technology and design methods:* Non-reconfigurable intelligent surfaces (N-RIS), possibly non-diagonal, represent the best solution for this use case. Their design is very scenario-specific requiring off-line optimization algorithms exploiting ray-tracing tools.
2. ***Collaborative wireless zone ECUs: functions across multiple in-vehicle zones***
- **Description:** This use case covers automotive systems and applications that require (or benefit from) collaboration or offloading between functions, sensors and actuators located at different zones of the considered 6G-SHINE reference in-vehicle Electrical/Electronic (E/E) architecture. Each in-vehicle zone is characterized by the presence of a wireless zone ECU, which integrates sensors and actuators that might support automotive functions and systems of different in-vehicle domains. This use case covers automotive systems and services that require for their execution the interaction and cooperation between sensors, actuators and processing units located at different in-vehicle zones. - **RIS-aided KPIs:** N/A
- **Suitable RIS technology:** ***Purpose:*** The deployment of RISs appears not particularly advantageous in this use case. **Technology and design methods:** N/A
3. ***Inter-subnetworks coordination: collaboration between subnetworks in intra/inter-vehicle communications***
- **Description:** There are two levels of Radio Resource Management (RRM): 1. Intra-vehicular RRM: This optimizes the distribution of network resources among different components of the E/E architecture within a vehicle, ensuring smooth and uninterrupted communication. It also involves managing resources, for example, between different zones or components within the vehicle. 2. Inter-vehicular RRM: This manages potential interference between adjacent vehicles to prevent any performance degradation. This involves careful resource allocation to mitigate the risk of cross-vehicle interference, which becomes especially important when vehicles are close to each other.

This use case highlights the need for a sophisticated RRM system that can handle both these levels of management efficiently, ensuring optimal performance of the wireless subnetworks in an automotive E/E architecture.

- **RIS-aided KPIs:** N/A

- **Suitable RIS technology:**
  Purpose: The deployment of RISs appears not particularly advantageous in this use case.
  Technology and design methods: N/A

4. ***Virtual ECU: in-vehicle sensor data and functions processing at the 6G network edge***

- **Description:**
  This use case focuses on integrating the in-vehicle network with the 6G parent network, following the 6G 'network of networks' paradigm. The goal is to seamlessly extend the in-vehicle embedded computing capabilities to the edge/cloud. The connection from the in-vehicle network to the edge/cloud is exploited in this use case to enable opportunistic offload and vehicle-network-cloud cooperation to support advanced in-vehicle automotive functionalities critical for Autonomous Driving (AD) and the continuous evolution and advancement of vehicles. This use case utilizes the high capabilities of the in-vehicle High-Performance Computing Unit (HPCU) (and Connectivity Control Unit - CCU) to act as the bridge between the in-vehicle network and the 6G parent network. In this use case, the focus is on ensuring that offloading processing and functions from the in-vehicle network to the 6G network does not affect service provisioning, even if there are changes in the quality-of-service levels within the 6G parent network.
- **RIS-aided KPIs:** N/A

- **Suitable RIS technology:**
  Purpose: The deployment of RISs appears not particularly advantageous in this use case.
  Technology and design methods: N/A

3 PRELIMINARY RESULTS ON INTERFERENCE AND CO-EXISTENCE ASPECTS IN RIS-EQUIPPED SUBNETWORKS

In many industrial scenarios, a subnetwork is meant to co-exist with a microcell (e.g., an enterprise's wireless network). When the subnetwork is equipped with a RIS, potential problems arise. The reason being that the RIS may reflect signals from the microcell. For a static intelligent surface (i.e., an N-RIS), this is not of any concern as, from the microcell's perspective, the surface could be seen as any other point of reflection. However, for RISs, said reflections could be changed instantaneously, rendering the microcell with very little ability to estimate/predict the reflections based on reference signals. In section 3.1, we take a closer look at this issue, and in particular compare, from an interference perspective, two RIS implementations, namely a "standard RIS", and a Network Controlled Repeater (NCR). In section 3.2, novel spatially non-selective RISs are introduced as appealing solution to mitigate or avoid interference.

3.1 CO-EXISTENCE OF RIS-EQUIPPED SUBNETWORKS WITH MICROCELLS

3.1.1 TARGET KPIs/KVIs AND USE CASES

The material to be presented is general and targets most use cases, but with a strong focus on the industrial ones in which subnetworks are deployed within an already existing cell. Main KPIs addressed are interference mitigation and communication support for a large number of nodes.

3.1.2 PROBLEM STATEMENT

We consider a subnetwork operating within a microcell. We consider two cases, (i) separate frequency bands for the two networks, and (ii) the same frequency band. The effect that we study is that a RIS is reflecting all impinging signals. This implies that a RIS may potentially cause interference to the microcell. Further, also for separate frequency bands, the RIS may create interference as its reflection characteristics are typically not strongly bandlimited.

Herein, we shall compare two RIS implementations, namely a "standard RIS", and a Network Controlled Repeater (NCR) [104]. Further information about these is provided in section 3.2. The setup is a microcell equipped with a 6G Base Station (BS) serving a User Equipment (UE), and a subnetwork equipped with an Element with High Capabilities (HC) (or Element with Low Capabilities - LC) and a RIS/NCR serving a single SNE, as defined in deliverable D2.2.

3.1.3 RESULTS ACHIEVED SO FAR

A simulator according to 3GPP's 38.901 channel model, [77], has been implemented. The scenario considered is the indoor factory model; see [77]. Parameters of the channel model are provided in Table 8 Parameters for the simulator setup.

TABLE 8 PARAMETERS FOR THE SIMULATOR SETUP.

Parameter	Value
Channel model	TR 38.901
Scenario: HC – RIS/NCR	Indoor factory, LOS with probability 1
Scenario: all other links	Indoor factory, dense-high (= LOS with probability dependent on distance)

Dimension	120x60x10 m
Carrier frequency	3.8 GHz
Subcarrier spacing	15kHz
Number of subcarriers per system	512
Guard band between system operating in different bands	0
RIS/NCR antenna	Macro, 8dbi, TR 37.855
HC, 6G BS, and SNE antennas	Isotropic
Number of antennas at SNE and UE	1
Number of antennas at HC and 6G BS	1
Polarization	Single
RIS/NCR antennas	64
RIS/NCR amplification	30dB
RIS/NCR reflection bandwidth	1024 subcarriers (covers to bands)
HC, 6G BS, and RIS/NCR height	4m
SNE and UE heights	Uniform between 0.5m and 1.5m

As shown in the table above, we consider single antenna for the HC, 6G BSs, UE, and SNE, while an $M = 64$ antenna element RIS/NCR is employed. Our simulations are performed with 512 subcarriers, and we have assumed that the RIS has the same configuration across the entire band.

The received signal at the SNE, at subcarrier n, reads

$$y_{1,n} = h_{1,1,n}x_{1,n} + h_{2,1,n}x_{2,n} + x_{1,n}s_{1,n}Tt_{1,n} + x_{2,n}s_{2,n}Tt_{1,n}$$

while the received signal at the UE reads

$$y_{2,n} = h_{1,2,n}x_{1,n} + h_{2,2,n}x_{2,n} + x_{1,n}s_{1,n}Tt_{2,n} + x_{2,n}s_{2,n}Tt_{2,n}$$

where

- $h_{1,1,n}$ is the scalar channel from the HC to the SNE at subcarrier n, $h_{1,2,n}$ is the scalar channel from the HC to the UE at subcarrier n, $h_{2,1,n}$ is the scalar channel from the 6G BS to the SNE at subcarrier n, and $h_{2,2,n}$ is the scalar channel from the 6G BS to the UE at subcarrier n.
- $s_{1,n}$ and $s_{2,n}$ are the $1 \times M$ channel vectors from the HC and the 6G BS to the M RIS antennas, respectively, at subcarrier n.
- $t_{1,n}$ and $t_{2,n}$ are the $M \times 1$ channel vectors from the RIS to the HC and 6G BS, respectively, at subcarrier n.
- $x_{p,n}$ and $x_{p,n}$ are the data symbols transmitted by the HC and the 6G BS, respectively, at subcarrier n. All data symbols are independent and identically distributed.
- T is the $M \times M$ transfer function of the RIS.

For a standard RIS, we have that $T = diag(\exp(\mathrm{j}\phi_1)\ \ \exp(\mathrm{j}\phi_2)\ \ \ldots \exp(\mathrm{j}\phi_M))$ where $diag(\cdot)$ is a diagonal matrix with its argument along the main diagonal. However, for an NCR, we have a non-diagonal transfer function

$$T = [\exp(j\alpha_1)\ \ \ldots \exp(j\alpha_M)]^T[\exp(j\beta_1)\ \ \ldots \exp(j\beta_M)].$$

The difference between an NCR and a standard RIS is that the former is spatially selective, whereas the latter is not (see section 3.2.3.1 for further information on spatially selectivity).

The Signal-to-Interference Ratios (SIRs) at subcarrier n for the SNE and the UE, without any RIS, read, respectively,

$$\gamma_{1,n} = \frac{|h_{1,1,n}|^2}{|h_{2,1,n}|^2} \quad \gamma_{2,n} = \frac{|h_{2,2,n}|^2}{|h_{1,2,n}|^2}$$

With the RIS present, the corresponding SIRs become

$$\overline{\gamma}_{1,n} = \frac{|h_{1,1,n} + s_{1,n}Tt_{1,n}|^2}{|h_{2,1,n} + s_{2,n}Tt_{1,n}|^2} \quad \overline{\gamma}_{2,n} = \frac{|h_{2,2,n} + s_{2,n}Tt_{2,n}|^2}{|h_{1,2,n} + s_{1,n}Tt_{2,n}^2|}.$$

In selecting the optimal T, the optimal strategy is to perform a joint optimization, e.g., the ensuing capacity from T. This is SNR dependent and a very challenging optimization, wherefore we have chosen to optimize it according to

$$T = \arg\max_{\tilde{T}} \sum_n |s_{1,n}\tilde{T}\, t_{1,n}|^2$$

This is, still, not a trivial optimization due to the fact that T is built up from phasors. In order to solve it, we have relied on numerical optimization. We remark that the optimization is made for the subnetwork, i.e., the link HC-SNE, without taking the direct link $h_{1,1,n}$ into consideration. However, based on experiments beyond what is presented herein, we have noted that this assumption does not significantly alter our conclusions. Finally, we introduce the reference SIR.

$$\tau_1 = \frac{|h_{1,1,n} + s_{1,n}Tt_{1,n}|^2}{|h_{2,1,n}|^2}$$

which represents a benchmark SIR for a situation in which the RIS does not reflect any signal originating from 6G BS towards the subnetwork SNE.

In what follows we present our observations on the average gains γ_1, γ_2, $\overline{\gamma}_1$,$\overline{\gamma}_2$, and τ_1 when averaged over subcarriers (n) and channel realizations.

3.1.3.1. SAME FREQUENCY BAND FOR SUBNETWORK AND MICROCELL

We assume a simulation setup according to Figure 6 just below. The results for the averaged SIRs are provided in Table 9 corresponding to Figure 6. From the results in Table 9, we may observe that a RIS implementation in fact decreases the SIRs both for the subnetwork SNE and the microcell UE. We observe this by noting that $\gamma_p > \overline{\gamma}_p$ for $p = 1{,}2$. However, by noting that $\tau_1 = 21.7$ we can make the conclusion that the RIS is indeed boosting the received signal at SNE, but unfortunately it also reflects the 6G BS's signal towards the SNE, which results in an overall loss.

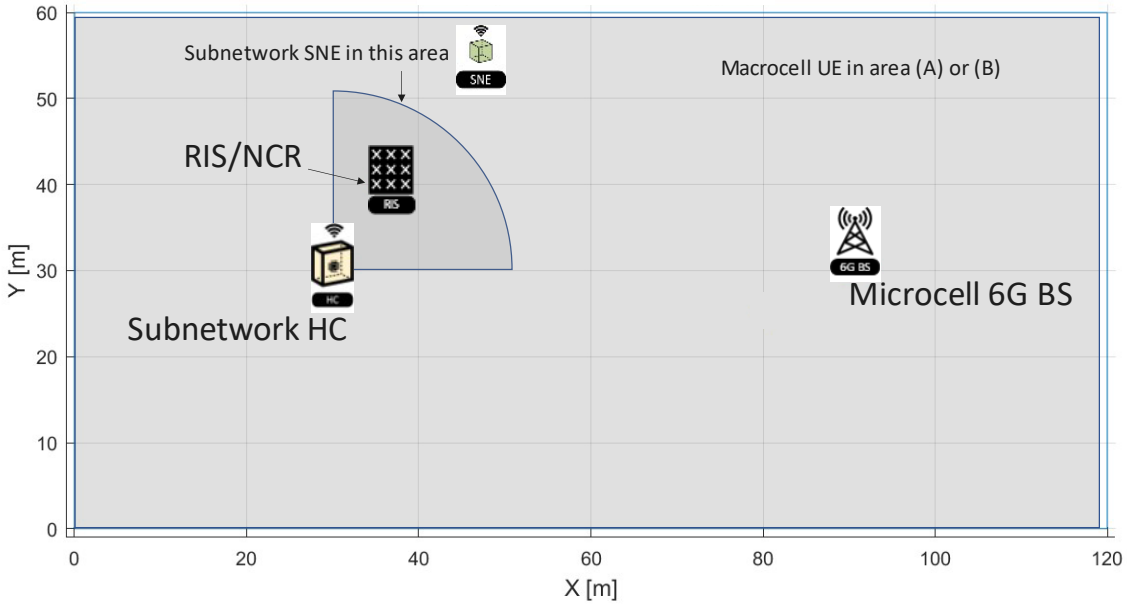

FIGURE 6 AN INDOOR FACTORY MODEL IS ASSUMED, WITH TWO 6G BSS SHARING THE FREQUENCY BAND

TABLE 9 AVERAGE SIRS CORRESPONDING TO FIGURE 6

SIRs [dB]	γ_1	γ_2	$\overline{\gamma}_1$	$\overline{\gamma}_2$	τ_1
RIS	10.7	10.8	8.6	9.3	22
NCR	10.7	10.8	12.2	6.7	22

For an NCR, the situation is somewhat different. For this case we have $\overline{\gamma}_1 > \gamma_1$ so the NCR indeed increases the SIR at the SNE. However, $\overline{\gamma}_2 < \gamma_2$ which implies that the microcell UE experiences a 3.5 dB SIR drop due to activation of the NCR. Although $\overline{\gamma}_1 > \gamma_1$, we still have a 10 dB gap to τ_1 which implies that the NCR is not very efficient (due to interference). As a conclusion to this case, we may say that without the RIS/NCR, the subnetwork and the microcell can indeed co-exist, as $\gamma_1 \approx \gamma_2 \approx 11$dB, but the subnetwork cannot benefit from a RIS, and can only mildly so from an NCR – but this comes at the expense of a major drop in performance for the microcell UE.

We next proceed with an investigation on the role played by the assumed location of the microcell UE. Wherefore we assume two possible regions where it may be located, see Figure 7. It may be understood that the average values for γ_1, $\overline{\gamma}_1$, and τ_1 are unaffected by the location of the microcell UE (since there is only a single antenna at 6G BSs), wherefore those values are copied from the above table. The results for the two locations, (A) and (B), are summarized in Table 10. We may see, that with an active RIS, the microcell UE is still degraded, but slightly less so.

Altogether, we may conclude that co-existence between a RIS-equipped subnetwork and a microcell is challenging when both systems operate at the same frequency. This is a consequence of the RIS/NCR, as they can co-exist without the presence of the RIS/NCR.

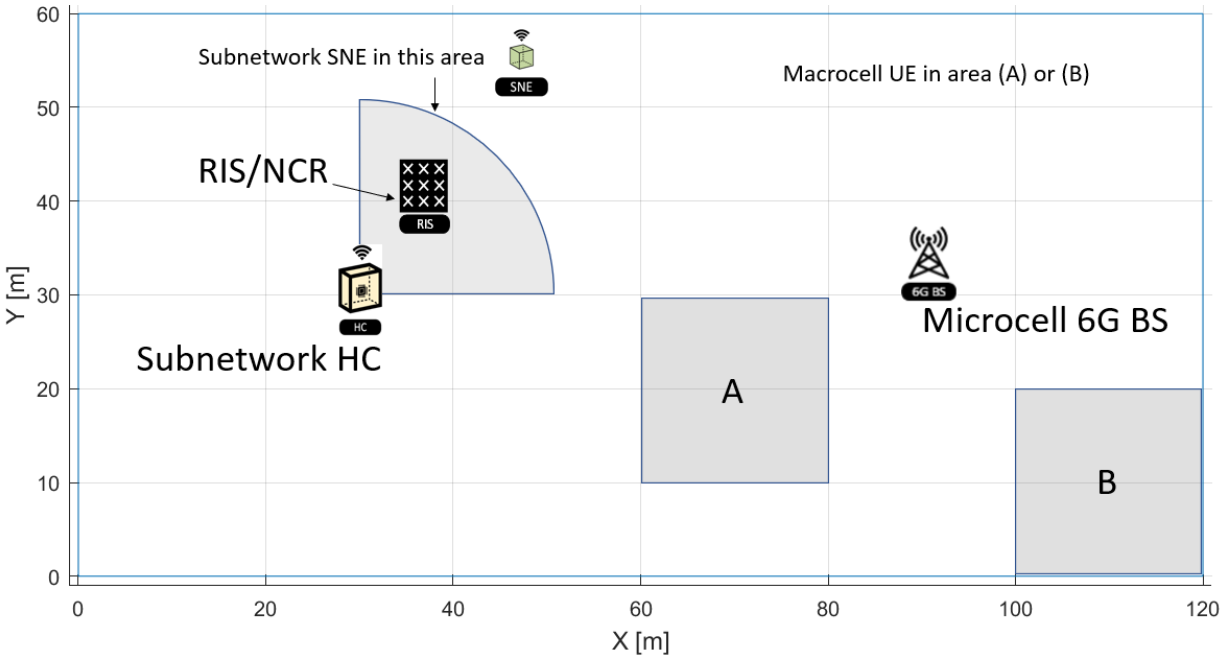

FIGURE 7 THE MICROCELL LC IS EITHER IN THE REGION A OR B.

TABLE 10 AVERAGE SIRS CORRESPONDING TO FIGURE 7

SIRs [dB]	γ_1	γ_2	$\overline{\gamma}_1$	$\overline{\gamma}_2$	τ_1
RIS	10.7	A:15.3. B:19.8	A and B: 8.6	A: 10.6. B: 14.2	22
NCR	10.7	A:15.3. B:19.8	A and B: 12.2	A: 8.3. B: 12.2	22

3.1.3.2. DIFFERENT FREQUENCY BANDS FOR SUBNETWORK THE MICROCELL

For this case the subnetwork and the microcell do not interfere each other, so one may ask why a RIS would matter for interference properties? The reason is that the when the RIS of the subnetwork is reconfigured, it is done so abruptly. This may abruptly change the propagation channels for the microcell, which implies that the channel cannot be tracked by reference symbols (e.g., Demodulation Reference Signal (DMRS)).

Assume that the RIS/NCR is inactive, i.e., its gain is set to null. The channel between the microcell 6G BS and its associated UE is

$$y_n = h_n x_n + w_n I = \log\left(1 + \frac{|\hat{h}|^2}{N_0}\right) + \frac{2}{N_0} Re(\hat{h}^* h) - \frac{|\hat{h}|^2}{N_0}\left[\frac{|h|^2 + N_0}{|\hat{h}|^2 + N_0} + 1\right]$$

where h_n denotes the channel between the 6G BS and the UE, x_n the symbol transmitted at subcarrier n, and w_n is complex Gaussian noise with variance N_0.

When the RIS/NCR is active, the received signal at the UE reads

$$\overline{y}_n = (h_n + s_n T t_n) x_n + w_n$$

where T is of the same form as before.

Assume now two cases: (1) The UE has estimated the channel during a period in which the RIS/NCR is inactive, i.e., the UE knows the value h_n, and the RIS/NCR becomes active. (2) The UE has estimated the channel during a period when the RIS/NCR is active, i.e., it knows the value $h_n + s_n T t_n$, and the RIS/NCR switches to an inactive mode. In both cases, we are in the domain of mismatched receivers. The rate that can be supported for a receiver that decodes on the basis of an estimate $\hat{h}$ but where the true channel is h reads (in nats/channel use)

$$I_{mism} = \log\left(1 + \frac{|\hat{h}|^2}{N_0}\right) + \frac{2}{N_0} Re\{\hat{h}^* h\} - \frac{|\hat{h}|^2}{N_0}\left[\frac{|h|^2 + N_0}{|\hat{h}|^2 + N_0} + 1\right]$$

For case (1), we set $\hat{h} = h_n$, $h = h_n + s_n T t_n$ and for case (2) $\hat{h} = h_n + s_n T t_n$, $h = h_n$. Based on experiments beyond what will be presented herein, the results for cases (1) and (2) are very similar, wherefore we only present results for (1). Our results are shown in Figure 8, where N_{ref} is a reference value which is irrelevant, and the scenario is the same as that considered in Figure 6. The blue curve is the achievable rate for the UE without any RIS/NCR, i.e., it is given by

$$I = \mathbb{E}\left[\log\left(1 + \frac{|h_n|^2}{N_0}\right)\right]$$

where the average is both over the subcarrier index and the location of the UE. The red and black curves are the rates of UE with a RIS and NCR present, respectively under assumption that UE has estimated the channel with the RIS/NCR present. That is, they are computed as

$$I = \mathbb{E}\left[\log\left(1 + \frac{|h_n + s_n T t_n|^2}{N_0}\right)\right]$$

where the expectation is now taken also over the location of the SNE – as it determines the RIS/NCR configuration. Finally, the red and black curves with markers, are the rates of the UE when the RIS/NCR is activated, but where the UE has formed its channel estimate when the RIS/NCR was not active, i.e., they equal I_{mism}.

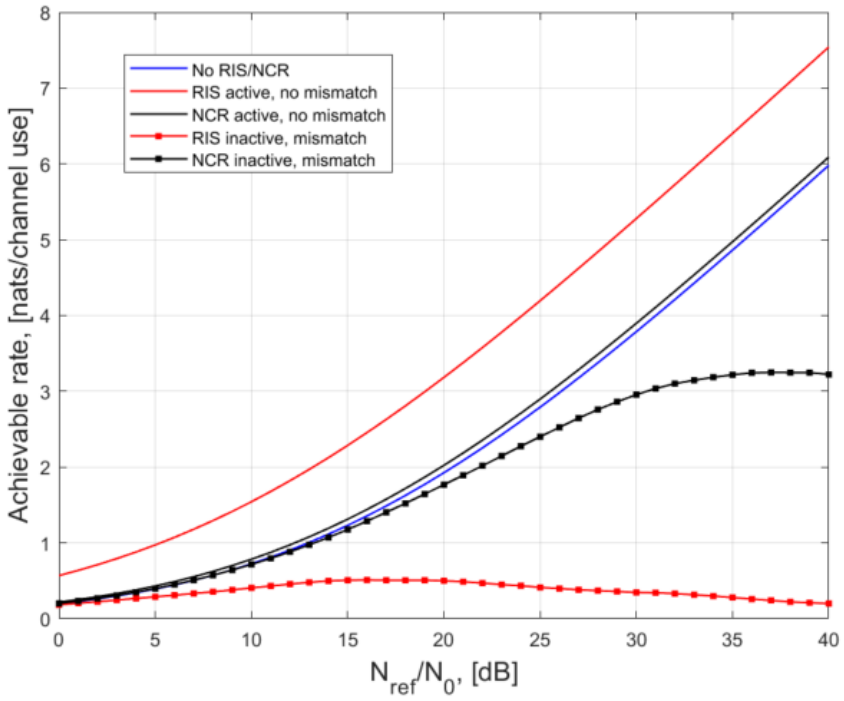

FIGURE 8 ACHIEVABLE RATES. SEE MAIN BODY OF TEXT FOR DESCRIPTION.

Interestingly, and importantly, we observe that a RIS of the subnetwork has significantly higher impact on the microcell than an NCR. In fact, a reconfiguration of a RIS in the subnetwork essentially destroys the communication of the microcell –despite the fact that they operate at different frequencies. On the other hand, a reconfiguration of an NCR in the subnetwork has no impact for microcell communications below 3 nats/channel use. The reason for this behaviour may be clearly seen in that the black curve is close to the blue: the NCR interferes with the microcell to a much smaller extent than a RIS.

We may conclude that for RIS/NCR assisted subnetworks, an NCR has much smaller impact on neighbour cells than a RIS. However, also an NCR may degrade performance in the microcell, and it is therefore concluded that some form of protocol should be designed so that reconfigurations are less harmful. For example, the RIS/NCR may only be allowed to be reconfigured at certain given time instances, or at very slow rates. This would allow the microcell to track the channel via its DMRS. Another solution would be for the subnetwork to indicate to the microcell each time a reconfiguration occurs.

3.1.4 FUTURE ACTIVITIES

The work so far has identified interference issues with RIS and NCR deployments in subnetworks and has demonstrated that in some cases a subnetwork should ideally not reconfigure its RIS without indicating this to surrounding cells. However, we have made our demonstration based on fairly generic channel models. In future work, we plan to expand our investigations to use cases and scenarios more tailored to the 6G-SHINE use cases. If we find that the identified issues indeed pertain to a wide array of use cases, then our ambition is to embark on protocols for co-existence of RIS-empowered subnetworks with other cells.

3.2 INTERFERENCE ASPECTS OF SUBNETWORKS: COMPARISON BETWEEN SPATIALLY SELECTIVE AND SPATIALLY NON-SELECTIVE RISs

3.2.1 TARGET KPIS/KVIS AND USE CASES

The material to be presented are general and targets most use cases, but with a strong focus on the industrial ones in which subnetworks are deployed within an already existing cell. Main KPIs addressed are interference mitigation and communication support for a large number of nodes.

3.2.2 PROBLEM STATEMENT

In the recent past, massive research efforts have been devoted to RIS technology. However, simulations and experiments are commonly limited to link-level studies – system-level studies are scarce in publicly available literature. System- and link-level simulations differ in a variety of ways, but here we are concerned with interference aspects of RIS deployments. Interference issues are largely non-existent in link-level studies, while profound in system-level. Therefore, we argue that interference issues are underexplored for RIS-aided systems in general, and for RIS-aided subnetworks in particular.

Different RIS hardware architectures have different interference properties. Herein we consider several potential RIS architectures and compare them with respect to interference.

3.2.3 RESULTS ACHIEVED SO FAR

Figure 2 provides an illustration of a typical RIS implementation. Remembering what was introduced in section 2.2.1 and invoking notation and derivations ensuing said figure, shows that if a signal $s_{nm}(\Theta_{\text{inc}})$ impinges upon unit-cell (n,m) from a direction Θ_{inc}, i.e., $s_{nm}(\Theta_{\text{inc}})$ are the components of a so called steering vector, then the backscattered narrowband signal v_{nm} from this cell reads

$$v_{nm} = s_{nm}(\Theta_{\text{inc}})r_{nm}(\Theta_{\text{inc}},\Theta) = s_{nm}(\Theta_{\text{inc}})\sqrt{F(\Theta_{\text{inc}})F(\Theta)}G_{\text{c}}\Gamma_{nm}$$

The term $\sqrt{F(\Theta_{\text{inc}})F(\Theta)}G_{\text{c}}$ is the same for all cells, wherefore we ignore it for the rest of this section (in fact, we set $F(\Theta)G_{\text{c}} = 1, \forall\Theta$, i.e., omni-directional antennas). With that, we have $v_{nm} = s_{nm}(\Theta_{\text{inc}})\Gamma_{nm}$. In the direction Θ, the received signal, save for path loss, reads

$$y(\Theta_{\text{inc}},\Theta) = \sum_{n,m} s_{nm}(\Theta)s_{nm}(\Theta_{\text{inc}})\Gamma_{nm}.$$

A "RIS configuration" is a particular setting of Γ_{nm} that yields a large value of $y(\Theta_{\text{inc}},\Theta)$. Recall from section 2.2 that

$$\Gamma_{nm} = \frac{Z_{nm} - Z_0}{Z_{nm} + Z_0}.$$

When Z_{nm} is strictly imaginary-valued, we have $|\Gamma_{nm}| = 1$, and optimizing the RIS configuration amounts to finding an imaginary Z_{nm} such that $\Gamma_{nm} = s_{nm}^*(\Theta)s_{nm}^*(\Theta_{\text{inc}})$ (where it has been assumed that $s_{nm}(\cdot)$ are normalized to unit magnitude). Due to the bijective nature of the functional relationship between Γ_{nm} and Z_{nm}, this is always possible. For Z_{nm} with a resistive component (such as 2.5 Ohm mentioned in section 2.2), the optimization is more cumbersome, but still doable in closed form after some lengthy, but straightforward, manipulations.

Let us focus, with a slight loss of generality, exclusively on the case of strictly imaginary valued Z_{nm}. We then, for the configuration $\Gamma_{nm} = s_{nm}^*(\Theta)s_{nm}^*(\Theta_{\text{inc}})$, have that $|y(\Theta_{\text{inc}},\Theta)|^2 = (NM)^2$. One may now consider what

happens in case a signal impinges from another direction, Θ'_{inc}, but the RIS configuration remains $\Gamma_{nm} = s^*_{nm}(\Theta)s^*_{nm}(\Theta_{\text{inc}})$. It is easily verified, see [97], that there exists[1] a direction Θ' such that we have $|y(\Theta_{\text{inc}}', \Theta)|^2 = (NM)^2$. Put simply, this implies that a RIS reflects a signal impinging from *any* direction, not only the configured one.

In general, this may lead to increased interference in systems, but a perhaps more daunting problem is that a non-RIS aided transmitter serving a receiver, may serve said receiver via another cell's RIS without being aware of it. If so, then said TX-RX pair's propagation link will change abruptly whenever the RIS is reconfigured. Such abrupt channel change cannot be captured by normal reference symbols and will lead to outdated Channel State Information (CSI). This situation may be especially challenging for subnetworks as it may be foreseen that a subnetwork operates in close vicinity to another cell. If the RIS belongs to the subnetwork, then it is the neighbour cell that may experience problems, while if the RIS belongs to the neighbour cell, then the subnetwork may suffer. For general cellular systems, these effects have been studied in the very recent paper [98].

Our objective is twofold:

1. Find RIS architectures that are spatially selective, i.e., they *only* reflect signals from a configured direction.
2. Perform simulations to investigate whether spatially selective RISs offer meaningful gains for subnetworks co-existing with other cells.

3.2.3.1 SPATIALLY SELECTIVE RIS

A spatially selective RIS can be achieved in various ways. In fact, in 3GPP a RIS-like device is a part of Rel-18 and is termed NCR. An NCR is spatially selective by design and has an architecture as depicted in Figure 9.

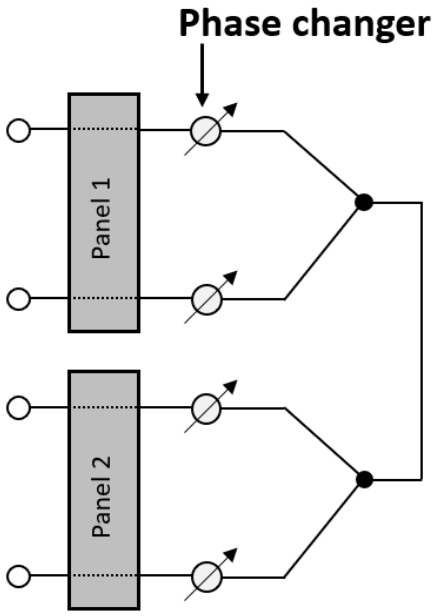

FIGURE 9 ARCHITECTURE OF NCR (WITHOUT FILTERS AND AMPLIFIER)

An NCR has two antenna arrays (a.k.a. panels) [104]. The received signals at, say, panel 1 are first phase shifted and then added up. The resulting signal is then split (lower black dot) into multiple signals. Each one is phase rotated and then transmitted from the antennas at panel 2. In an NCR, the idea is that panel 1 configures its phase shifters so that it beamforms towards, say, an HC while panel 2 beamforms towards the SNE. An NCR as defined by 3GPP is equipped with bandpass filters and a bi-directional amplifier; these two components are located between the two black dots. The bi-directional amplifier is HC-controlled and is configured based on the uplink

[1] Some exceptions exist, see [97].

(UL)/down link (DL) scheme of the cell. However, an amplifier is not strictly necessary and the architecture in Figure 2 is reciprocal by nature and constitutes an alternative to a conventional RIS (shown in Figure 2). The NCR has both pros and cons compared to a traditional RIS:

- For a a given number of antennas, only half of them are involved in reception and the other half in transmission. This gives a 3dB loss at both panels, so that a 6dB overall loss results in comparison with a traditional RIS.
- While a traditional RIS reflects a signal impinging from any direction, an NCR only reflects signals from configured directions, i.e., it is spatially selective. To understrand this, it suffices to note that the transfer matrix linking the antennas at panel 1 and panel 2 is a rank 1 matrix.

We also remark that the NCR in Figure 9 is fully reciprocal. That is, if panel 1 beamforms towards the 6G BS and panel 2 towards the LC, then the NCR works both for UL and DL traffic (This is also true for traditional RISs, but not for some of the RIS architectures to be presented shortly).

While NCR architectures have a well established position in contemporary literature, our next architectures are novel over the state-of-the-RIS-art. Our proposed architectures are depicted in Figure 10. The left architecture is more general than the right, but also more complicated. Let us first explain the operations of the left architecture. A signal arriving at an element, say, the top right one In the figure, is first phase rotated, and then enters a, possibly reconfigurable, permutor. For the permuation shown in the figure, said signal would leave the RIS from the rightmost element at the third “row” of the RIS. Note, however, that a signal entering the RIS at said rightmost element of row 3, would not leave the RIS from the top right element as the circulators break the reciprocity. This implies that the permuation is not symmetric, and this will have important consequences later.

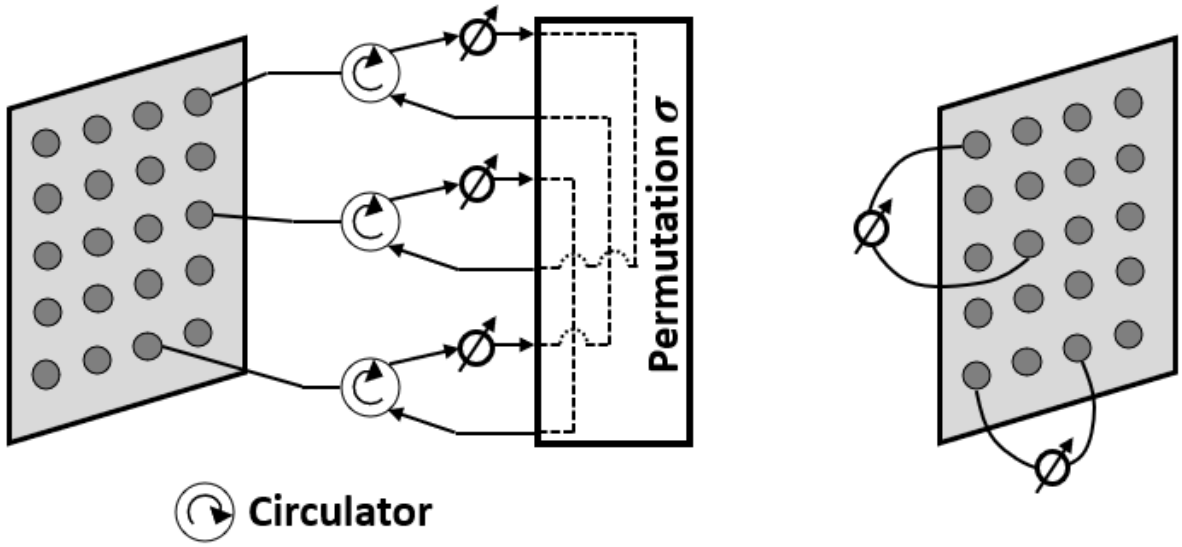

FIGURE 10 PROPOSED ARCHITECTURES FOR SPATIALLY SELECTIVE RISS

Circulators are somewhat bulky components, and it would be prefereble if they could be dispensed with. To that end, we have the right architacture, which is circulator free. In this architecture, an element arriving at an element (m, n) is phase rotated and then leaves the RIS from an element (m', n'). Meanwhile, a signal arriving at element (m', n') leaves the RIS from element (m, n) and undergoes the very same phase shift. Thus, the permutation is symmetric, circulator free, but only has one phase shifter per 2 antenna elements.

Let $\boldsymbol{s}(\Theta_{\text{inc}})$ denote an $NM \times 1$ column vector comprising all the elements $s_{nm}(\Theta_{\text{inc}})$ according to the reader's favorite order of vectorization. Said vector represents the steering vector of the impinging signal. We may define $\boldsymbol{s}(\Theta)$ in a verbatim manner. For the left architecture, the received signal at the receiver reads

$$y(\Theta_{\text{inc}}, \Theta) = \boldsymbol{s}^{\text{T}}(\Theta)\boldsymbol{P}D(\boldsymbol{\Gamma})\boldsymbol{s}(\Theta_{\text{inc}}),$$

where $\boldsymbol{P}$ is an $NM \times NM$ permutation matrix, $D(\cdot)$ denotes a diagonal matrix with its argument along the main diagonal, and $\boldsymbol{\Gamma}$ is a vector comprising the variables Γ_{nm} (in the same order as that for $\boldsymbol{s}(\Theta_{\text{inc}})$). A well-known fact of permutation matrices is that, unless $\boldsymbol{P}^{\text{T}} = \boldsymbol{P}$, we have in general that $\boldsymbol{x}^{\text{T}}\boldsymbol{P}\boldsymbol{y} \neq \boldsymbol{y}^{\text{T}}\boldsymbol{P}\boldsymbol{x}$. The implication of this is that

$$y(\Theta, \Theta_{\text{inc}}) = \boldsymbol{s}^{\text{T}}(\Theta_{\text{inc}})\boldsymbol{P}D(\boldsymbol{\Gamma})\boldsymbol{s}(\Theta) \neq y(\Theta_{\text{inc}}, \Theta),$$

i.e., the RIS is no longer reciprocal. Thus, the phase shift configuration must be different in UL and DL. Before we offer a solution to this problem, we mention that the RIS configuration $\boldsymbol{\Gamma}$ is trivial to find, namely:

$$\boldsymbol{\Gamma} = \boldsymbol{s}^{*}(\Theta_{\text{inc}}) \circ \boldsymbol{P}^{\text{T}}\boldsymbol{s}^{*}(\Theta)$$

which produces $|y(\Theta_{\text{inc}}, \Theta)|^2 = (NM)^2$, i.e., the permuted RIS offers equally high gain as a traditional, unpermuted, RIS. In the reverse direction, we must configure the phase shifts as $\boldsymbol{\Gamma}^{*}$, and by doing so, we obtain $|y(\Theta, \Theta_{\text{inc}})|^2 = (NM)^2$. A natural question is whether we may find a RIS configuration $\boldsymbol{\Gamma}$ for which it holds that $|y(\Theta_{\text{inc}}, \Theta)|^2 = |y(\Theta, \Theta_{\text{inc}})|^2 = A$ and where A is as close as possible to $(NM)^2$. This will be answered in Theorem 2.

If we consider the right architecture of Figure 10, we have the same model $y(\Theta_{\text{inc}}, \Theta) = \boldsymbol{s}^{\text{T}}(\Theta)\boldsymbol{P}D(\boldsymbol{\Gamma})\boldsymbol{s}(\Theta_{\text{inc}})$, but where $\boldsymbol{P}^{\text{T}} = \boldsymbol{P}$, and if $P_{\ell,\ell'} = P_{\ell',\ell} = 1$, then $\Gamma_{\ell} = \Gamma_{\ell'}$. The symmetry of $\boldsymbol{P}$ implies that for any $\boldsymbol{\Gamma}$ it holds that $y(\Theta_{\text{inc}}, \Theta) = y(\Theta, \Theta_{\text{inc}})$, i.e., the RIS is reciprocal. However, to determine the RIS configuration is now not entirely obvious as there is a single-phase shifter for every pair of antennas. We summarize our findings in Theorem 1.

Theorem 1. For the RIS architecture in the right part of Figure 10, assume $P_{\ell,\ell'} = P_{\ell',\ell} = 1$ and define

$$c_{\ell,\ell'} = s_{\ell}(\Theta_{\text{inc}})s_{\ell'}(\Theta) \qquad c_{\ell',\ell} = s_{\ell'}(\Theta_{\text{inc}})s_{\ell}(\Theta).$$

For a random permutation matrix $\boldsymbol{P}$ drawn uniformly over the set of permutation matrices, and for all pairs $(\Theta_{\text{inc}}, \Theta)$ except for those in a set of measure 0, the RIS configuration

$$\Gamma_{\ell} = \Gamma_{\ell'} = \frac{c_{\ell,\ell'}^{*} + c_{\ell',\ell}^{*}}{\left|c_{\ell,\ell'}^{*} + c_{\ell',\ell}^{*}\right|}$$

achieves

$$\lim_{N,M\to\infty} \frac{|y(\Theta_{\text{inc}}, \Theta)|^2}{(NM)^2} = \lim_{N,M\to\infty} \frac{|y(\Theta, \Theta_{\text{inc}})|^2}{(NM)^2} = \frac{4}{\pi^2} \approx 0.4053 \quad (-3.92\text{dB}).$$

Proof. See [97].

To achieve a reciprocal version of the left architecture of Figure 10, we have

Theorem 2. For the RIS architecture in the left part of Figure 4.1.1, assume $P_{\ell',\ell} = 1$ and define

$$c_{\ell} = s_{\ell}(\Theta_{\text{inc}})s_{\ell'}(\Theta) \qquad d_{\ell} = s_{\ell}(\Theta)s_{\ell'}(\Theta_{\text{inc}}).$$

For a random permutation matrix $\boldsymbol{P}$ drawn uniformly over the set of permutation matrices, and for all pairs $(\Theta_{\text{inc}}, \Theta)$ except for those in a set of measure 0, the RIS configuration

$$\Gamma_{\ell} = \frac{c_{\ell}^{*} + d_{\ell}^{*}}{\left|c_{\ell}^{*} + d_{\ell}^{*}\right|}$$

achieves

$$\lim_{N,M\to\infty} \frac{|y(\Theta_{\text{inc}},\Theta)|^2}{(NM)^2} = \lim_{N,M\to\infty} \frac{|y(\Theta,\Theta_{\text{inc}})|^2}{(NM)^2} = \frac{4}{\pi^2} \approx 0.4053 \quad (-3.92\text{dB}).$$

Proof. See [97].

Theorems 1-2 states that for random directions, and as the RIS grows large, both architectures of Figure 10 are equally well performing in terms of reflection gain in the configured directions, under the assumption that a reciprocal RIS is desired. The price to pay is about 4dB, and this "price to pay" refers to

- Making the left architecture of Figure 10 reciprocal.
- Using 50% less phase shifters in the right figure compared with the left one.

So far, we have not at all discussed spatial selectivity – the rationale of introducing the architectures in Figure 10. We do this next, in Theorem 3.

Theorem 3. For the RIS architecture in the left part of Figure 10 and with $\max(N,M) \geq 4$, there exists a permutation matrix $\boldsymbol{P}$ such that, for the configuration $\boldsymbol{\Gamma}$ achieving $|y(\Theta_{\text{inc}},\Theta)|^2 = (NM)^2$, there exists no other directions $(\Theta_1,\Theta_2) \neq (\Theta_{\text{inc}},\Theta)$ such that $|y(\Theta_1,\Theta_2)|^2 = (NM)^2$, except if $(\Theta_{\text{inc}},\Theta)$ belongs to a set of measure 0.

Proof. See [97].

A discussion of Theorem 3 is in place. First of all, Theorem 3 only guarantees existence of a permutation for which the RIS is spatially selective – it does not reveal how difficult it is to find such $\boldsymbol{P}$. However, in practice this is extremely easy: any randomly chosen $\boldsymbol{P}$ will do. Moreover, the permutation $\boldsymbol{P}$ may be separable in its rows and columns (i.e., an element (n,m) is permuted to an element $(\sigma_1(n),\sigma_2(m))$). Secondly, the Theorem does not quantify what the attenuation in all other directions may be. To further sharpen Theorem 3 constitutes an excellent research task for the young and ambitious researcher, but is beyond the scope of the 6G-SHINE project. Finally, Theorem 3 does not provide any information about the right architecture of Figure 10, or for a reciprocal version of the left one. However, natural extensions of Theorem 3 are easily verified, by means of numerical simulations, to be valid: Select a reciprocal RIS structure, either the left one or the right one, then $|y(\Theta_1,\Theta_2)|^2 = 4(NM/\pi)^2$ only happens for $(\Theta_1,\Theta_2) = (\Theta_{\text{inc}},\Theta)$ and $(\Theta_1,\Theta_2) = (\Theta,\Theta_{\text{inc}})$, save for $(\Theta_{\text{inc}},\Theta)$ belonging to a set of measure 0.

To quantify the degree of spatial selectivity we provide some simulations next for $N = M$. It is shown in [97] that the configured directions $(\Theta,\Theta_{\text{inc}})$ have no relevance on the attenuation of other directions and are therefore irrelevant. The reflection pattern of the RIS is fully characterized by $|y(\Theta_1,\Theta_2)|^2$ and we know that $|y(\Theta_1,\Theta_2)|^2 \approx N^4$ for $(\Theta_1,\Theta_2) \approx (\Theta,\Theta_{\text{inc}})$ and $|y(\Theta_1,\Theta_2)|^2 \ll N^4$ for (Θ_1,Θ_2) far from $(\Theta,\Theta_{\text{inc}})$. Loosely speaking, we may define the "main lobe" $\mathfrak{B}$ as all (Θ_1,Θ_2) for which $|y(\Theta_1,\Theta_2)|^2 \approx N^4$and we may then define the volume of this main lobe. More precisely, we define

$$\beta = \min_{\Theta_1,\Theta_2} \frac{|y(\Theta_1,\Theta_2)|^2}{N^4} \text{subject to } \|(k_1,k_2)-(k,k_{inc})\|^2 \leq \delta^2$$

where k-variables are directional cosines associated with the Θ-variables. The relationship between δ and β means the following: For all directional pairs (Θ_1,Θ_2) that are no more than δ away from the configured pair $(\Theta,\Theta_{\text{inc}})$, the beamforming gain is at least β. For example, if we set $\beta = 0.5$, then δ gives the radius of a 4-ball in which all directions are at most 3dB attenuated; the radius being given in terms of a directional cosine coordinate system.

We may then define the degree of spatial selectivity as

$$\tau = \max_{\Theta_1,\Theta_2} \frac{|y(\Theta_1,\Theta_2)|^2}{N^4} \text{subject to } \|(k_1,k_2)-(k,k_{inc})\|^2 > \delta^2$$

and we remark that a smaller τ means better spatial selectivity; this definition implies that for directions farther away from the configured pair than some δ, τ is the maximum beamforming gain.

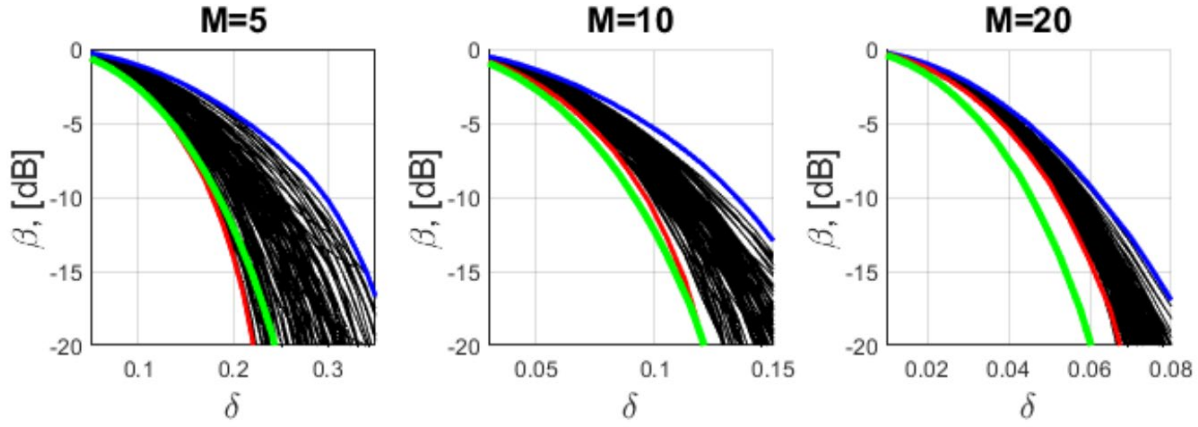

FIGURE 11 RESULTS FOR Δ AND B FOR 100 RANDOMLY SELECTED PERMUTATIONS (BLACK).

In Figure 11 we plot β against δ for 100 randomly selected permutations; we consider three different values of $M = N$, namely, 5, 10 and 20. The blue and the red curves highlight the top and bottom curves, respectively. The green curves are the ensuing results for the identity permutation, i.e., a traditional RIS. We can draw the following conclusions:

- A system designer has freedom in the design of the main lobe: By carefully selecting the permutation, one may choose a permutation with a ”widest” (top, blue curve) and ”narrowest” (bottom, red curve) main lobe.
- As *M* grows, there is less and less difference among permutations, and it appears that any randomly selected permutation suffices. This is most natural as average behaviours across the RIS are dominant.
- In general, the shape of the main lobe is not drastically changed compared with that of the identity permutation, but it appears to widen slightly.

The results for τ are shown as empirical Cumulative Distribution Functions (CDFs) in Figure 12 generated from the same set of 100 randomly generated permutations as in Figure 11. We remark that the identity permutation, corresponding to the green curves in Figure 11, leads to $\tau = 1$ as such RIS is not spatially selective. In generating the CDFs in Figure 12 we have chosen $\delta \in \{0.3, 0.15, 0.08\}$, for $M \in \{5,10,20\}$; these values for δ can be understood from Figure 11.

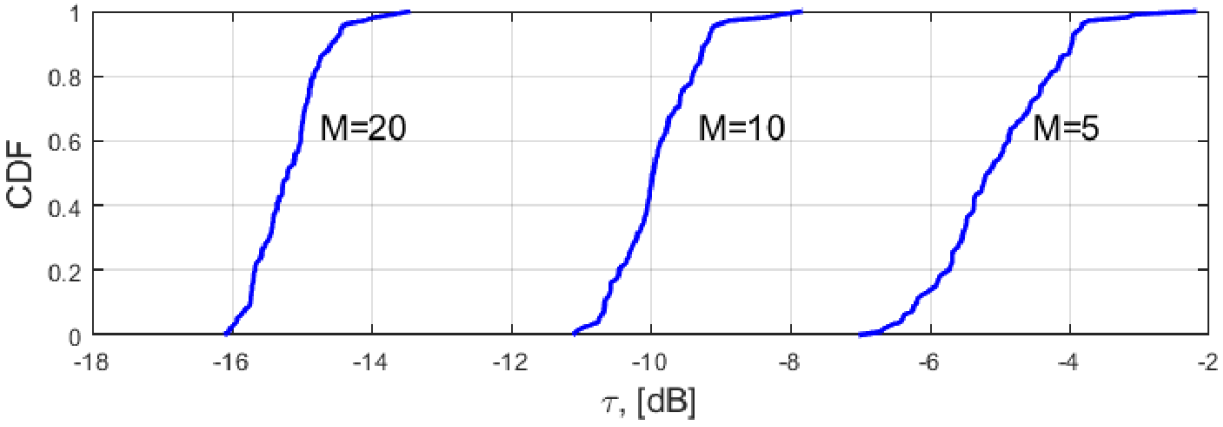

FIGURE 12 EMPIRICAL CDFS OF T FOR 100 RANDOM PERMUTATIONS.

3.2.4 FUTURE ACTIVITIES

In view of the system aspects presented in section 3.1, a spatially non-selective RIS may be a favourable path forward to avoid interference. Our plan is to conduct system-level simulations to determine to what extent non-diagonal RISs may improve the interference situation discussed in section. 3.1.

4 RIS-AWARE MAC PROTOCOLS FOR SUBNETWORKS

RIS-aware MAC protocols can be modelled using basic insights without focusing on specific protocol design, by considering two fundamental transmission modes: multiplexing and diversity [78]. In the case of multiplexing, the propagation conditions are learned, and adaptation of the user's transmission rate is done, whereas if RIS is included, then conditions can be estimated, and specific channel can be created to facilitate the user rate adaptation. In the case of diversity, the user rate is fixed, and the channel may or may not support the rate, whereas if RIS is included, the rate can be fixed and supported by some RIS configuration. These basic insights are used as a starting point to design a specific RIS-aware MAC protocol for subnetworks. It should be noted that conventional MAC protocols may underperform when enabling medium access to multiple users since these do not harness the benefits of RIS which may lead to improved user performance.

This contribution is comprised of three subsections: a subsection on brief overview of the state-of-the-art for RIS-aware MAC protocols, a subsection on preliminary design guidelines of the specific RIS-aware MAC protocol for subnetworks, and a subsection on considerations for the control channel and its involvement within the design of RIS-aware MAC protocol.

4.1. A BRIEF OVERVIEW OF THE STATE-OF-THE-ART

The state-of-the-art overview is used to identify all parameters relevant for building RIS-aware (or RIS-aided) MAC protocol for subnetworks. Further, the impact of these parameters on the performance is investigated in order to develop intuition about how RIS MAC protocol would perform for the subnetworks use cases. In principle, designing RIS-aided MAC is the reservation of RIS (or RIS elements) for each user before the transmission. There are a few preliminary studies where researchers have proposed a framework about how to reserve RIS resources [79]. In [79], the proposal is to divide the access in two phases, i.e., negotiation phase and transmission phase, as depicted in Figure 13. It is basically a hybrid of carrier-sense multiple access (CSMA) and Time Division Multiple Access (TDMA); the negotiation phase uses CSMA to reserve RIS resources and the data transmission phase uses a TDMA approach. The negotiation phase is contention-based, where each user competes for the access using some random backoff mechanism and then negotiates with the central unit (i.e., 6G BS) to reserve the RIS resources, power resources, channel resources, and time resources. During the transmission phase, RIS may be controlled, and elements can be switched on/off for each user on granted resources during the negotiation phase. The control of the RIS from the RIS controller entity can be done via a control channel which is important, and frequently overlooked aspect when it comes to RIS deployment, and development of RIS-aware protocols. Hence, we have included some considerations around the control channel in subsection 4.3.

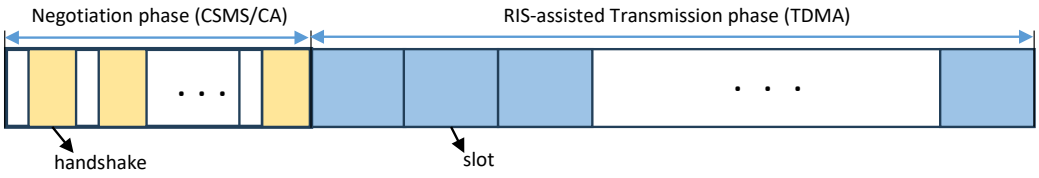

FIGURE 13 MAC FRAMEWORK FOR RIS ASSISTED TRANSMISSIONS.

AI-based techniques have been used to develop RIS-aware MAC protocols in centralized, decentralized and hybrid ways in [80]. In the centralized approach, the BS enables each RIS-controller to configure the propagation environment. The BS in this case estimates the concatenated BS-RIS-UE link, calculates the phase reconfiguration of the RIS, and allocates resources using deep learning. Similarly, in the decentralized RIS-aware MAC, each UE configures the propagation environment, and each UE negotiates with the RIS controller. In this case, computation and channel sensing are carried out at each UE and UE uses reinforcement learning (RL) to determine RIS configuration. In hybrid RIS-MAC, the frame is divided for scheduled users (centralized) and for competing users (decentralized) after pilot transmission and computing periods. A similar way MAC framework has been proposed

in [81], in which static users are using scheduled period and mobile users compete for RIS configuration for RIS-assisted transmission.

The work in [79] is a distributed technique where each user contests to access the channel and to reserve RIS resources. In [82], the authors propose a centralized and scheduling-based method for joint optimization of RIS group allocation and RIS reflection parameters in RIS-assisted downlink transmissions of Unmanned Aerial Vehicles (UAVs) with users especially when the LOS path is blocked or when there is poor channel condition. The problem is formulated as a multi-task learning problem that employs deep learning. The model takes UAV-user pairs, RIS size (number of elements etc) and channel conditions and outputs a transmission strategy of UAV-user pairs, which includes RIS element allocation and phase shift configuration. In [83], genetic algorithm is used to allocate a RIS and RIS elements to a particular user whereas the channel gain, transmit power and reflection coefficient is provided as the input. The elements of RIS are dynamically assigned to a user as opposed to [79, 82] where RIS elements are equally divided among users.

In RIS-assisted environments, for users with heterogenous demands, the multiplexing of Enhanced Mobile Broadband (eMBB), ultra-reliable and low latency communication (URLLC) and massive machine-type communication (mMTC) traffic creates additional challenges. Inspired by pre-emptive puncturing in 5G New Radio (NR), authors in [84] propose a solution to assist the URLLC traffic by temporarily muting the eMBB users and relying solely on eMBB Channel State Information (CSI). In [85], authors consider eMBB and URLLC services in existence with RIS and how RIS resources can be allocated for each service or jointly. This is done by jointly optimizing the power allocation at the BS and phase-shift matrix for RIS elements for eMBB. For URLLC, power and frequency allocation and RIS phase-shift matrix are optimized. The idea is to proactively allocate the phase-shift matrix before each time slot and for these three optimization-based solutions are provided, one for eMBB services, one for URLLC and one for joint eMBB and URLLC.

4.2 PRELIMINARY DESIGN OF RIS MAC PROTOCOL FOR SUBNETWORKS

Having surveyed the state-of-the-art works, we have identified parameters that have impact on performance and propose the following preliminary design of RIS MAC protocol for 6G-SHINE X-subnetworks, which is illustrated in Figure 14. The basic idea is to create groups of SNEs based on their subnetwork traffic characteristics, position, mobility (static or mobile) and their QoS requirements (URLLC, eMBB or mMTC etc). Further, the SNEs may also be grouped based on their position, and whether their transmissions occur when the SNEs are in the far-field or the near-field region. The far-field and the near-field classification may provide an important distinction when designing a RIS-aware access protocol for subnetworks. We divide the frame into pilot training phase or negotiation phase where each user is configured with RIS elements and time, and frequency resources as depicted in Figure 14. Top right hand side of Figure 14 also shows some conditions, checks and actions that are considered in this preliminary design such as: checking SNE category (SNEC) on per coherence block level (users may switch categories due to their mobility or changes in the traffic patterns), then configuring the RIS over Control Channel (CC) and adjusting time and frequency resources (similar to allocation of dynamic grants and configured grants in 5G).

Several use cases have been identified for RIS integration in X-subnetworks in the 6G-SHINE deliverable D2.2 [1]. The integration of RIS in each use case requires careful design of novel RIS-aware MAC protocols. For instance, RIS can dynamically adjust the wireless environment, and this will involve considering RIS or RIS elements in scheduling of resources among the SNEs. The SNEC may depend on 6G-SHINE use cases presented in the Deliverable D2.2 and each use case may be configured with pre-determined length of pilot's phase, dynamic and scheduled access phase. For a highly dynamic environment with mobile users, dynamic scheduling time may be increased and in the same way the environment with more static users, the scheduling period may be increased. Similarly, depending on the SNEs and use cases, the subcarrier allocation may also be adjustable.

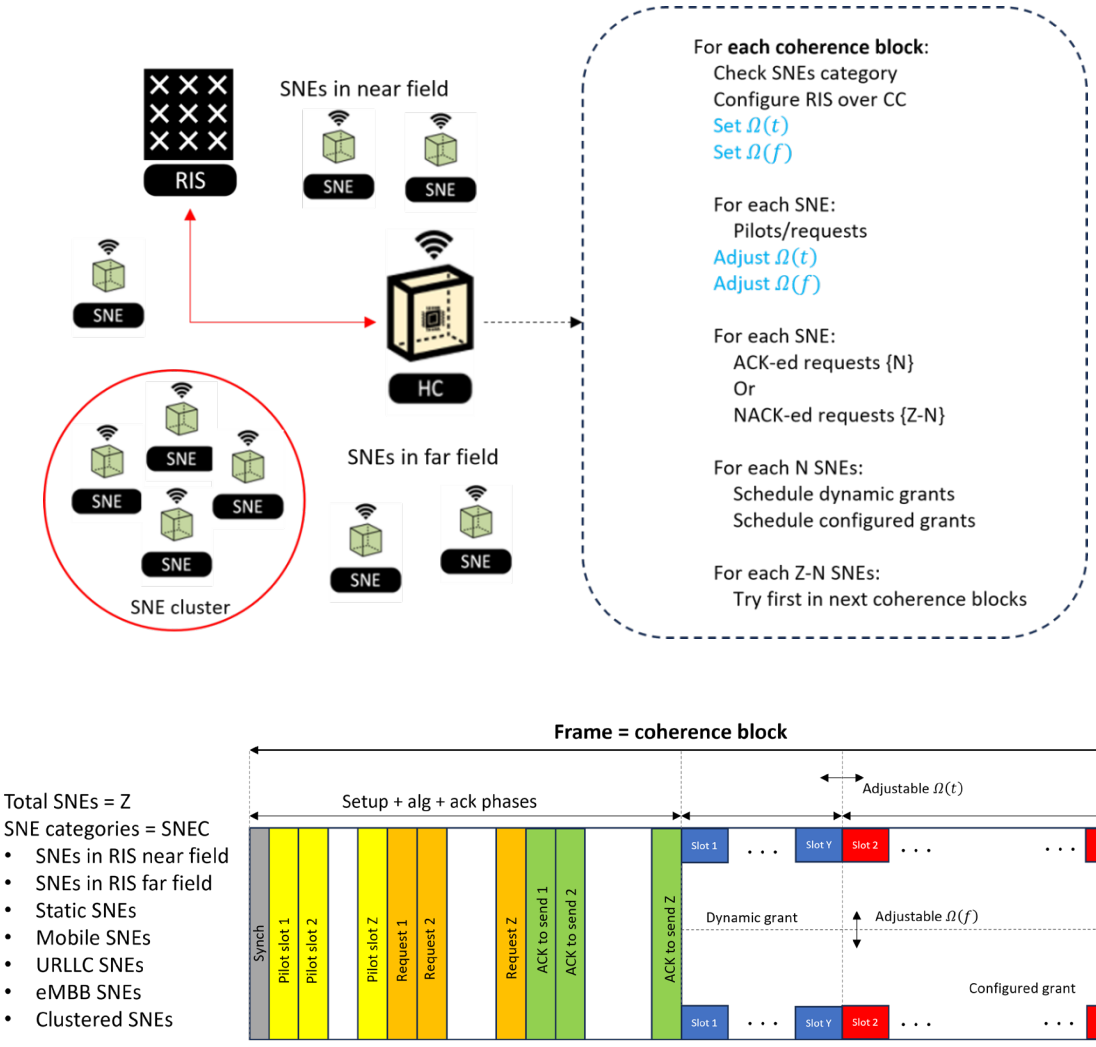

FIGURE 14 PROPOSED RIS-AWARE MAC FRAMEWORK FOR X-SUBNETWORKS

4.3 CONTROL CHANNEL CONSIDERATIONS FOR RIS MAC PROTOCOL DESIGN FOR SUBNETWORKS

The state-of-the-art on RIS MAC protocols shows that the efficiency of the protocol is increased when there is a possibility to dynamically adjust the RIS configuration of the RIS element (via control channel between the RIS and a RIS controller) compared to the case when the RIS element has a fixed configuration. In order to have the RIS element configured, it is necessary that the element is capable of receiving control information from the radio infrastructure (primarily from the RIS controller). There are two main principal types of channels for sending control information: out-of-band and in-band [86]. In the case of out-of-band control channel, the transmission of the control information does not use portion of the useful bandwidth in the subnetwork and may be implemented as a wireless channel that uses different spectrum compared to the subnetwork, or even as a wired link. In the case of in-band control channel, the transmission of the control information uses a portion of the useful bandwidth in the subnetwork which affects the overall capacity of the subnetwork. In the case of using out-of-band control channel, it is implied that the control information must be sent before the actual data transmission. However, in the case of using in-band-control channel, the control information may be sent before the actual data transmission and it may be sent simultaneously with the actual data transmission. These aspects have to be included in the RIS MAC protocol design and depend on the subnetwork use case. For example, industrial subnetworks that do not require large bandwidth for data transmissions may be more suitable for in-band control channel signalling, whereas use cases where XR traffic is exchanged may require out-of-band control channel signalling to configure the RIS elements.

5. PRELIMINARY RESULTS ON RIS DEPLOYMENT AND OPTIMIZATION STRATEGIES

The optimization of the configuration of the RISs deployed in a given scenario depends on a myriad of factors such as the geometric configuration (position of devices and RISs), the QoS requirements, multi-device interference, and the instantaneous propagation channel state. While in a single-device single-RIS MIMO scenario the optimal RIS configuration has been recently found analytically for far- and near-field free-space propagation conditions [106], when employing many devices (e.g., SNEs), realistic channel conditions, and multiple RISs, such an optimization might require unsustainable communication overhead (e.g., for the RIS control channel and CSI estimation), and computational complexity stemming from the large number of configuration parameters of a RIS. This might even be more severe when operating in the propagation near-field regime as typically happens when working at high frequencies with large antenna arrays or large RISs. In this context, in section 5.1 a practical approach to mitigate both communication overhead and computational complexity by reducing the dimension of the optimization problem in a near-field scenario is presented. In section 5.2, a rate weight adaptation strategy aiming at achieving a form of proportional fairness among SNEs, to improve the quality of service for nodes with poor signal propagation conditions from the HC, is illustrated along with some preliminary results.

5.1 NEAR-FIELD RIS ALLOCATION STRATEGIES FOR RIS-AIDED MIMO COMMUNICATIONS IN THE PRESENCE OF MULTIPLE USERS

5.1.1 TARGET KPIS/KVIS AND USE CASES

Aligned with the 17 United Nations Sustainability Development Goals (SDGs), the proposed strategy demonstrates relevance in the realm of industry, innovation, and infrastructure. More precisely, it tackles the challenges associated with communication within industrial environments featuring a high number of nodes. By doing so, it contributes to the development of a robust communication infrastructure and fosters a work environment that promotes productivity and well-being, optimizing communication performance and resource allocation.

5.1.2 PROBLEM STATEMENT

The exploration of enhancing communication performance through a RIS-assisted system has garnered significant attention within the wireless community in recent years. However, compared to most existing works in the literature, two primary constraints emerge. Broadly speaking, the planar structure of RIS, composed of numerous scattering elements (equivalently addressed as atoms or unit cells), necessitates optimization that relies on a central controller determining the phases for each RIS atom. Subsequently, this decision is communicated to a local controller, responsible for configuring the RISs accordingly. Regrettably, this method suffers from two major drawbacks: the burden of communication overhead and the computational complexity stemming from the substantial number of atoms requiring optimization. This limitation hinders the deployment of systems with a large number of RISs and SNEs, constraining potential use cases.

To address these issues, a practical approach involves mitigating both communication overhead and computational complexity by reducing the dimension of the optimization problem. This is achieved by employing a more streamlined set of potential RIS configurations, transforming the problem into an assignment problem. Essentially, this approach employs a management technique directly at the physical layer resources, facilitating simpler optimization procedures. In other words, we propose a strategy for allocating RISs in a multi-SNE MIMO scenario, aiming to maximize the weighted system throughput. Each RIS is subdivided into tiles, as opposed to considering individual atoms, and each tile is preconfigured with the capacity to serve each node. Consequently, this eliminates the challenge of finding the best configuration of each single atom. The schematic representation of this scenario is depicted in Figure 15.

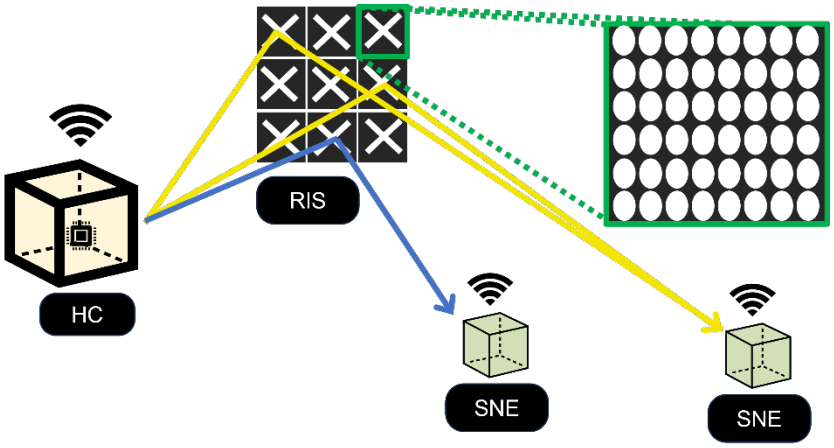

FIGURE 15 SCHEMATICAL REPRESENTATION OF THE PROPOSED APPROACH

Reframing the problem as an assignment problem yields a simplified approach, enabling optimization in scenarios with numerous nodes and multiple RISs. This underscores one of the key benefits of incorporating RISs in wireless communication—an appreciable enhancement in system fairness. Specifically, this improvement aims to elevate the quality of service for nodes experiencing suboptimal signal propagation conditions from the HC.

In the context of this study, we focus on a downlink communication scenario featuring a single HC and multiple SNEs, each benefiting from the assistance of multiple RISs. The intelligent surfaces are structured into non-overlapping tiles, each comprising a specific number of atoms. The information symbols, assumed to be zero-mean and independently and identically distributed (i.i.d.) random variables (RVs), are transmitted to the SNEs through a compound channel. This channel encompasses both the direct HC-to-SNE link and the concatenated HC-to-RIS-to-SNE channel.

Similar to the approach in [87], our consideration for the direct HC-SNE link involves a spatially non-stationary narrow-band clustered channel model. This model, commonly applied in millimeter-wave (mmWave) communications, incorporates near-field and far-field effects of electromagnetic propagation in the presence of large antenna arrays. The channel consists of a LOS component and a NLOS component, which includes numerous clustered paths, each corresponding to a macro-level scattering path. Specifically, we assume that the centre of each multipath cluster lies on an ellipse with foci coinciding with the antennas of the HC and SNE. For simplicity, we assume all centres are on the same ellipse. Each cluster consists of multiple paths, and each path is represented by a point randomly placed within a small maximum distance from the cluster centre. Consequently, all paths of a given cluster reach the receiver within a limited angular spread, aligning with typical mmWave channels. The path loss for the channel is modelled according to the channel model for indoor office (IO) and shopping mall (SM) NLOS scenarios at 28 GHz, as detailed in [88].

In the context of RIS-assisted communications, considerations vary for the indirect HC-RIS-SNE link. Near-field effects become significant when the RIS size is large and transmission distances are short [89]. In such cases, the plane wave approximation breaks down, and spherical waves must be considered. Consequently, the channel is non-stationary along the RIS, necessitating the consideration of transmission distances between the RIS unit cells and the antennas of the HC and SNEs, beyond angles of incidence and scattering. Generally, RISs are strategically deployed to maintain LOS with the HC and SNEs, providing more benefits when the HC and SNEs are in NLOS [90]. It is worth noting that, unlike the direct HC-SNE link, the NLOS component of the channel is absent for the HC-RIS and RIS-SNE channels, as it is associated with second- and higher-order reflections, typically negligible and thus ignored in this study.

The signals incident on the surfaces undergo reflection towards the SNEs based on the RIS's responses, specifically, the phase shift coefficients of the RISs assigned through reconfiguration. In our model, to streamline the design of these coefficients, typically derived for individual atoms, each tile, comprising multiple atoms, is associated with a single SNE through a linear combination of potential basis functions. Mathematically, this can be expressed as $\boldsymbol{b} = \sum_{m=1}^{N_u} \gamma_m \boldsymbol{b}^{(m)}$, where N_u is the total number of SNEs, and the sets $\{\boldsymbol{b}^{(m)}\}$ and $\{\gamma_m\}$ represent the possible basis

functions and the binary allocation variables respectively. The allocation is executed by setting the binary coefficients of the linear combination, such that the tile is assigned to SNE m if the m-th coefficient is 1 and 0 otherwise, with the constraint that each tile is assigned to only one SNE. Assuming each small tile is in the far-field region concerning the SNEs, the *m*-th basis function is designed as a function of the angle at which the tile perceives the corresponding *m*-th SNE. In other words, a tile assigned to the *m*-th SNE redirects the signal received from the HC toward that SNE.

At this stage of the study, certain assumptions about the RIS model impact the RIS response. For each surface, we assume that the mutual coupling among scattering elements can be neglected, meaning the RIS response $\boldsymbol{\phi}$ = diag(**b**) for every surface is a diagonal matrix. Additionally, we assume that the surface induces pure phase shifts—i.e., the amplitude of the reflection coefficients for each atom is one. This assumption is reasonable under the hypothesis that every RIS scattering element, or port, is matched with a purely reactive impedance and the RIS is lossless, with a perfectly ideal scattering matrix with 0 values, indicating total reflection of the impinging energy. [88].

In this initial study, the selected allocation strategy is heuristic, assigning the tile to the nearest SNE. This choice underscores the system's capability to effectively handle a large number of SNEs.

5.1.3 RESULTS ACHIEVED SO FAR

In our simulation scenario, we envision an indoor environment spanning a 30 × 30 m area. Within this space, a multiple-antenna HC is deployed, featuring 16 antennas arranged in two linear arrays, each comprising 8 antennas. The HC is strategically aligned in the (-y, z) plane and situated at the coordinates (30, 15, 2) within the environment. Consequently, the scenario includes multiple SNEs scattered randomly throughout the designated area, each receiving support from various RISs. This setup reflects a dynamic and diverse communication environment, allowing for the exploration and evaluation of communication strategies and optimizations in a real-world, indoor context.

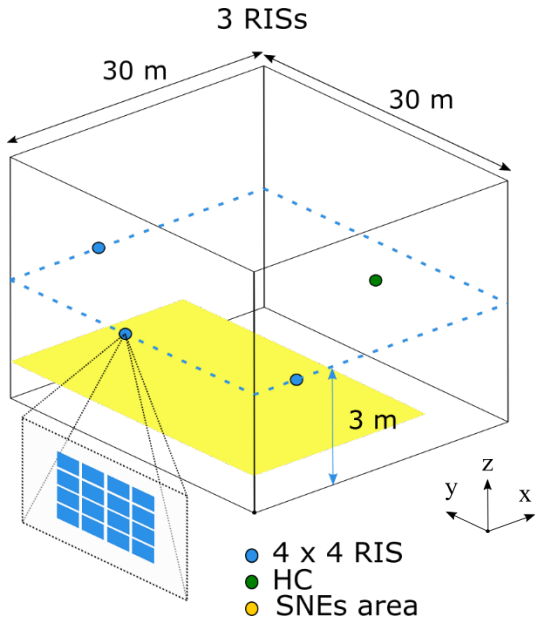

FIGURE 16 WORKING SCENARIO

As reported in Figure 16, for the simulations we use a configuration with 3 RISs divided in 4 x 4 tiles, for a total number of 48 tiles. Each tile comprises 200 scattering elements. Two RISs in position (10, 0, 3) and (5, 30, 3) are oriented along the (x, z) plane while one in (0, 15, 3) is along the (y, z) plane. All antennas and the RIS elements are spaced half wavelength apart. As for the SNEs we consider individual antennas SNEs.

TABLE 11 SIMULATION PARAMETERS

SYSTEM PARAMETER	VALUE
Working frequency	28 GHz
Noise power spectral density	174 dBm/Hz
Transmit power	20 dBm
Noise figure	8 dB
Antenna gains in transmission and reception	3 dBi
Bandwidth	30 kHz

The entailed simulation parameters are summarized in Table 11. The results are then given in terms of spectral efficiency (bits/s/Hz) for a single subcarrier and are obtained by Monte Carlo simulations. In this case we consider the system to be frequency non-selective, i.e., the RIS optimization would not change considering a large bandwidth. The direct HC-SNE link is modelled according to two different channel models, IO and SM (see [87]) with probability 70% and 30%, respectively. Note that both cases refer to an NLOS situation, but IO corresponds to stronger attenuation with distance, while SM represents a qualitatively better direct connection. Conversely, the HC-RIS and RIS-SNE connections are assumed to occur under LOS conditions, taking advantage of the greater RIS height.

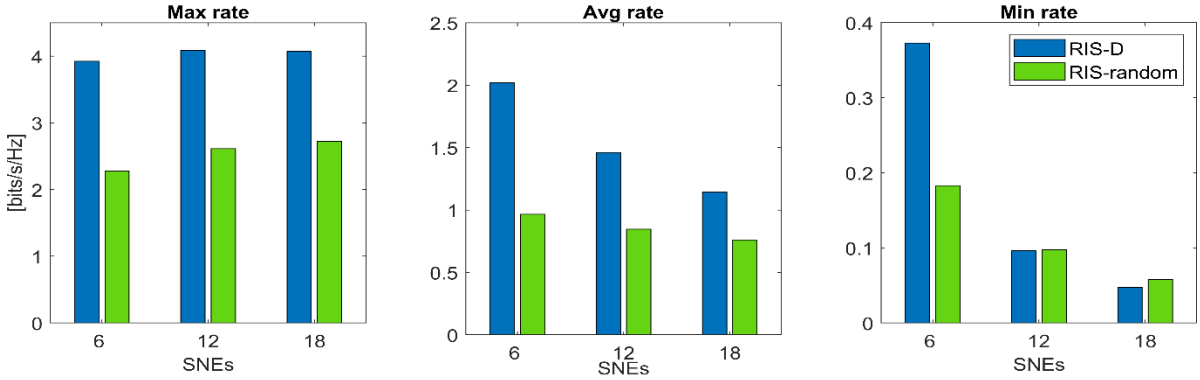

FIGURE 17 PERFORMANCE COMPARISON BETWEEN RIS-D AND RIS-RANDOM CONFIGURATIONS FOR 6, 12, 18 SNES.

In Figure 17 we present the outcomes for the proposed algorithm (RIS-D), where tile allocation follows a heuristic based on a minimum distance criterion, and for the case where the RISs are randomly configured (RIS-random). The results are delineated in terms of maximum, average, and minimum rates, computed as the average over all the simulations of the best, all, and the worst SNEs rates, respectively. Scenarios involving 6, 12, and 18 SNEs have been considered for the simulations. Notably, the system demonstrates robust support for a high number of SNEs, ensuring commendable performance with manageable complexity. More specifically, in relation to the chosen allocation criterion, due to the competition for finite resources, there is a slight performance degradation observed in the minimum rate as the number of SNEs increases, decreasing of almost 87 % when passing from 6 to 18 SNEs. However, the results remain satisfactory in terms of maximum and average rates: in the former case the maximum rate improvements is around 3.85 % for 18 SNEs, compared to the results for 6 SNEs only, while in case of the average rate there's a decrement of around 43 %. This indicates that, while there may be a marginal reduction in the minimum rate, the overall system performance remains robust, demonstrating the effectiveness of the proposed algorithm in supporting diverse communication scenarios with a substantial number of SNEs.

5.1.4 ADVANCEMENTS WITH RESPECT TO THE STATE OF THE ART

In the context of RIS-aided scenarios, we explore the feasibility of employing a physical layer resource management technique to streamline subsequent RIS optimization processes, especially in scenarios involving numerous RISs and SNEs. While existing literature has delved into physical resource management in RIS-supported systems, there is a notable gap in addressing communication overhead and computational complexity arising from the configuration of a large number of atoms on the surfaces.

Previous studies, such as [91-94] have tackled weighted sum rate maximization problems, system throughput maximization, and resource allocation in various RIS-aided scenarios. For example, in [91], a weighted sum rate maximization problem is formulated to jointly optimize the deployment location and reflection coefficients of one RIS as well as the power allocation to the HC in a multi-SNE scenario. To this end, three different access schemes are considered, namely non orthogonal multiple access (NOMA), frequency division multiple access (FDMA), and TDMA, and the solutions are obtained using monotonic optimization, Semidefinite Relaxation (SDR), and exploiting the time-selective nature of RIS. Alternate optimization (AO) and successive convex approximation techniques are used to provide low complexity suboptimal solutions, and a local region optimization method is applied to optimize the RIS deployment site. A similar study is conducted in [92], where the average sum rate optimization problem in a two-SNE scenario with the option of using NOMA, FDMA, or TDMA is investigated. The problem is formulated in terms of two matching schemes, dynamic phase matching and one-time phase matching, and the optimal resource allocations are determined using Lagrangian dual decomposition. The system throughput is also maximized in [93], where a RIS-supported NOMA system is considered. The problem is formulated as a joint optimization problem for channel allocation, decoding order of NOMA SNEs, power allocation, and RIS reflection coefficients, using a three-stage novel resource allocation algorithm that considers the different objectives separately. In [94], the authors study a RIS-enhanced Orthogonal Frequency Multiplexing (OFDM) system with frequency-selective channels. In this case the main objective is to maximize the achievable rate by jointly optimizing the power allocation and RIS coefficients and a suboptimal solution is obtained through AO.

As previously stated, in relation to the works presented in the literature, there has been a lack of considerations regarding the communication overhead and computational complexity, however, one approach to mitigate both issues is to introduce an RIS allocation problem that necessitates simpler and faster resolution techniques.

Following this line of research, the problem of assigning RIS to multiple SNEs in a NOMA scenario is explored in [95], where the SNE outside the field of view of the RISs are directly served by the assigned HC, while the remaining SNEs are served by the RISs. Conveniently divided into sub-areas, each RIS is dedicated to a different SNE, thus achieving a degree of fairness. Instead of the original non-convex and non-linear integer programming approach, the structure of the problem is exploited to find a suboptimal solution with marginal performance degradation. The solution meets certain fairness criteria, including the requirement for each SNE to be allocated a minimum number of RIS elements, an adaptable step size for the selected number of assigned elements, and the necessity to assign more elements to SNEs with weaker RIS-SNE channel gain. In [96], a RIS-supported dual connectivity (DC) architecture is proposed. The joint resource allocation of the RIS-supported DC is formulated as an optimization problem that yields the optimal SNE time fraction for scheduling. In this context, binary variables are used to indicate whether the SNE is associated with a RIS or not. The solution is obtained considering the Karush-Kuhn-Tucker (KKT) constraints applied to the decomposed original problem and using a heuristic approach.

Our approach takes inspiration from the existing works but further simplify the RIS optimization problem framing it as a heuristic allocation problem. Our chosen allocation strategy is symbolic at this stage, to emphasize that, in contrast to existing literature, our proposed approach can handle systems with a high number of RISs and nodes due to the reduced computational complexity we provide. This emphasis on computational efficiency addresses a crucial aspect often overlooked in prior works, making our approach more practical for real-world implementation in scenarios with numerous RISs and SNEs.

5.1.5 KPIs REACHED SO FAR AND ONGOING ACTIVITY

Simulation results give evidence to the potential of the proposed approach in handling system with high number of SNEs, as it may happen in industrial scenarios with many sensors and actuators. Building upon the introduced allocation strategy in this work, the primary objective for the current phase is to introduce an RIS optimization strategy, distinct from the heuristic approach. This optimization strategy is aimed at maximizing the system rate in a fair manner for the SNEs being served.

5.2 OPTIMAL RIS CONFIGURATION IN MULTIPLE USERS MIMO SCENARIOS

5.2.1 TARGET KPIS/KVIS AND USE CASES

The main focus of the work is focused on the industrial environment in which we aim at addressing the problem of providing a satisfying minimum experience data rate assured for the SNEs. Within the framework of the 17 United SDGs, the proposed strategy holds significant relevance in the field of industry, innovation, and infrastructure. The focus on fairness enforcement aligns with the overarching goal of creating inclusive and sustainable systems. In the context of industry, innovation, and infrastructure, where a myriad of nodes such as sensors and actuators are integral components, ensuring fairness becomes crucial.

5.2.2 PROBLEM STATEMENT

The possibility of developing a RIS-aided system for rate maximization has been widely investigated in recent years in the wireless community. However, as highlighted in section 5.1, most of the work presented in the literature often overlooks two significant limitations associated with introducing RISs into communication systems, i.e., the computational complexity deriving from the necessity of optimizing every single element of the planar structure and the communication overhead due to the necessity of transmit the optimized RIS configuration to a local controller that subsequently applies it to the surface.

In order to get rid of these two limitations we leveraged on the possibility of recasting the RIS optimization problem into an allocation problem (see section 5.1) in which the allocation is performed in order to maximize the weighted system throughput [99]. The simplification that results from formulating the problem as an assignment problem allows optimization in a scenario with many nodes and many RISs, highlighting that one of the advantages of introducing RISs in a wireless communication context is to significantly increase the fairness of the system, i.e., to improve the quality of service for nodes with poor signal propagation conditions from the HC. To this aim we further propose a rate weight adaptation strategy which aims at achieving a form of proportional fairness among SNEs.

We consider a downlink communication scenario with one HC and multiple SNEs aided by multiple RISs. Each RIS consists of non-overlapping tiles grouping a given number of atoms. Information symbols, assumed to be zero-mean and i.i.d. RVs, are conveyed to the SNEs by means of a compound channel that includes the direct NLOS HC-SNE link and the cascaded HC-RIS-SNE channel. The HC-RIS and RIS-SNE channels are assumed to be in LOS, and the expressions can be derived accordingly. The signals that impinge on the surfaces are reflected towards the SNEs according to the RISs' responses, i.e., the phase shift coefficients of the RISs, assigned through reconfiguration. In our model, to simplify the design of the coefficients, usually derived for every single atom, each tile, grouping many atoms, is associated with one SNE. This association is accomplished through a linear combination of potential basis functions, with binary coefficients determining whether the tile is allocated to the SNE or not. In this phase of the work, assumptions are made about the behaviour of RISs that allow for the derivation of simplified models, which can be effectively employed for system optimization purposes. We assume that, for each surface, the mutual coupling among scattering elements can be disregarded, resulting in the RIS response being a diagonal matrix. Additionally, we posit that the surface induces pure phase shifts, implying that the amplitude of the reflection coefficient for each atom is unitary. This assumption is justifiable under the hypothesis that each RIS scattering element, or RIS port, is characterised by a purely real internal impedance and is terminated on a purely reactive impedance [88].

System optimization is performed leveraging on two different variables, i.e., the allocation variables which impact the final RIS phase reflection coefficients, and the precoding matrices used at the transmitter side to direct the

informative signal intended for the SNE towards its direction. After expressing the system rate in terms of these variables the problem formulation is expressed in terms of a weighted maximization problem in which the system weighted rate is maximized with constraints about the binary allocation variables and the total maximum power at the transmitter side. At this initial step the weights are actually unitary while further studies are presented in the following to enforce system fairness.

Due to the nonconvex nature of the proposed problem, which makes it challenging to solve directly, we divide it into two subproblems—precoding optimization and tile allocation optimization. The overall problem is then solved through an AO approach between these two subproblems. This iterative process is schematically summarized in Figure 18.

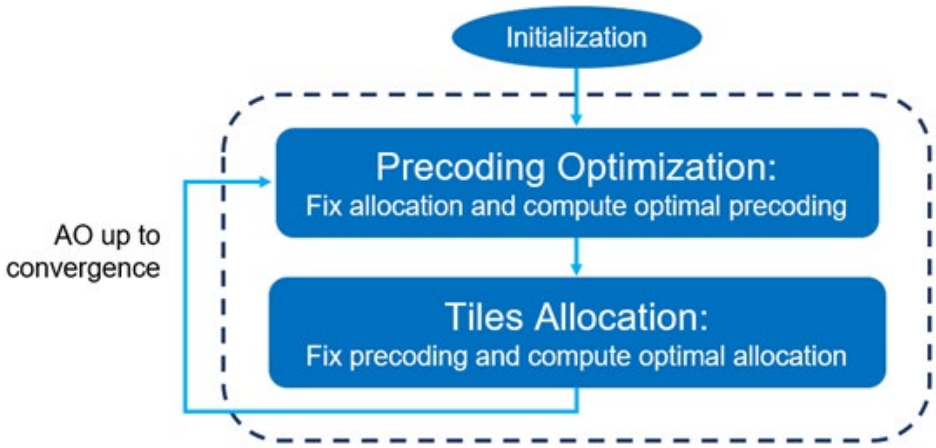

FIGURE 18 FLOW CHART OF THE PROPOSED ALGORITHM

For the precoding optimization the allocation variables are held fixed and the solution to the first subproblem can be achieved using the Weighted Minimum Mean Square Error (WMMSE) minimization approach. The WMMSE algorithm leverages the close relationship between the Signal-to-Interference-plus-Noise Ratio (SINR) and Mean Square Error (MSE), in order to find a locally optimal solution to the sum-rate problem [100]. To do that it is sufficient to introduce the MSE matrix and to apply some mathematical elaboration to convert the problem into an actual WMMSE minimization problem. The solution to the problem is found by means of AO combined with Block Coordinate Descent (BCD) algorithm. More details can be found in section III-B of [87].

Using the same approach as for precoding optimization but fixing the set of precoding matrices instead of the allocation variables, the tile allocation optimization problem can be formulated as a WMMSE problem as well. Also in this case, by means of mathematical elaborations we are in the position of recast the problem into the form of a non-homogeneous quadratic integer programming problem that, however, does not admit an algorithmic solution of acceptable complexity. One way to circumvent this problem is to relax the integer constraint for the allocation variable with a convex constraint, so that the problem turns out to be a quadratic (i.e., convex) programming problem with affordable complexity. The relaxed problem has a solution that is a lower bound for the original problem. Moreover, by projecting the relaxed solution on the feasible set of the original problem one can find a good integer solution. In other words, given the relaxed solution, the projection operator sets for every tile the allocation variable to 1 for the SNE that maximizes the entries of the relaxed solution corresponding to the tile and to 0 the entries of all other SNEs.

For the final step a weight adjustment procedure for the weighted rate maximization is presented. The weights of the proposed approach can be evaluated using an online iterative procedure with the goal of maximizing a long-term utility that enforces fairness, for instance. To do so we define a utility function which depends on the average rate achieved after every optimization procedure and we derive a utility maximization problem in terms of the precoding matrices and the allocation variables. Applying a Taylor series expansion with respect to the current time instant and considering the quantities that depends on it, the utility maximization problem can be rewritten

in the same form as the original weights rate maximization problem with the weights corresponding to the first order derivative of the utility function computed at the previous time instant.

5.2.3 RESULTS ACHIEVED SO FAR

For the simulation scenario we consider an indoor environment with an area of 30 x 30 m, in which a multiple antenna HC, consisting of 16 antennas arranged in two linear arrays of 8 antennas each, is aligned in the plane (-y, z) and located at the point (30,15,2) m. Hence, we have multiple SNEs with random positions in the considered area supported by multiple RISs. The scenario is illustrated in Figure 19.

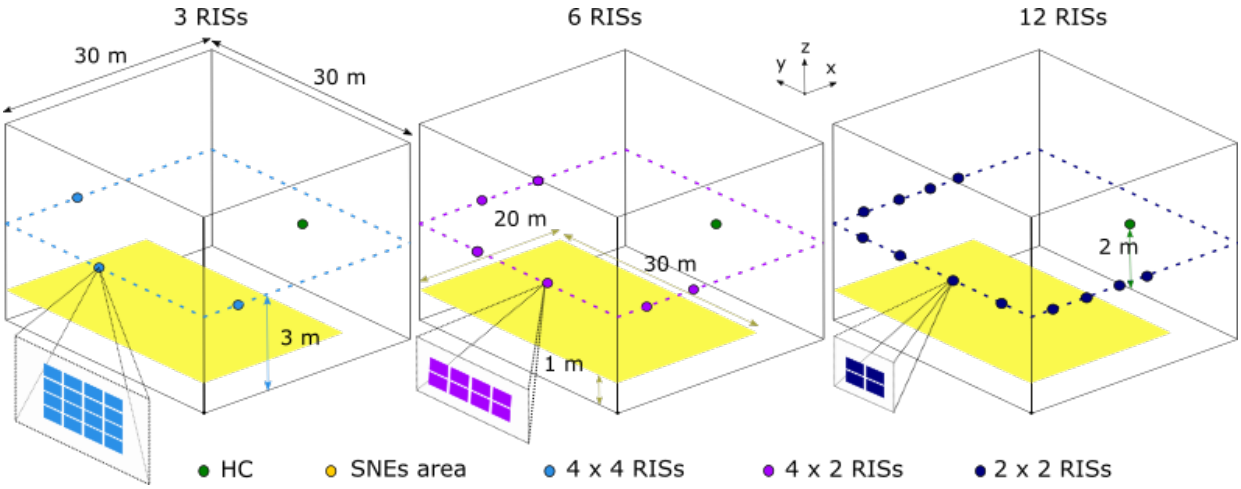

FIGURE 19 WORKING SCENARIO

For the simulations three main configurations have been used, with 3, 6, and 12 RISs. To provide an unbiased comparison among the three scenarios the total amount of tiles has been kept constant to 48, each tile provided with 200 elements, thus entailing a 4 x 4, 4 x 2, and 2 x 2 tiles configuration for the case with 3, 6 and 12 RISs respectively. The RISs centres positions and orientations used in the three scenarios are provided in tabular form for the different tiles' configuration in Table 12.

TABLE 12 TILES CONFIGURATION, POSITION AND ORIENTATION FOR RISS INVOLVED IN SYSTEM SIMULATIONS

TILES CONFIGURATION	POSITION	ORIENTATION
4 X 4	(10, 0, 3) (5, 30, 3)	(x, z)
	(0, 15, 3)	(y, z)
4 x 2	(0, 20, 3) (0, 10, 3)	(y, z)
	(3, 0, 3) (13, 0, 3) (8, 30, 3) (18, 30, 3)	(x, z)
2 x 2	(0, 24, 3) (0, 18, 3) (0, 12, 3) (0, 6, 3)	(y, z)
	(2, 0, 3) (7, 0, 3) (12, 0, 3) (17, 0, 3) (3, 30, 3) (8, 30, 0)	(x, z)

	(13, 30, 3) (18, 30, 3)	

All antennas and RIS elements are spaced half wavelength apart. As for the SNEs, unless otherwise specified, we consider individual antennas SNEs. The simulation parameters are reported in Table 8 of Section 3.3. The results are given in terms of spectral efficiency (bits/s/Hz) for a single subcarrier and are obtained by Monte Carlo simulations for the cases in which 4, 6, and 8 SNEs are considered. In this simulation campaign we consider the system to be frequency non-selective, i.e., the RIS optimization wouldn't change considering a large bandwidth.

The direct HC-US link is characterised by two different channel models, Indoor Office (IO) and Shopping Mall (SM), each with a probability of 70% and 30%, respectively (refer to [87]). Both cases represent NLOS scenarios, where IO indicates stronger attenuation with distance, and SM signifies a qualitatively better direct connection. In contrast, the HC to RIS (HC-RIS) and RIS to SNE (RIS-SNE) connections are assumed to occur under LOS conditions, taking advantage of the greater height of the RIS.

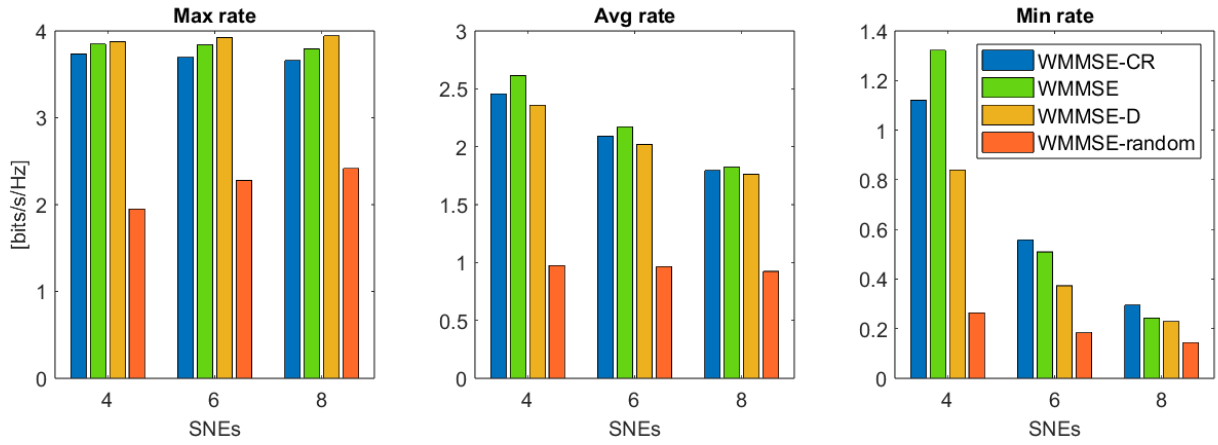

FIGURE 20 PROPOSED SCHEMES COMPARED FOR MAX (LEFT), AVG (MIDDLE), AND MIN (RIGHT) RATES, 3 RIS CONFIG.

In Figure 20 the outcomes computed for the 3-RIS configuration are displayed, representing maximum, average, and minimum rates for the proposed WMMSE optimization approach with RIS allocation and constraint relaxation, denoted as WMMSE-CR. In these instances, the weights in the maximisation process are uniformly set to 1, indicating the absence of a specific scheduling policy for fairness. Equivalently, the utility function $U(x) = x$ is employed.

For comparison purposes, we also give the cases WMMSE, which corresponds to the optimal WMMSE approach presented in [87] (optimization of each RIS atom without RIS allocation), WMMSE-D corresponding to the case in which the tiles are allocated to the closest SNEs, and WMMSE-*random*, which corresponds to the case where the RISs are not optimised, i.e., they are given a random configuration and very little advantage can be gained by RIS. This last case closely resembles an environment without the presence of RIS.

The results indicate a close match between WMMSE-CR and WMMSE, confirming that the proposed RIS assignment does not notably compromise performance while considerably reducing algorithmic complexity. In addition to this advantage, the results for the minimum rate (on the right of the figure) reveal that the main advantage obtained by the presence of RISs is fairness, i.e., RISs facilitate a more pronounced increase in the minimum rate, while exhibiting less pronounced advantages in terms of average or maximum rates. Conversely, for WMMSE-CR, there remains a notable difference between the maximum and minimum rates, a distinction that amplifies with an increasing number of SNEs. The WMMSE-D method yields superior performance in terms of the maximum rate, albeit at the expense of the minimum rate, yielding a reduction in fairness.

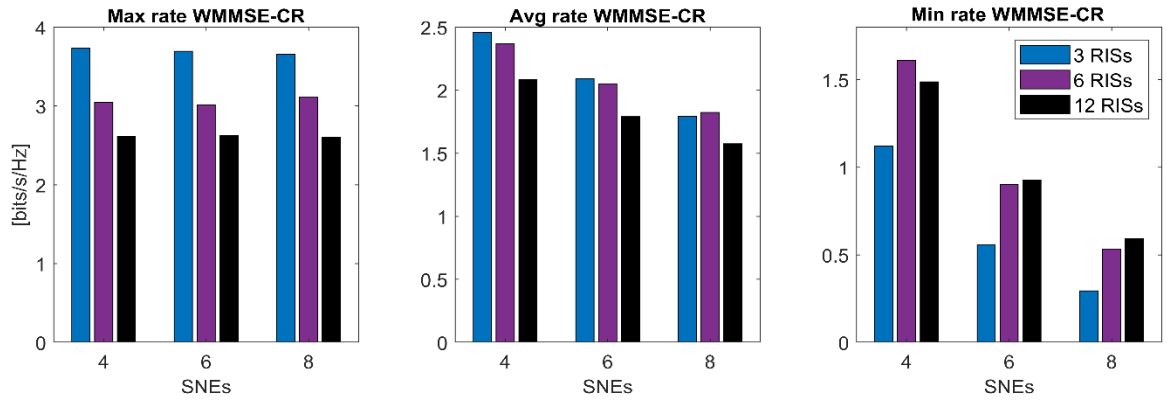

FIGURE 21 MAX (L), AVG (C), AND MIN (R) RATES USING WMMSE-CR VS THE NUMBER OF SNES WITH 3, 6, AND 12 RISS

Figure 21 provides a thorough comparison, showcasing the results obtained from the WMMSE-CR algorithm in scenarios featuring 3, 6, and 12 RISs. The presented results show maximum, average, and minimum rates across scenarios involving 4, 6, and 8 SNEs. Clearly, as the number of RISs increases, there is a simultaneous decrease in both maximum and average rates, coupled with an increase of the minimum rate. More specifically better performance in terms of the minimum rate is achieved for the case with 8 SNEs and 12 RISs, compared with the case of 6 SNEs and 3 RISs. This implies that, even when more SNEs compete for finite resources, those with the lowest allocation still achieve superior results. These observations underscore that the primary performance enhancements facilitated by RISs are notably evident in terms of achieving fairness across diverse communication scenarios.

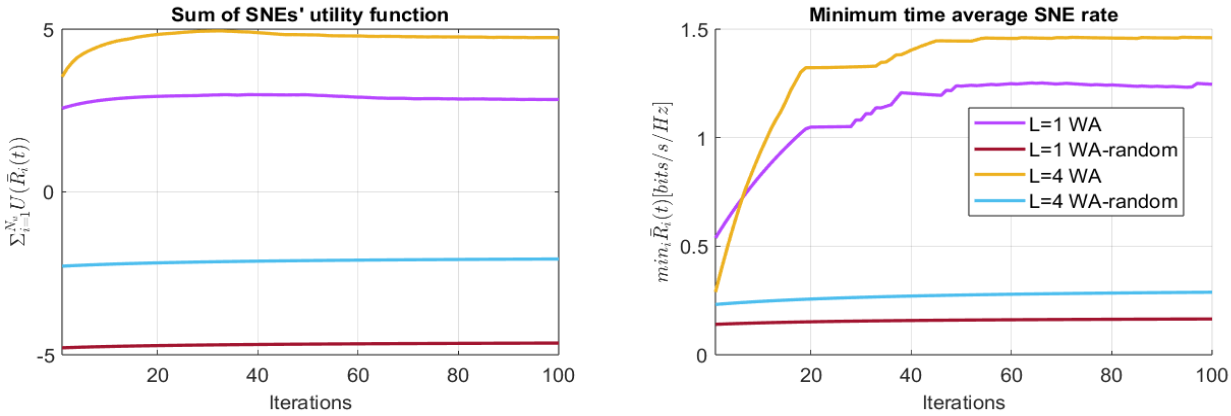

FIGURE 22 MISO VS MIMO WMMSE-CR-WA RESULTS FOR SUM OF SNES' UTILITY (L) AND MIN TIME AVG.

To emphasize this aspect, we conducted simulations employing the Weight Adaptation (WA) strategy. The outcomes for the WA approach are depicted in Figure 22, including a comparison between scenarios with MIMO and Multiple-Input Single-Output (MISO) configurations (L = 4 and L = 1, respectively). Specifically, the figure employs a proportional fairness utility function, $U(x) = \log(x)$. Achieving a stable solution in this case requires running the WMMSE algorithms a sufficient number of times. At each iteration, the weights are updated, and new average rates are determined for each SNE. Subsequently, the algorithms are executed with the updated weights for the subsequent time step.

The figure presents the value of the objective function (left) and the minimum rate (right) as a function of the iteration index. This applies to scenarios where RISs are optimized according to the proposed algorithm (WA) and where RISs are assigned a random configuration (WA-random). On the left side of the figure, it is evident that, for both MISO and MIMO cases, the WMMSE-CR-WA RIS optimization approach significantly enhances the objective function compared to the WMMSE-CR case, represented by the starting point of each curve. On the right side of the figure, the minimum rate is also substantially increased with the WA approach, while no significant improvement is observed with a random RIS configuration. In this case, only precoder optimization is performed,

effectively. Regarding the comparison between different numbers of antennas on the SNEs' side, the simulation results indicate that the MIMO case yields higher rates, aligned with expectations.

5.2.4 ADVANCEMENTS WITH RESPECT TO THE STATE OF THE ART

The primary comparison for the proposed algorithm can be drawn in relation to the methodology presented in [87]. This approach introduces an optimization algorithm for configuring RISs in a multi-SNE MIMO system, aiming to maximise the system sum rate by utilising only the statistical characterization of the mobile SNE locations. Consequently, the proposed approach does not necessitate the estimation of instantaneous CSI or second-order channel statistics for RIS optimization. This characteristic significantly alleviates, or even eliminates, the need for frequent reconfiguration of RISs, which is a critical challenge in RIS-based systems. However, in this approach, the optimization strategy pertains to every single RIS scattering element, offering no additional complexity reduction beyond the RIS optimization rate. In fact, when considering the linear programming approach applied to cases where RIS optimization operates at the level of individual atoms, the algorithm complexity becomes comparable to the cube of the number of individual RIS atoms [102]. In contrast, with the proposed approach, the complexity is contingent on the total number of tiles. In other words, if the total number of tiles is much smaller than the number of elements, a significant advantage in terms of system complexity can be achieved.

5.2.5 ACHIEVED KPIS AND FUTURE ACTIVITY

Simulation results actually shows the effectiveness of the proposed approach in terms of the minimum SNE rate assured for the SNEs involved in the communication system. This work can be viewed as an initial stride towards an approach where the aim is to ensure identical performance for all SNEs, such as minimizing power for a fixed rate per SNE. A similar problem was tackled in the foundational work [103], but the proposed solution is exceedingly intricate and challenging to apply in practical scenarios. Therefore, the emphasis on diminishing system complexity through intelligent RIS allocation becomes especially crucial in this context. Considering the reduced complexity offered by our approach, future investigations could delve into exploring more intricate RIS models.

6. CONCLUSION

This deliverable has reported the activities carried out and initial results obtained during the first year of the project as planned in Task 3.3 "*Reconfigurable intelligent surfaces*". The long-term goal is to assess to what extent RISs might be beneficial for in-X subnetworks under study in 6G-SHINE and how they can be exploited towards the achievement of objectives 3 and 4 of the project.

After a survey and classification of available and under-study RIS technologies, the main models used to characterize and design RISs, detailing potential integration into ray-tracing tools, have been described. A preliminary analysis of the main design issues and the promising RIS technologies expected to enhance the target KPIs has been carried out for the use cases defined in WP2. This analysis serves as a foundational reference for the ongoing research activity which aims to develop RIS-aided PHY/MAC methods and RIS optimization algorithms.

Some preliminary investigations have been reported in this deliverable. Notably, a RIS-aware MAC framework for 6G-SHINE X-subnetworks that categorizes users based on their traffic characteristics, position, mobility, and QoS requirements has been proposed. Regarding RIS deployment and optimization strategies, an initial investigation of the effect of RIS-generated interference in scenarios where microcells and in-X subnetworks coexist has been presented by comparing various RIS hardware architectures included a novel one. The investigation has been extended to multiple users MIMO scenarios through a rate weight adaptation strategy with the purpose of understanding the optimal RIS configuration maximizing the achievable rate while reducing the signalling overhead and computational burden. Each presented method has been put in relationship with the KPIs/KVIs and use cases of the project.

The concepts and results presented in this deliverable are based on works that are currently in progress, and further findings and recommendations will be provided in deliverable D3.4. Specifically, the next planned activity is mainly oriented towards the following aspects:

- Embed models for RIS in the ray-tracing tool.
- Expand the investigations about the coexistence of RIS-equipped subnetworks with macro-cells to the most promising 6G-SHINE use cases. As a second step, design protocols for coexistence of RIS-empowered subnetworks with other cells.
- Conduct system-level simulations to analyse the effectiveness of spatially non-selective RIS to avoid interference.
- Design of novel RIS-aware MAC protocols, for instance, in which the RIS can dynamically adjust the wireless environment, also including the RIS in the scheduling process of resources among the SNEs.
- Inclusion of in-band or out-band control channel aspects in RIS-aided MAC protocol design depending on the specific subnetwork use case.
- Extend the proposed low-complexity RIS optimization strategy for multi-user MIMO scenarios aimed at maximizing the system rate in a fair manner.

Other aspects are not excluded to be tackled in the future activity in case new critical issues will emerge during the next investigations.

REFERENCES

[1] Deliverable D2.2: 'Refined definition of scenarios, use cases and service requirements for In-X subnetworks ', Project 6G SHINE, 2024.

[2] M. Di Renzo et al., 'Smart radio environments empowered by AI reconfigurable meta-surfaces: An idea whose time has come', EURASIP Journal on Wireless Communications and Networking, vol. 129, pp. 1-20, May 2019.

[3] M. Jian et al., 'Reconfigurable intelligent surfaces for wireless communications: Overview of hardware designs, channel models, and estimation techniques', Intelligent and Converged Networks, vol. 3, no. 1, pp. 1-32, March 2022, doi: 10.23919/ICN.2022.0005.

[4] Y. Liu et al., 'Reconfigurable Intelligent Surfaces: Principles and Opportunities', IEEE Communications Surveys & Tutorials, vol. 23, no. 3, pp. 1546-1577, third quarter 2021.

[5] E. Bjornson et al., 'Reconfigurable Intelligent Surfaces: Three Myths and Two Critical Questions', IEEE Communications Magazine, vol. 58, no. 12, pp. 90-96, December 2020, doi: 10.1109/MCOM.001.2000407.

[6] E. Basar et al., 'Wireless Communications Through Reconfigurable Intelligent Surfaces', IEEE Access, vol. 7, pp. 116753-116773.

[7] C. Huang et al., 'Reconfigurable Intelligent Surfaces for Energy Efficiency in Wireless Communication', IEEE Transactions on Wireless Communications, vol. 18, no. 8, pp. 4157-4170, Aug. 2019.

[8] T. Chen et al., 'Model-free Optimization and Experimental Validation of RIS-assisted Wireless Communications under Rich Multipath Fading', arXiv preprint arXiv:2302.10561, 2023.

[9] M. Barbuto et al., 'Metasurfaces 3.0: A New Paradigm for Enabling Smart Electromagnetic Environments', in IEEE Transactions on Antennas and Propagation, vol. 70, no. 10, pp. 8883-8897, Oct. 2022, doi: 10.1109/TAP.2021.3130153.

[10] E. C. Strinati et al., 'Reconfigurable, Intelligent, and Sustainable Wireless Environments for 6G Smart Connectivity', IEEE Communications Magazine, vol. 59, no. 10, pp. 99-105, October 2021, doi: 10.1109/MCOM.001.2100070.

[11] H. Zhang et al., 'Toward Ubiquitous Sensing and Localization with Reconfigurable Intelligent Surfaces', Proceedings of the IEEE, vol. 110, no. 9, pp. 1401-1422, Sept. 2022, doi: 10.1109/JPROC.2022.3169771.1

[12] U. Saeed et al., 'Intelligent Reflecting Surface-Based Non-LOS Human Activity Recognition for Next-Generation 6G-Enabled Healthcare System', Sensors, vol. 22, no. 19, p. 7175, Sep. 2022, doi: 10.3390/s22197175.

[13] Y. Cui et al., 'Digital Twin-Aided Learning for Managing Reconfigurable Intelligent Surface-Assisted, Uplink, User-Centric Cell-Free Systems', arXiv preprint arXiv:2302.05073, 2023.

[14] H. Wymeersch et al., 'Radio Localization and Mapping with Reconfigurable Intelligent Surfaces: Challenges, Opportunities, and Research Directions', IEEE Vehicular Technology Magazine, vol. 15, no. 4, pp. 52-61, Dec. 2020, doi: 10.1109/MVT.2020.3023682.

[15] P. del Hougne, 'Robust position sensing with wave fingerprints in dynamic complex propagation environments', Physical Review Research, vol. 2, p. 043224, Nov. 2020.

[16] Y. Liu et al., 'Reconfigurable Intelligent Surfaces: Principles and Opportunities', IEEE Communications Surveys & Tutorials, vol. 23, no. 3, pp. 1546-1577, third quarter 2021.

[17] ETSI white paper n. 10, 'Maturity and field proven experience of millimeter wave transmission', Sept. 2015.

[18] ETSI white paper, 'Reconfigurable Intelligent Surfaces (RIS); Use Cases, Deployment Scenarios and Requirements', – ETSI GR RIS 001, Apr. 2023.

[19] G. Oliveri et al., 'Reconfigurable electromagnetics through Metamaterials: a review', Proceedings of the IEEE, vol. 103, no. 7, pp. 1034–1056, 2015.

[20] Oliveri, G., Rocca, P., Salucci, M., & Massa, 'Holographic smart EM skins for advanced beam power shaping in next generation wireless environments', *IEEE Journal on Multiscale and Multiphysics Computational Techniques*, *6*, 171-182, 2021.

[21] Q. Li et al., 'Reconfigurable intelligent surfaces relying on non-diagonal phase shift matrices', IEEE Transactions on Vehicular Technology, 71(6), 6367-6383, 2022.

[22] M. Mizmizi et al., 'Space-Time Phase Coupling in STMM-based Wireless Communications', arXiv preprint arXiv:2306.00466, 2023.

[23] D. Dardari and D. Massari, 'Using metaprisms for performance improvement in wireless communications', IEEE Transactions on Wireless Communications, vol. 20, no. 5, pp. 3295-3307, 2021.

[24] M. Lotti, G. Calesini, and D. Dardari, 'NLOS Localization Exploiting Frequency-selective Metasurfaces', arXiv preprint arXiv:2307.12800 (2023).

[25] M. Lotti and D. Dardari, 'Metaprism-aided NLOS Target Localization', 2023 31st European Signal Processing Conference (EUSIPCO). IEEE, 2023.

[26] Basharat, S., Hassan, S. A., Mahmood, A., Ding, Z., & Gidlund, M. 'Reconfigurable intelligent surface-assisted backscatter communication: A new frontier for enabling 6G IoT networks', *IEEE Wireless Communications*, *29*(6), 96-103, 2022.

[27] Zhao, Yang, and Bruno Clerckx 'RIScatter: Unifying Backscatter Communication and Reconfigurable Intelligent Surface', *arXiv preprint arXiv:2212.09121* (2022).

[28] D. Dardari et al., 'Establishing Multi-user MIMO Communications Automatically using Retrodirective Arrays', IEEE Open Journal of the Communications Society, 2023.

[29] N. Shlezinger, G. C. Alexandropoulos, M. F. Imani, Y. C. Eldar and D. R. Smith, 'Dynamic Metasurface Antennas for 6G Extreme Massive MIMO Communications', in IEEE Wireless Communications, vol. 28, no. 2, pp. 106-113, April 2021, doi: 10.1109/MWC.001.2000267.

[30] T. Cui et al., 'Coding metamaterials, digital metamaterials and programmable metamaterials', Light Sci Appl 3, e218 (2014), vol. 62, no. 1, pp. 183-198, 2014.

[31] J. Hu et al., 'Reconfigurable intelligent surface based RF sensing: Design, optimization, and implementation', IEEE Journal on Selected Areas in Communications, vol. 38, no. 11, pp. 2700–2716, 2020.

[32] F. Costa and M. Borgese, 'Circuit Modelling of Reflecting Intelligent Surfaces,' 2021 IEEE 22nd International Workshop on Signal Processing Advances in Wireless Communications (SPAWC), Lucca, Italy, 2021, pp. 546-550, doi: 10.1109/SPAWC51858.2021.9593104.

[33] Y. Ra'di et al., 'Tailoring reflections from thin composite metamirrors', IEEE Transactions on Antennas and Propagation, vol. 62, no. 7, pp. 3749-3760, July 2014.

[34] C. L. Holloway et al., 'Reflection and transmission properties of a metafilm: with an application to a controllable surface composed of resonant particles', IEEE Transactions on Electromagnetic Compatibility, vol. 47, no. 4, pp. 853-865, Nov 2005.

[35] D. Demmer et al., 'Hybrid Precoding Applied to Multi-Beam Transmitting Reconfigurable Intelligent Surfaces (T-RIS)', Electronics, vol. 12, no. 5: 1162, 2023, https://doi.org/10.3390/electronics12051162.

[36] W. Tang et al., 'Wireless communications with reconfigurable intelligent surface: Path loss modeling and experimental measurement', IEEE Transactions on Wireless Communications, vol. 20, no. 1, pp. 421-439, Jan 2021.

[37] S. W. Ellingson, 'Path loss in reconfigurable intelligent surface-enabled channels', arXiv preprint arXiv:1912.06759, 2019.

[38] S. V. Hum and J. Perruisseau-Carrier, 'Reconfigurable reflectarrays and array lenses for dynamic antenna beam control: A review', IEEE Transactions on Antennas and Propagation, vol. 62, no. 1, pp. 183–198, Jan 2014.

[39] D. R. Smith, O. Yurduseven, L. P. Mancera, P. Bowen, and N. B. Kundtz, 'Analysis of a waveguide-fed metasurface antenna', Phys. Rev. Applied, vol. 8, p. 054048, Nov 2017.

[40] J. P. Turpin et al., 'Reconfigurable and tunable metamaterials: A review of the theory and applications', International Journal of Antennas and Propagation, vol. 2014, 2014.

[41] C. L. Holloway et al., 'An overview of the theory and applications of metasurfaces: The two-dimensional equivalents of metamaterials', IEEE Antennas and Propagation Magazine, vol. 54, no. 2, pp. 10-35, April 2012.

[42] C. Liaskos et al., 'Design and development of software defined metamaterials for nanonetworks', IEEE Circuits and Systems Magazine, vol. 15, no. 4, pp. 12-25, Fourth quarter 2015.

[43] C. Pfeifer and A. Grbic, 'Metamaterial Huygens' surfaces', in 2013 IEEE MTT-S International Microwave Symposium Digest (MTT), June 2013, pp. 1-4.

[44] S. B. Glybovski et al., 'Metasurfaces: From microwaves to visible', Physics Reports, vol. 634, pp. 1–72, 2016.

[45] C. Pfeiffer and A. Grbic, 'Metamaterial Huygens' surfaces: Tailoring wave fronts with reflectionless sheets', Phys. Rev. Lett., vol. 110, p. 197401, May 2013.

[46] M. Selvanayagam and G. V. Eleftheriades, 'Circuit modeling of Huygens surfaces', IEEE Antennas and Wireless Propagation Letters, vol. 12, pp. 1642–1645, 2013.

[47] N. Mohammadi Estakhri and A. Alù, 'Wave-front transformation with gradient metasurfaces', Phys. Rev. X, vol. 6, p. 041008, Oct 2016.

[48] V. S. Asadchy et al., 'Perfect control of reflection and refraction using spatially dispersive metasurfaces', Phys. Rev. B, vol. 94, p. 075142, Aug 2016.

[49] A. Diaz-Rubio et al., 'From the generalized reflection law to the realization of perfect anomalous reflectors', Science Advances, vol. 3, no. 8, e1602714, 2017.

[50] QW. Tang, M. Z. Chen, X. Chen, J. Y. Dai, Y. Han, M. Di Renzo, Y. Zeng, S. Jin, Q. Cheng, and T. J. Cui, 'Wireless communications with reconfigurable intelligent surface: Path loss modeling and experimental measurement', IEEE Transactions on Wireless Communications, vol. 20, no. 1, pp. 421–439, Jan 2021.

[51] M. D. Renzo, A. Zappone, M. Debbah, M. Alouini, C. Yuen, J. D. Rosny, and S. Tretyakov, 'Smart radio environments empowered by reconfigurable intelligent surfaces: How it works, state of research, and road ahead', IEEE Journal on Selected Areas in Communications, pp. 1–1, 2020.

[52] Q. Wu, S. Zhang, B. Zheng, C. You, and R. Zhang, 'Intelligent Reflecting Surface Aided Wireless Communications: A Tutorial', arXiv e-prints, p. arXiv:2007.02759, Jul. 2020.

[53] C. Liaskos, S. Nie, A. Tsioliaridou, A. Pitsillides, S. Ioannidis, and I. Akyildiz, 'A new wireless communication paradigm through software-controlled metasurfaces', IEEE Communications Magazine, vol. 56, no. 9, pp. 162–169, Sep. 2018

[54] M. D. Renzo, M. Debbah, D.-T. Phan-Huy, A. Zappone, M.-S. Alouini, C. Yuen, V. Sciancalepore, G. C. Alexandropoulos, J. Hoydis, H. Gacanin, J. d. Rosny, A. Bounceur, G. Lerosey, and M. Fink, 'Smart radio environments empowered by reconfigurable AI meta-surfaces: an idea whose time has come', EURASIP Journal on Wireless Communications and Networking, vol. 2019, no. 1, p. 129, 2019.

[55] S. W. Ellingson, 'Path loss in reconfigurable intelligent surface-enabled channels', arXiv preprint arXiv:1912.06759, 2019.

[56] F. Liu et al., 'Reflectarrays and Metasurface Reflectors as Diffraction Gratings: A tutorial', IEEE Antennas and Propagation Magazine, vol. 65, no. 3, pp. 21-32, June 2023, doi: 10.1109/MAP.2023.3236278.

[57] N. Thanh Nguyen et al., 'Hybrid Relay-Reflecting Intelligent Surface-Aided Wireless Communications: Opportunities, Challenges, and Future Perspectives', arXiv e-prints, p. arXiv:2104.02039, Apr. 2021.

[58] J. An et al., 'Stacked Intelligent Metasurface-Aided MIMO Transceiver Design', arXiv preprint arXiv:2311.09814, 2023.

[59] J. An et al., 'Stacked intelligent metasurface performs a 2D DFT in the wave domain for DOA estimation', arXiv preprint arXiv:2310.09861, 2023.

[60] S. Abeywickrama et al., 'Intelligent reflecting surface: Practical phase shift model and beamforming optimization', IEEE Transactions on Communications, vol. 68, no. 9, pp. 5849–5863, 2020.

[61] G. Gradoni and M. Di Renzo, 'End-to-end coupling aware communication model for reconfigurable intelligent surfaces: An electromagnetic-compliant approach based on mutual impedances', IEEE Wireless Communications Letters, pp. 1–1, 2021.

[62] A. Abrardo et al., 'MIMO Interference Channels Assisted by Reconfigurable Intelligent Surfaces: Mutual Coupling Aware Sum-Rate Optimization Based on a Mutual Impedance Channel Model', arXiv e-prints, p. arXiv:2102.07155, Feb. 2021.

[63] Bartoli, Giulio, et al. 'Spatial multiplexing in near field MIMO channels with reconfigurable intelligent surfaces', IET Signal Processing 17.3 (2023): e12195.

[64] Li, Hongyu, et al. 'Beyond diagonal reconfigurable intelligent surfaces with mutual coupling: Modeling and optimization', arXiv preprint arXiv:2310.02708 (2023).

[65] Nerini, Matteo, et al. 'Beyond Diagonal Reconfigurable Intelligent Surfaces Utilizing Graph Theory: Modeling, Architecture Design, and Optimization', arXiv preprint arXiv:2305.05013 (2023).

[66] Li, Hongyu, et al. 'Reconfigurable intelligent surfaces 2.0: Beyond diagonal phase shift matrices', arXiv preprint arXiv:2301.03288 (2023).

[67] Y. Liu et al., 'STAR: Simultaneous Transmission and Reflection for 360° Coverage by Intelligent Surfaces', IEEE Wireless Communications, vol. 28, no. 6, pp. 102-109, December 2021, doi: 10.1109/MWC.001.2100191.

[68] Di Renzo, Marco, et al. 'Communication models for reconfigurable intelligent surfaces: From surface electromagnetics to wireless networks optimization', Proceedings of the IEEE 110.9 (2022): 1164-1209.

[69] S. Zhang et al., 'Intelligent Omni-Surface: Ubiquitous Wireless Transmission by Reflective-Transmissive Metasurface', arXiv e-prints, p. arXiv:2011.00765, Nov. 2020.

[70] V. S. Asadchy et al., 'Functional metamirrors using bianisotropic elements', Phys. Rev. Lett., vol. 114, p. 095503, Mar 2015.

[71] A. Diaz-Rubio and S. A. Tretyakov, 'Macroscopic Modeling of Anomalously Reflecting Metasurfaces: Angular Response and Far-Field Scattering', arXiv e-prints, p. arXiv:2012.03727, Dec. 2020.

[72] F. H. Danufane et al., 'On the path-loss of reconfigurable intelligent surfaces: An approach based on Green's theorem applied to vector fields', IEEE Transactions on Communications, pp. 1-1, 2021.

[73] V. Degli Esposti, E. M. Vitucci, M. Di Renzo, S. Tretyakov, 'Reradiation and Scattering from a Reconfigurable Intelligent Surface: a General Macroscopic Model', IEEE Transactions on Antennas and Propagation, vol. 70, no. 10, pp. 8691-8706, Oct. 2022

[74] E.M. Vitucci, M. Albani, S. Kodra, M. Barbiroli and V. Degli-Esposti, 'An Efficient Ray-Based Modeling Approach for Scattering from Reconfigurable Intelligent Surfaces', IEEE Transactions on Antennas and Propagation, 2024, available in early access. doi: 10.1109/TAP.2024.3359288.

[75] E. M. Vitucci, M. Fabiani, V. Degli-Esposti, '*Use of a Realistic Ray-Based Model for the Evaluation of Indoor RF Coverage Solutions Using Reconfigurable Intelligent Surfaces*', ELECTRONICS, 2023, 12, Article number: 1173, pp. 1 - 14

[76] Fuschini, F., Vitucci, E. M., Barbiroli, M., Falciasecca, G., & Degli-Esposti, V. 'Ray tracing propagation modeling for future small-cell and indoor applications: A review of current techniques', *Radio Science*, *50*(6), 469-485, 2015

[77] 'Study on channel model for frequencies from 0.5 to 100 GHz', 3GPP TR 38.901, v17.1.0, Dec. 2023.

[78] Croisfelt, Victor, et al. 'Random access protocol with channel oracle enabled by a reconfigurable intelligent surface', IEEE Transactions on Wireless Communications, vol. 22, no. 12, Dec. 2023.

[79] X. Cao, B. Yang, H. Zhang, C. Huang, C. Yuen and Z. Han, 'Reconfigurable Intelligent Surface-Assisted MAC for Wireless Networks: Protocol Design, Analysis, and Optimization', *IEEE Internet of Things Journal*, Vol. 8, no. 18, Sep. 2021.

[80] X. Cao et al., 'AI-Assisted MAC for Reconfigurable Intelligent-Surface-Aided Wireless Networks: Challenges and Opportunities', in IEEE Communications Magazine, vol. 59, no. 6, pp. 21-27, June 2021.

[81] X. Cao et al., 'Massive Access of Static and Mobile Users via Reconfigurable Intelligent Surfaces: Protocol Design and Performance Analysis', in IEEE Journal on Selected Areas in Communications, vol. 40, no. 4, pp. 1253-1269, April 2022, doi: 10.1109/JSAC.2022.3145908.

[82] X. Cao, B. Yang, C. Huang, C. Yuen, M. D. Renzo, D. Niyao, Z. Han, 'Reconfigurable Intelligent Surface-assisted Aerial-Terrestrial Communications via Multi-task Learning', *IEEE Journal on Selected Areas in Communications,* vol. 39, no. 10, Oct. 2021.

[83] S. Prabh, 'On Intelligent Reflecting Surfaces Element Allocation Using Genetic Algorithms', 2022 IEEE 33rd Annual International Symposium on Personal, Indoor and Mobile Radio Communications (PIMRC), Kyoto, Japan, 2022, pp. 01-06, doi: 10.1109/PIMRC54779.2022.9977607.

[84] João Henrique Inacio de Souza et al, 'Uplink Multiplexing of eMBB/URLLC Services Assisted by Reconfigurable Intelligent Surfaces,', https://arxiv.org/abs/2305.04629

[85] M. Almekhlafi, M. A. Arfaoui, M. Elhattab, C. Assi and A. Ghrayeb, 'Joint Resource Allocation and Phase Shift Optimization for RIS-Aided eMBB/URLLC Traffic Multiplexing', in IEEE Transactions on Communications, vol. 70, no. 2, pp. 1304-1319, Feb. 2022.

[86] E. Björnson, H. Wymeersch, B. Matthiesen, P. Popovski, L. Sanguinetti and E. de Carvalho, 'Reconfigurable Intelligent Surfaces: A signal processing perspective with wireless applications', in *IEEE Signal Processing Magazine*, vol. 39, no. 2, pp. 135-158, March 2022.

[87] A. Abrardo, D. Dardari, and M. D. Renzo, 'Intelligent Reflecting Surfaces: Sum-Rate Optimization Based on Statistical Position Information', *IEEE Trans Comm*, vol. 69, no. 10, pp. 7121–7136, Jul. 2021.

[88] A. Abrardo, A. Toccafondi, and M. Di Renzo, 'Design of Reconfigurable Intelligent Surfaces by Using S-Parameter Multiport Network Theory–Optimization and Full-Wave Validation', *ArXiv Prepr. ArXiv231106648*, 2023.

[89] F. H. Danufane, M. D. Renzo, J. de Rosny, and S. Tretyakov, 'On the path-loss of reconfigurable intelligent surfaces: An approach based on Green's theorem applied to vector fields', *arXiv:2007.13158*, 2020.

[90] N. S. Perovic and al., 'Achievable Rate Optimization for MIMO Systems with Reconfigurable Intelligent Surfaces', *arXiv:2008.09563*, 2020.

[91] X. Mu, Y. Liu, L. Guo, J. Lin, and R. Schober, 'Joint Deployment and Multiple Access Design for Intelligent Reflecting Surface Assisted Networks', *IEEE Trans. Wirel. Commun.*, vol. 20, no. 10, pp. 6648–6664, 2021, doi: 10.1109/TWC.2021.3075885.

[92] Y. Guo, Z. Qin, Y. Liu, and N. Al-Dhahir, 'Intelligent Reflecting Surface Aided Multiple Access Over Fading Channels', *IEEE Trans. Commun.*, vol. 69, no. 3, pp. 2015–2027, 2021, doi: 10.1109/TCOMM.2020.3042277.

[93] J. Zuo, Y. Liu, Z. Quin, and N. Al-Dhahir, 'Resource Allocation in Intelligent Reflective Surface Assisted NOMA Systems', *IEEE Trans. Commun.*, vol. 68, no. 11, pp. 7170–7183, 2020, doi: 10.1109/TCOMM.2020.3016742.

[94] Y. Yang, B. Zheng, S. Zhang, and R. Zhang, 'Intelligent Reflecting Surface Meets OFDM: Protocol Design and Rate Maximization', *IEEE Trans. Commun.*, vol. 68, no. 7, pp. 4522–4535, 2020, doi:10.1109/TCOMM.2020.2981458.

[95] A. Khaleel and E. Basar, 'A Novel NOMA Solution with RIS Partitioning', *IEEE J. Sel. Top. Signal Process.*, vol. 16, 16, no. 1, pp. 70–81, 2022, doi: 10.1109/JSTSP.2021.3127725.

[96] Y. Ramamoorthi, M. Iwabuchi, T. Murakami, T. Ogawa, and Y. Takatori, 'Resource Allocation for Reconfigurable Intelligent Surface Assisted Dual Connectivity', *Sensors*, vol. 22, no. 15, 2022, doi: 10.3390/s22155755.

[97] F. Rusek, et al., 'Spatially selective intelligent surfaces through rewiring', Accepted for publication at ICC'2024.

[98] J. Angjo, A. Zubow, and F. Dressler, 'Side effects of IRS: On the need for coordination in 6G multi-operator IRS-assisted networks', IEEE Global Telecommunications Conference (Globecom), Kuala Lumpur, Malaysia, Dec., 2023.

[99] S. Palmucci, A. Abrardo, and M. Moretti, 'Optimal RIS Allocation in Multi-User MIMO Communications', in *2023 21st Mediterranean Communication and Computer Networking Conference (MedComNet)*, IEEE, 2023, pp. 188–195.

[100] Q. Shi and al., 'An Iteratively Weighted MMSE Approach to Distributed Sum-Utility Maximization for a MIMO Interfering Broadcast Channel', *IEEE Tran Signal Process.*, vol. 59, no. 9, pp. 4331–4340, 2011.

[101] '5G Channel Model for bands up to 100 GHz', *Report*, pp. 1–107, Oct. 2016.

[102] P. M. Vaidya, 'An algorithm for linear programming which requires \mathcalO(((m+ n) n^2+(m+ n)^1.5 n)L) arithmetic operations', in *Proceedings of the nineteenth annual ACM symposium on Theory of computing*, 1987, pp. 29–38.

[103] Q. Wu and R. Zhang, 'Intelligent Reflecting Surface Enhanced Wireless Network via Joint Active and Passive Beamforming', *IEEE Trans Wirel. Comm*, vol. 18, no. 11, pp. 5394–5409, Nov. 2019

[104] 'Study on NR Network-controlled Repeaters,' 3GPP TR 38.867, Sept. 2023.

[105] Chao-Kai Wen et al. 'Shaping a Smarter Electromagnetic Landscape: IAB, NCR, and RIS in 5G Standard and Future 6G', arXiv, https://doi.org/10.48550/arXiv.2308.03016, 2024.

[106] G. Bartoli, A. Abrardo, N. Decarli, D. Dardari, M. Di Renzo, "Spatial multiplexing in near field MIMO channels with reconfigurable intelligent surfaces", IET Signal Processing, Vol. 17, no. 3, March 2023, https://doi.org/10.1049/sil2.12195.

[107] ETSI GR RIS-001, "Reconfigurable Intelligent Surfaces (RIS); Use Cases, Deployment Scenarios and Requirements," V1.1.1, April 2023.

[108] ETSI GR RIS-002, "Reconfigurable Intelligent Surfaces (RIS); Technological challenges, architecture and impact on standardization," V1.1.1, Aug. 2023.